Manipulation Of Soft Matter System In Nonequilibrium Conditions

Thesis submitted for the degree of

Doctor of Philosophy (Science)

in

Physics (Theoretical)

by

Rahul Karmakar

Department of Physics

University of Calcutta

2023

To
Mother
Father
my sister
our weaver bird

Acknowledgement

This thesis is my 1 st child. In this journey of fatherhood, there are numerous ups and downs with passion and emotions.

First and foremost, I want to acknowledge my supervisor Prof. Jaydeb Chakrabarti for introducing me to such an interesting and advanced field of research. I truly take this opportunity to convey my respect and gratitude from the core of my heart. The 5 years journey with Porf. Chakrabarti turns into a friend, and philosopher along with my guide. The journey starts with coursework (Advance Stat Mech.(2018). I start writing my 1 st Monte Carlo Code in my PhD journey in this coursework. Being a code lover from my school days, I assured myself maybe I came to a place where I shall do what I want to do in upcoming years. Every interaction with Prof. Chakrabarti cooked something inside me. That is not only science and also apart from science. He taught me how to think and how to cross the barrier. How can I forget our group meeting? It is true at first it was a nightmare for us(me and Abhik Ghosh Moulick). But as the days passed, every interaction gives me new insight. Every topic we discuss(either I am presenting or others), opens up my understanding how easily I can think of something and in which direction should I go.

I am also grateful towards my thesis member Prof. Gautam Gangopadhyay and Prof. Punyabrata Pradhan for their helpful suggestions and comments in my every evaluation. I also show my gratitude towards Prof. Deb Shankar Ray for his helpful comments in my JRF to SRF evaluation. I would like to give a special thanks to my senior Edwin (Dr. Edwin Tendong) for his constant support and immense help in understanding many things for my research.

I thank my fellow group members present and past who helped me during different phases of my works in different ways: Dr. Suman Dutta, Dr. Samapan Sikdar, Dr. Sutapa Dutta, Dr. Priya Patra, Dr. Sasthi Charan Mandal, Edwin Tendong, Abhik Ghosh Moulick, Suravi Pal, Anirban Paul, Avik Sasmal, Kanika Kole.

I believe in destiny. Some persons, I meet as my life goes, they put some weightage of them in me. I try to carry those philosophies along with me. I always like to pursue my academic career in Physics from my school days. Thankfully, I got a chance at Vidyasagar College, where some miracle happened to me. I meet Prof. Sukanya Dasgupta, Prof. Saugata Bhattacharya. I extend my vote of thanks to them. I still remember Prof. Saugata Bhattacharya first introduced us with Brownian Dynamics. Brownian Dynamics is the bread and butter of my 1 st paper. At my post graduate level, how can I forget Prof.

Abhijit Bandyopadhyay who introduce me the power of nothingness. From that day at least I try to feel for that powerful reality. I thank Prof. Shamik Gupta, Prof. Bobby Ezhuthachan, Prof. Partha Sarathi Majumdar, Prof. Somendra M. Bhattacharjee for their support. I gratefully acknowledge Birati High School, Vidyasagar College and RKMVERI for providing me with the perfect ambience and educational support.

Being a very aloof kind of person, they are few people I cherish in my SNB days. First I shall mention Sidhartha Biswas, with whom I used to discuss many spiritual things apart from science. I also mention Abhik and Indrani, we had a small group name 'Chotuskon'. How can I forget Shovan (Shovan Dev Mandal), my singing partner and co composer? We wrote and composed a few songs, whatever the quality of those, they will remain close to our hearts forever.

I acknowledge S. N. Bose. National Centre for Basic Sciences for providing me with wonderful research facilities. Special thanks to DST, Govt. of India for providing me INSPIRE Fellowship.

Finally, I acknowledge my mother, father and sister. They stood by me from the very first day of my academic career. Without them, I can't move a bit. I only think about my problem. I am almost ignorant of the problem in my house because of them. They take care of all of those staff. Whatever I am today because of their constant support and sacrifice.

This thesis is a treat to all of those who helped in shaping me in different ways.

Rahul Karmakar
Kolkata, India
March 2023

Abstract

Soft matter systems have length scales ranging from several nanometres to a few microns and slow time scales due to large sizes. These systems are termed soft due to their sensitivity to external perturbations as compared to pure molecular materials. Colloidal dispersion, polymers, membranes and biological macromolecules are typical soft matter systems. Soft matter systems in equilibrium have been studied in great details.

These systems can be easily driven out of equilibrium by external perturbations, like shear, temperature gradient, tuning electric and magnetic fields and applying pressure and so on. The simplest non-equilibrium state of a system is steady state. This means that there is a time independent current in the system. Example of typical non-equilibrium steady state phenomenon includes phase transitions like shear-banding, lane formation, glass and gel formation, homogeneous and heterogeneous crystal nucleation and cluster formation, tracer diffusion in polymeric membrane under external force.

Soft matter systems show steady state structures by forming aggregates, like ordering micron-sized objects in low-Reynolds number flows, aggregation of active matters where the particle motion is aided by energy sources, polymeric systems, colloidal aggregation in toggling magnetic field, electric field, periodic forcing, chemical reaction fuels and thermal gradients and so on. Manipulation of these type of systems under non-equilibrium steady state condition is relevant in a variety of technological applications, like separation of components in organic solvents, sensors, trapping of bio molecules, micro-fluidic applications and colloidal confinement to name a few.

In the thesis, we have investigated a couple of classes of soft matter systems in non-equilibrium situation: (1) Steady state behaviour of systems with temperature sensitive interactions in the presence of temperature gradient. (2) Motion of particles driven through a polymeric network. These systems in non-equilibrium situations may be helpful for various technological purposes. We observe long-ranged crystalline order in cold region in thermo-sensitive ligand capped noble metal nanoparticles in presence of temperature difference. The aggregated order particles may be useful for sensory applications. We also study thermo responsive colloids which show change in diameter with temperature. We observe long-range order in hot region as well as in cold region in presence of temperature gradient in this system beyond a certain diameter ratio. It can be helpful in designing structures at high temperature. In other class of problem, we explore different parameters of polymer network to reduce respiratory droplet permeation through a facemask. We observe that the efficiency

of the facemask depends on composition of polymer, interaction strength of tracer and the network, the polymeric network rigidity and the thickness of the confinement. Our results may be helpful in designing breathable facemask with better efficiency. Finally, we study a model system to control binary mixture separation through membrane using reverse osmosis technique. We observe performance of RO membrane in terms of permeation, solute rejection, fouling can be controlled with changing relative interaction of membrane material with mixture. Our results may be useful for designing reverse osmosis membrane with better permeation, selectivity and less fouling for longer use.

সারাংশ

সফট ম্যাটার সিস্টেম গুলোকে সহজেই অসাম্য অবাস্থায় নিয়ে যাওয়া সম্ভব তার সাম্যবস্থা থেকে নানারকম বাহ্যিক প্রভাবের মাধ্যমে, যেমন বাইরে থেকে বল প্রয়োগ করে বা তাপমাত্রার তারতম্য ঘটিয়ে। খুব সাধারণ ভাবে বলতে গেলে অসাম্য অবস্থার একটি বিশেষ রূপ হলো তখন যখন সিস্টেমটির মধ্যে কোনো নির্দিষ্ট দিকে প্রবাহ থাকেনা। এই ধরনের অসাম্য অবস্থায় থাকা সফট ম্যাটার সিস্টেম গুলোর নানারকম ব্যাবহারিক প্রয়োগ আছে।

সেরকম ই কয়েক প্রকার অসাম্য অবস্থায় থাকা সফট ম্যাটার সিস্টেম এই থিসিস এর আলোচনার বিষয়। ১) থার্মরেস্পনসিভ বস্তু দের তাপমাত্রার তারতম্য এর জন্য তৈরি হওয়া অসাম্য অবস্থা র দশা, ২) বাহ্যিক বলের উপস্থিতিতে পলিমার নেটওয়ার্ক এর মধ্যে দিয়ে বস্তুকণার গতিপথ। এই ধরনের সিস্টেম গুলি প্রযুক্তির দিক থেকেও ভীষণ গুরুত্বপুর্ন হতে পারে। আমরা এই ধরনের কিছু সিস্টেম মলিকিউলার সিমুলেশন এর মাধ্যমে আলোচনা করেছি ।

সাম্প্রতিক এক পরীক্ষায় দেখা গেছে লিগান্ড পরিহিত ধাতব ন্যানোপর্টিকেল এর মধ্যেকার ইন্টারেকেশন তাপমাত্রার ওপর নির্ভরশীল। এই ধরনের পর্টিকলস সিস্টেমস এর মধ্যে যখন তাপমাত্রার তারতম্য সৃষ্টি করা হয়, তারা অপেক্ষাকৃত ঠান্ডা জায়গায় এসে জমায়িত হয়। এই জমায়েত অবস্থার পার্টিকলস রা সেন্সর হিসেবে তাদের ব্যাবহারিক প্রয়োগ দেখতেও সক্ষম হয়। আরেক ধরনের বস্তু আছে যারা তাপমাত্রা পরিবর্তনের আয়তন পরিবর্তন ঘটায়। এই ধরনের বস্তু যারা তাপমাত্রার পরিবর্তনের সাথে নানারকম ভাবে ইন্টারেকেশন এর পরিবর্তন ঘটায়, তাদের থার্মরেস্পন্সিভ বস্তু বলা হয়। এই ধরনের বস্তুরা অসাম্য অবস্থায় নানারকম আকার ধারণ করে, যাদের আণবিক ভাবে বোঝা ভীষণ প্রয়োজনীয়।

আমরা আমাদের মডেল গণয়ায় সেরকম ই কিছু সিস্টেম নেই যাদের ইন্টারেকেশন তাপমাত্রার ওপর নির্ভরশীল। তাদের ইন্টারেকেশন সেই সমস্ত লিগান্ড পরিহিত ধাতব ন্যানোপর্টিকেল এর মত। আমাদের মডেল গণনায় ইন্টারেকেশন গুলোতে বিকর্ষণ এবং আকর্ষণ দুই ধরনের টার্ম ই আছে। বিকর্ষণ টার্ম আসে কারণ বস্তু গুলো পরীক্ষায় জিটা বিভব(পোটেনশিয়াল) দেখায় । যা তাদের সারফেস এ চার্জ এর অবাস্থান প্রমাণ করে যার ফলে তারা একে অপরকে বিকর্ষণ করবে। আবার লিগন্ড গুলো হাইড্রফোবিক ধরনের যারা আকর্ষণ করে একে অপরকে। তাই দুই ধরনের টার্ম ই রাখা হয়েছে। আমরা বিকর্ষণ তাপমাত্রা কমানোর সাথে কমে আবার আকর্ষণ তাপমাত্রা কমানোর সাথে বৃদ্ধি পায়। ন্যানোপর্টিকেল গুলোর চলাফেরা (ডিফফিউশন) গরম তাপমাত্রায় বেশি হয়। আমরা আমাদের মডেল গণনা ব্রাউনীনান ডাইনামিক্স সিমুলেশন এর মাধ্যমে করি। আমাদের মডেল গণনায় এই ধরনের সিস্টেম এর মধ্যে আমরা তাপমাত্রার তারতম্য সৃষ্টি করি। কিছু জায়গা অপেক্ষাকৃত ঠান্ডা এবং কিছু জায়গা অপেক্ষাকৃত গরম। বস্তু গুলো যখন এক তাপমাত্রা অঞ্চল থেকে আরেক অঞ্চলে প্রবেশ করে আমরা তাদের ইন্টারেকেশন এবং ডিফফিউশন সেই তাপমাত্রা অনুযায়ী পরিবর্তন করে দেই। আমরা লক্ষ্য করি ঠান্ডা তাপমাত্রায় বস্তুগুলো একত্রিত হয় এবং কেলাস(ক্রিস্টাল) গঠন করে। গরম তাপমাত্রায় তাদের পরিমাণ কমে যায় এবং তরল অবস্থায় থাকে। এই ঘটনার কারণ ঠান্ডা তাপমাত্রায় তাদের একত্রিত হওয়া এবং চলাফেরা মন্থর বলে। আমরা আরো কিছু গণনা করি একধরনের কলোইডস বস্তু নিয়ে যারা তাদের ব্যাস পরিবর্তন করে তাপমাত্রা র সাথে। গরম তাপমাত্রায় ব্যাস কমে যায় এবং ঠান্ডায় বৃদ্ধি পায়। এদের মধ্যে আমরা তাপমাত্রার তারতম্য সৃষ্টি করি। আমরা লক্ষ্য করি একটি নির্দিষ্ট ব্যাসের অনুপাতের জন্য গরম এবং ঠান্ডা উভয় অঞ্চলেই তারা কেলাস গঠন করে।

আরেক ধরনের কাজে আমরা আলোচনা করি বাহ্যিক বলের উপস্থিতিতে পলিমার নেটওয়ার্ক এর মধ্যে দিয়ে বস্তুকণার গতিপথ। এর উদাহরণ হলো ফেসমাস্ক যা বর্তমান অতিমারি তে ভীষণ গুরুত্বপূর্ণ। আমরা মডেল গণনায় দেখি কিভাবে রেসপিরেটরি ড্রপ্লেটস কে ফেসমাস্ক এর মধ্যে দিয়ে একদিক থেকে অন্য দিকে কম চলাফেরা করানো যায়। যাহাতে ফেসমাস্ক এর কর্মক্ষমতা বৃদ্ধি পায় বিভিন্ন পলিমার নেটওয়ার্ক এর বৈশিষ্ট এর ওপর নির্ভর করে।

সবশেষে একটি গুরুত্বপূর্ণ বিষয়ে আমরা আলোকপাত করি যেটি হল রিভার্স অস্মসিস পদ্ধতি তে মেমব্রেন এর মাধ্যমে একটি মিশ্রণ কে পরিশুদ্ধ করা । ইহা আমাদের প্রত্যেকের বাড়িতে দরকার জল পরিশোধনের জন্য। আমরা মডেল গনয়ায় একটি বাইনারি মিশ্রণ/দ্রবণ থেকে দ্রাব ও দ্রাবক কে পৃথক করি। আমরা দেখতে পাই মেমব্রেন এর মাধ্যমে পৃথক করার দক্ষতা কে মেমব্রেন ও মিশ্রণ এর মধ্যেকার আপেক্ষিক ইন্টারেকেশন এর মাধ্যমে নিয়ন্ত্রণ করা যেতে পারে। আমাদের কাজ পরিশোধনের জন্য কিরকম মেমব্রেন তৈরি করার প্রয়োজন তার কিছু দিশা দেখতে পারে।

List of Publications

1. A long-range order in a thermally driven system with temperature-dependent interaction. Rahul Karmakar, Jaydeb Chakrabarti; Soft Matter, 2022, 18, 867; DOI: 10.1039/d1sm01379c.

2. Model studies on motion of respiratory droplets driven through a face mask. Rahul Karmakar, Aishani Ghosal and Jaydeb Chakrabarti; EPL, 141 (2023) 27001 ; doi: 10.1209/0295-5075/acaf9f.

3. Long ranged order formation in the hot region using thermoresponsive particles in presence of temperature gradient. Rahul Karmakar, Jaydeb Chakrabarti. (Manuscript to be submitted)

4. Reverse Osmosis of binary mixture through polymeric membrane. Rahul Karmakar, Jaydeb Chakrabarti. (Manuscript under preparation)

Contents

List of Figures

List of Tables

Chapter 1 Introduction

Soft matter systems have length scales ranging from several nanometres to a few microns and slow time scales due to large sizes.[1] These systems are termed soft due to their sensitivity to external perturbations as compared to pure molecular materials. Colloidal dispersion, polymers, membranes and biological macromolecules are typical soft matter systems. Soft matter systems in equilibrium have been studied in great details.

These systems can be easily driven out of equilibrium by external perturbations, like shear, temperature gradient, tuning electric and magnetic fields and applying pressure and so on. The simplest non-equilibrium state of a system is steady state. This means that there is a time independent current in the system. Example of typical non-equilibrium steady state phenomenon includes phase transitions like shear-banding, lane formation,[2] glass and gel formation, homogeneous and heterogeneous crystal nucleation and cluster formation, tracer diffusion in polymeric membrane[3] under external force.

Soft matter systems show steady state structures[4–7] by forming aggregates, like ordering micron-sized objects in low-Reynolds number flows,[8] aggregation of active matters where the particle motion is aided by energy sources,[9–13] polymeric systems[14] , colloidal aggregation in toggling magnetic field,[15] electric field,[2,16,17] periodic forcing,[18] chemical reaction fuels[19,20] and thermal gradients[21] and so on. Manipulation of these type of systems under non-equilibrium steady state conditions[8–10,15,18–21] is relevant in a variety of technological applications, like separation of components in organic solvents,[22] sensors,[21] trapping of bio molecules,[23] micro-fluidic applications and colloidal confinement[24] to name a few.

In the thesis, we have investigated a couple of classes of soft matter systems in

non-equilibrium situation: (1) Steady state structures in systems with temperature sensitive interactions in the presence of temperature gradient. (2) Motion of particles driven through a polymeric network. These systems in non-equilibrium situations may be helpful for various technological purposes. We observe long-ranged crystalline order in cold region in thermo-sensitive ligand capped noble metal nanoparticles in presence of temperature difference. The aggregated order particles may be useful for sensory applications. We also study thermo responsive colloids which show change in diameter with temperature. We observe long-ranged order in hot region as well as in cold region in presence of temperature gradient in this system beyond a certain diameter ratio. It can be helpful in designing structures at high temperature. In other class of problem, we explore different parameters of polymer network to reduce respiratory droplet permeation through a facemask. We observe that the efficiency of the facemask depends on composition of polymer, interaction strength of tracer and the network, the polymeric network rigidity and the thickness of the confinement. Our results may be helpful in designing breathable facemask with better efficiency. Finally, we study a model system to control binary mixture separation through membrane using reverse osmosis technique. We observe performance of RO membrane in terms of permeation, solute rejection, fouling can be controlled with changing relative interaction of membrane material with mixture. Our results may be useful for designing reverse osmosis membrane with better permeation, selectivity and less fouling for longer use.

We describe the main findings of our work below in the following order. In section 1.1, we describe the steady state structure of a fluid with temperature sensitive interaction in temperature difference. In section 1.2 we study a model where temperature sensitivity of interaction is taken through change in diameter. Section 1.3 describes our investigations on a model FM where respiratory droplets movement takes place through polymeric network in presence of external driving. Section 1.4 depicts our findings on Reverse Osmosis of binary mixture through a polymeric membrane.

1.1 Ordering in suspension of thermally driven ligand capped noble metal nanoparticles

Soret effect or thermophoresis is particle movement in presence of temperature gradient.[25–28] It has been widely studied in the past[29–31] in micron-sized colloids

and nano-meter sized particles.[25,32–36] Recent experimental studies[21] show formation of large clusters with very high mono-dispersity index in cold region in an aqueous solution of noble metal (gold and silver) nanoparticles capped by citrate ligand in presence of temperature gradient. The large aggregated cluster act as a platform for Surface Enhanced Raman Scattering (SERS) to detect chemical species of a part in billion, leading to real-time, rapid, reliable and ultra-sensitive detection of discrete molecules from the solid-vapor and liquid-vapor interface. Further, the surface zeta potential of the metal nanoparticles fall in the cold region, suggesting decrease in the electrostatic repulsion due to decrease in temperature. Particle aggregation here[21] is driven by non-equilibrium situation in presence of temperature difference in the system and temperature sensitive interparticle interaction.

We study the model thermo-senstive particles in the presence of temperature difference defined as x axis. We show a schematic of our system in Fig. 1.1. The system is in equilibrium at hot temperature $T_H(= 373K)$(Fig. 1.1(a)). Then we create cold temperature $T_c(= 273K)$ regions as Fig. 1.1(b). The temperature sensitive interaction parameters are introduced as follows: The zeta potential indicates presence of surface charges over the particles screened by counter-charges. These particles interact with each other by screened electrostatic repulsion. As temperature is lowered, larger number of ligands are stabilized over the nanoparticle surface which screen the surface charges more efficiently decreasing the electrostatic repulsion as observed from zeta potential fall in experiment.[21] The electrostatic repulsion between two particles at separation r is modelled through standard Derjaguin–Landau–Verwey–Overbeek (DLVO) potential $V_R(r) = V_0\frac{e^{-\kappa r}}{r}$.[37] Here V_0 is prefactor of repulsion and κ is the inverse screening length. V_0 and κ both depend on temperature through the dependence on zeta potential. On the other hand, the ligands themselves are hydrophobic. The hydrophobic species are known to attract each other.[38] The hydrophobic attraction mediated between the ligand coated surfaces is modelled through a harmonic potential $V_A(r) = \alpha(r-1)^2$.[38] The strength α is proportional to the number of ligands bind to the surface which is large at lower temperature. The changes in electrostatic repulsion and in hydrophobicity mediated attraction with temperature are accounted for parametrically through the V_0, κ, α. The particle positions are updated with the periodic boundary conditions(PBC) in three directions using the Brownian Dynamics(BD) algorithm where interaction forces and the noise are taken as per the local temperature.

After creating temperature difference we observe that the density in cold

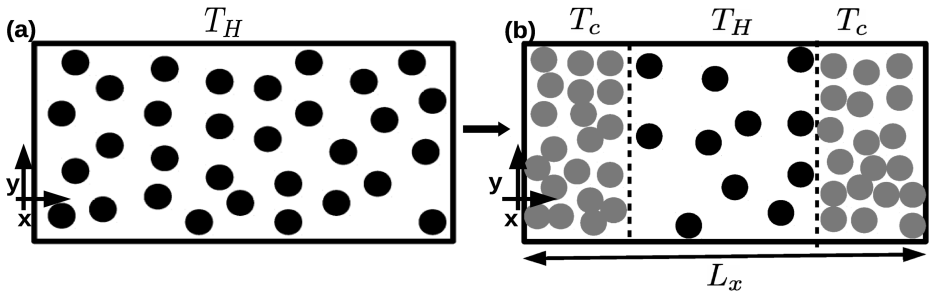

Figure 1.1: (a) The system is equilibrated at hot temperature T_H. (b) We cool two ends at T_C. The middle region remains at hot T_H. The black particles are at hot region and grey particles are at cold region. (The z-axis not shown is pointing into the page for panel(a-b)).

region increases with time and that decreases with time in hot region which is also evident from the schematic in Fig. 1.1(b). The increased density and slower diffusion lead to long-range order formation in the cold region. Using the Unsupervised Machine Learning(UML) algorithm we find the presence of two clusters of different structures as revealed through the bond order parameters $\bar{q}_l$. We find that the cold region has predominantly body centered cubic(BCC) structure at steady state coexisting with liquid phase[39] from bond order parameters $\bar{q}_4$ and $\bar{q}_6$. The kinetics of structural growth in the cold regions is extracted through the crystal fraction θ_c, the ratio of solid like particles and number of particles present at a given time in the cold region. We observe that the crystallization takes place in a two step manner from an initial slow to rapid crystal formation and finally to saturation.

Our observation of long-ranged order formation may pave way for microscopic understanding of long-range order formation of temperature dependent interaction in temperature difference. The presence of the long-ranged order in our system suggests that the surface area may be macroscopic and thus, useful for sensory applications.

1.2 Long ranged order by thermoresponsive particles in hot region

We also study thermoresponsive particles with temperature dependent size. In experiments, temperature dependent sizes are observed in poly-N-isopropylacrylamide colloidal particles. These thermoresponsive particles are cross-linked microgel spheres. They can absorb water at room temperature. Their volume decreases by

releasing water above room temperature. These particles are observed to form ordered structure in cold region in temperature gradient.[40] We investigate order formation in thermoresponsive hydrogel where particle volume is sensitive to temperature creating temperature gradient. We treat thermoresponsive hydrogel as Lennard-Jones(LJ) ($4\epsilon[(\frac{\sigma}{r})^{12} - (\frac{\sigma}{r})^{6}$) fluid whose diameter is sensitive to temperature, σ_C in cold temperature T_C and σ_H at hot temperature T_H, where $\sigma_C > \sigma_H$. We perform the Molecular Dynamics(MD) simulations on the particles with the PBC in three directions of the box. Here we equilibrate the system at a higher temperature $\frac{k_B T_H}{\epsilon} = 1.2$(in LJ unit) in a liquid state (Fig. 1.2(a)) and then cool two ends at $\frac{k_B T_C}{\epsilon} = 1$ leaving the middle region at the centre of the box at hot temperature(Fig. 1.2(b)). The schematic diagram in Fig. 1.2(b) shows that the diameter increases in cold temperature T_C compared to temperature T_H.

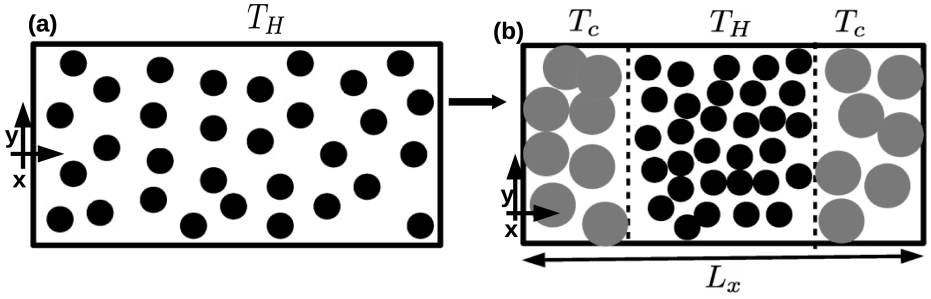

Figure 1.2: (a) The system is equilbrated at hot temperature T_H. (b) We cool two ends at T_C. The middle region remains at hot T_H. The black particles are at hot region and grey particles are at cold region. Grey particles are larger in size than black particles. (The z-axis not shown is pointing into the page for panel(a-b)).

We vary parameter $\sigma^* = \frac{\sigma_c}{\sigma_H}$ for a given $T^* = \frac{T_H}{T_C}$. We generate steady state structural diagram in σ^* - T^* plane for a given $T^*(= 1.2)$. We identify steady state structure base on based on $(\bar{q}_4, \bar{q}_6)$ plot. We observe both region remains liquid for lower value of σ^*. At first the cold region starts to emerge order formation whereas hot region remains liquid with increasing σ^* value. Both hot and cold regions show long-range order for sufficiently large σ^*. This is shown schematically in Fig. 1.3.

The intriguing phenomenon of crystallization in the hot region can be understood as follows. We calculate the net flux ΔJ at the two interfaces $\Delta J = J_{HC} - J_{CH}$, (Fig. 1.4) where J_{HC} is flux from hot region to cold region and J_{CH} is flux from cold region to hot region. We observe that J goes from negative value to zero and fluctuates around zero. This means that particles movement from cold region to hot region dominates over that from hot region to cold region and saturates. As particles diameter increases in cold region, they are pushed

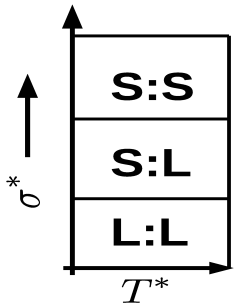

Figure 1.3: Schematic of steady state diagram in $\sigma^* - T^*$ plane. Symbols L and S denote liquid and ordered state respectively. Left side denotes the structure of cold region, right side for the hot region.

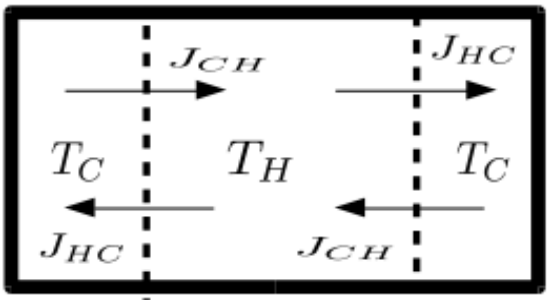

Figure 1.4: Schematic of flux calculation. Arrows in two interfaces denote particle flux from hot region to cold region J_{HC} and cold region to hot region J_{CH}.

out from the cold region to the hot region due to excluded volume effect. As a result, the packing fraction increases also in the hot region due to increase in particle. Packing fraction increases in cold region as well due to large diameter in spite of reduction of particle number. Increase in packing fraction in both regions leads to the crystallization in steady state. This is further reflected in overall pressure P in the system. We observe P suddenly increases in cold region initially due to large number of particles with large diameter. Subsequently, P decreases with time as particles pushes out from the cold to hot region and also due to structural rearrangement. Simultaneously P increases in hot region due to increases in particle number density. At steady state pressure becomes flat in both hot and cold regions.

Long-range order in hot region which we observe may also be interesting in practical scenario for designing ordered materials at high temperature. Our observation can be observed with more careful experiments in future.

1.3 Motion of fluid droplets driven through a face mask

Face mask(FM) has become important in recent times after COVID-19 pandemic hit the globe. FM prevents spread of airborne diseases by capturing respiratory droplets emitted by an affected person while speaking, coughing, sneezing.[41] These droplets consist of different salts, proteins in small amounts and microorganisms all floating in water. According to the WHO recommendation, FM should be made up of three layers:[42,43] a polar material like cotton layer inside towards mouth and hydrophobic material in the middle and the outermost layers.[43,44] Commercial available N95 FMs with fibres of micrometer range filter 95% of the micro-droplets through electrostatic capture and mechanical interception.[45] But they show reduction in efficiency due to charge loss.[46] Several studies mainly after post pandemic situation are performed to search for stable FM performances like tribo-electric generators,[44,47,48] mixture of fabrics with different compositions,[49] and multiple layers.[42] Nano-fibres[45] and metal-organic framework filters[50,51] are also studied. But they show breathing difficulty due to nano-meter size pores. FMs need to exchange essential molecules between the human body and the atmosphere so that normal breathing takes place.[49] For comfortable breathing pressure drop inside FM is calculated for different types of FM materials, which is found to be around 2.5 ± 0.4 Pa.[49] Thus, designing a FM with better stability and breathability is still quite pertinent. Such design can be facilitated by microscopic understanding of droplet movement inside FM.

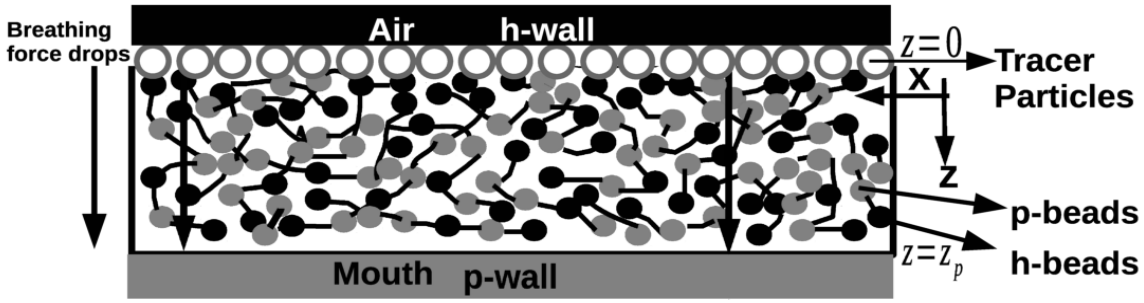

Figure 1.5: A model diagram of Polymeric network confined in asymmetric h(black) and p(grey) wall. Polymer consists of two beads: h-beads are shown in solid black circle and p-beads are shown in solid grey circle. h-beads prefer h-wall and p-beads prefer p-wall. Tracer particles (open grey circle) are added close to h-wall. Tracers prefer p-beads and p-wall. Force on each tracer particle (mimic breathing) is added from h-wall to p-wall. Force are represented by black arrows from h-wall to p-wall. Force is maximum at $z = 0$ and zero at $z = z_P$. (The y-axis not shown is pointing into the page).

Here we model droplet movement through FM under pressure difference as required for normal breathing. We consider explicitly the middle layer of the tri-layer FM. Each polymeric strand is composed of randomly distributed two kinds of beads (h-bead and p-bead) of the same diameter σ ($1\mu m$) and mass m in a given h:p ratio, randomly distributed over the strand. A schematic diagram is shown in Fig. 1.5. We take the interpenetrating polymer network confined by asymmetric walls(h-wall at $z = 0$ and p-wall at $z = z_P$) favouring h-beads and p-beads representing the outermost and the innermost layer respectively following WHO recommendation.[43] Then we study tracer permeation from the air side(h-wall) of the FM towards the side facing the mouth(p-wall) shown schematically in Fig. 1.5, using the Langevin dynamics simulation. We take respiratory droplets as tracer colloidal particles(TCP) of LJ type.

Non-bonded interactions between the polymeric beads are taken to be LJ type. The bonded interactions among the beads are harmonic with rigidity k. The h-beads are taken to interact mutually more strongly compared to that between the p-beads to mimic hydrophobic species which are known to collapse[38,52,53] and ensure strong interpenetration of the network. We choose TCPs to interact via an energy parameter $\epsilon_{tr,tr}$ and interact more favourably with the p-beads ($\epsilon_{tr,p}$) and the p-wall ($\epsilon_{tr,wp}$) than the h-beads ($\epsilon_{tr,h}$) and the h-wall($\epsilon_{tr,wh}$). We exert external force $F(z)$ on TCPs, which is taken to be maximum at h-wall and linearly vanishes at p-wall to ensure breathing. We study the motion of the TCPs through the network from h-wall to p-wall. The ratio $\bar{\epsilon} = \frac{\epsilon_{tr,p}}{\epsilon_{tr,h}}$, k and confinement length z_P are varied in the simulation.

First, we estimate mean pore size of the polymer network from tracer density profile $\rho_{tr}(z)$ along confinement z-direction without external drive. The profile shows peaks. We identify mean pore size $\sim$ 2 micrometer where the tracer density profile is sharply peaked near h-wall. As larger tracer will be stopped geometrically, our focus is on tracer size slightly smaller than the mean pore size. We restrict further analysis to droplet size $<$ 2 micrometer. The peak close to p-wall is permeation P and efficiency of mask is $e = 100 - P$.

Next we apply driving force along +z direction on the TCPs. We explore the temperature dependence of P. We observe that tracer permeation is an activated Arrhenius process[54] with tunable barrier. The potential energy barrier responsible for the activation process increases with tracer size, tracer bead interaction $\bar{\epsilon}$, rigidity of network k, and decreases with confinement length z_P, driving force. The efficiency $e > 90\%$ of the mask can be achieved by composition of polymer(h:p ratio = 50:50), interaction strength of tracer and

the network $\bar{\epsilon} > 3.3$, the network rigidity $k > 200 k_B T/\sigma^2$ and the thickness of the confinement $z_P = 5.5 \mu m$.

Our model is sufficiently robust. It may be helpful in designing mask with better efficiency while retaining normal breath-ability conditions at room temperature.

1.4 Reverse Osmosis of binary mixture through polymeric membrane

We study another application of polymer based membrane which is Reverse Osmosis(RO) process for separation of components in a solution. A solution is characterized by the presence of solute of a given concentration. If a solution of lower solute concentration and that of higher solute concentration is connected with a semipermeable membrane, solvent from low solute concentration region flows to that higher solute concentration by the process of osmosis.[55] Reverse osmosis is a pressure driven technique to overcome the natural osmotic pressure and enable solvent flow from higher to lower solute concentration in steady state conditions.[56] RO membrane separation processes are widely used nowadays both in industry and household purposes[57,58] like water purification.

The semipermeable membranes are thin film composite(TFC) membranes which are entangled polymers prepared from Interfacial polymerization process,[59] widely used in RO process for separation of both polar[60] and non polar[61] mixtures. Three quantities indicate RO membrane efficiency: Permeation P: amount of solvent flow from one side to other side, Solute Rejection R: rejection of solute from solution and Fouling F: amount of solute gather inside membrane during permeation. Experiments show that changing relative interaction of membrane matrix[57,60] with solute and solvent changes membrane efficiency as permeation of solvent, solute rejection and fouling inside the membrane. Despite atomistically detailed simulation for transport processes,[3] it is yet a challenge to design RO membrane with better permeation, solute rejection and less fouling. A coarse-grain model addressing solute and solvent transport may aid designing a better RO membrane.

We study such a coarse-grained model here. In our model the RO membrane is created as a polymeric network in an asymmetric confinement situation to the experimental IP process.[59] The preparation is very similar as described in the previous section. We attach two reservoir (LR and RR) on left and right side

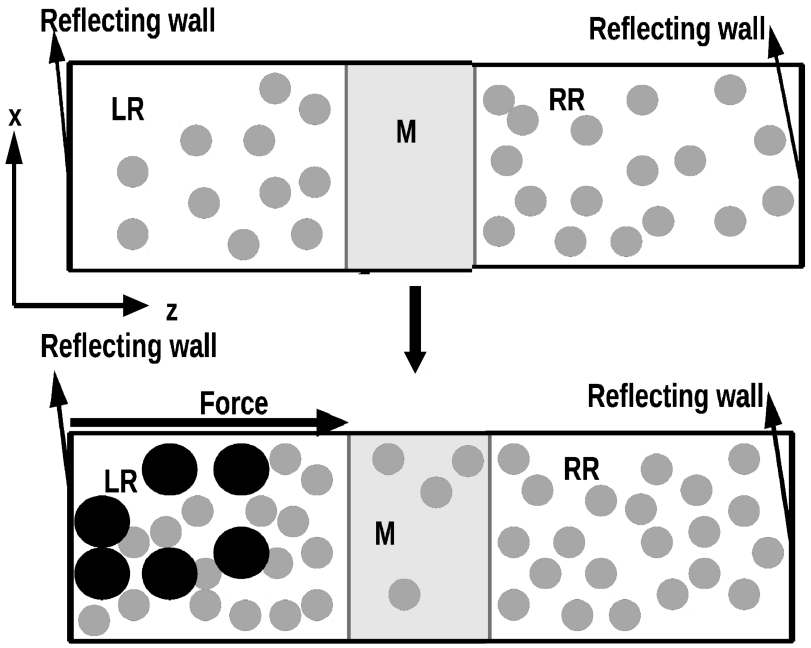

Figure 1.6: Schematic of the simulation cell. The y-axis (not shown) is pointing into the page. Upper panel: Two reservoirs with S particles (grey) are added in two sides of membrane. Lower panel: After solvation of membrane L particles(black) are added in LR.

of the RO membrane(M). Two reflecting walls are placed at two extreme end of two reservoir. Both reservoirs consist of solvent(S) particles. We solvate M without applying force as shown Fig. 1.6(upper panel). After equilibration both LR and RR comes to same density of S. Then we add solute(L) particles (1.8 times larger than S) in the LR removing same number of S particles randomly from the LR so that total number density of particles (S+L) remain same in the box(Fig. 1.6, lower panel). The partial density of S becomes lower in LR compared to RR. There are several interaction in the the system with the strength parameters as follows: the bead-bead interaction ($\epsilon_{\alpha,\beta}$), bead-wall interaction ($\epsilon_{\alpha,wh}$ and $\epsilon_{\alpha,wp}$), solvent-solvent interaction ($\epsilon_{S,S}$), solute-solute interaction ($\epsilon_{L,L}$), solvent-solute interaction ($\epsilon_{S,L}$), solvent h-bead interaction ($\epsilon_{S,h}$), solvent p-bead interaction ($\epsilon_{S,p}$), solute h-bead interaction ($\epsilon_{L,h}$) and solute p-bead interaction ($\epsilon_{L,p}$). Then we add external force $F(z)$ along z to study the motion of both S and L from LR to RR through M.

We study two types of solutions: 1) case of solution particles S,L preferring the h-beads. 2) case of solution particles S,L preferring the p-beads.

1) case of solution particles S,L preferring h-beads - We increase $\bar{\epsilon}_L = \frac{\epsilon_{L,h}}{\epsilon_{L,p}}$, keeping $\bar{\epsilon}_L > 1$. We measure solvent recovery or permeation P in RR, Solute

rejection R in RR when system reaches steady state and fouling F. We observe that both P and R increase with $\bar{\epsilon}_L$ but F also increases. Then, we tune $\bar{\epsilon}_S = \frac{\epsilon_{S,h}}{\epsilon_{S,p}}$ keeping $\bar{\epsilon}_S > 1$ and $\bar{\epsilon}_L = 8.71$. We observe fouling decreases rapidly beyond $\bar{\epsilon}_S = 4$ and R and P has a minimum at $\bar{\epsilon}_S = 4$. We also observe that R and P largely improve for $\bar{\epsilon}_S \geq \bar{\epsilon}_L$. The physical reason behind the observed nature is following: For sufficiently large relative interaction of solvent and membrane beads, the membrane gets sufficiently solvated to resist solute particles from coming from LR to M and subsequently to RR. This improves both R and P.

2) case of solution particles S,L preferring p-beads - Here we restrict to $\bar{\epsilon}_L < 1$ as we increase $\epsilon_{L,p}$. We observe that with decrease in $\bar{\epsilon}_L$ we get better P and R but fouling F also increase with decrease in $\bar{\epsilon}_L$. To reduce F with keeping P and R at large limit, we tune $\bar{\epsilon}_S$ where $\bar{\epsilon}_S < 1$ keeping $\bar{\epsilon}_L = 0.114$. We observe fouling decreases with decrease in $\bar{\epsilon}_S$ and P and R improve for $\bar{\epsilon}_S \leq \bar{\epsilon}_L$.

We relate our results to realistic situations. Here solution preferring h-beads can be thought as a nonpolar solution. Our model shows that interaction of nonpolar beads of membrane should interact sufficiently with solvent and solute. On top of that, the interaction with the nonpolar solvent needs to be at least as strong as that of non-polar solute. Similar observations are observed for the polar solution where solution prefers p-beads. Our model could be helpful to choose appropriate material for RO given the solution. It could be a guiding principle for better performance of RO operation.

The organisation of the thesis is as follows: In chapter 2 we discuss detailed results of long-range formation of ligand capped nanoparticles in the cold region in presence of temperature difference. Long range formation in hot region using thermoresponsive particles and steady state structural diagram are described in details in chapter 3. Driven trace movement in confined polymeric network is studied in chapter 4. Chapter 5 includes detailed study of binary mixture separation through polymeric membrane using RO technique.

Chapter 2 Ordering in suspension of thermally driven ligand capped noble metal nanoparticles

*

2.1 Introduction

Manipulation of macro-molecules under non-equilibrium conditions[8–10,15,18–21] is relevant in a various technological applications, like sensors,[21] separation of components in organic solvents,[22] trapping of bio molecules,[23] microfluidic applications and colloidal confinement[24] to name a few. Often macromolecular migration is accompanied by forming aggregates and emergence of ordered structure,[4–7] like ordering micron-sized objects in low-Reynolds number flows,[8] aggregation of active matters where the particle motion is aided by energy sources,[9–13] polymeric systems[14] , colloidal aggregation in toggling magnetic field,[15] electric field,[2,16,17] periodic forcing,[18] chemical reaction fuels,[1920] and thermal gradients[21] and so on. However, large scale structure formation and phase transitions in driven systems which are away from equilibrium is yet poorly understood.

Creation of temperature gradient is one way to create non-equilibrium situation in a system. Particle migration under temperature gradient, also known as thermophoresis[25] or the Soret effect,[26–28] has been extensively studied in the past[29–31] in micron-sized colloids and nano-meter sized particles.[25,32–36] Theoretical studies often consider simple Lennard Jones (LJ) systems[62] in temperature

*based on publication "A long-range order in a thermally driven system with temperature-dependent interaction". Rahul Karmakar, Jaydeb Chakrabarti; Soft Matter, 2022, 18, 867; DOI: 10.1039/d1sm01379c.

gradients. Some of the recent studies report the time evolution of the temperature and density fields to reach steady states in binary LJ mixture with different mass or strength (or both) in thermal gradient[63–65] including thermal diffusion coefficients (or the Soret coefficient), thermal conductivity and shear viscosity. Recently phase-space distribution functions in the non-equilibrium steady states under a constant thermal gradient are studied by theoretical analysis and supported by non-equilibrium molecular dynamics simulations on LJ systems.[66]

Recent experimental studies[21] show formation of large clusters with very high mono-dispersity index (~ 0.8) in cold region in an aqueous solution of noble metal (gold and silver) nanoparticles capped by citrate ligand in presence of temperature difference. The surface of the highly mono-disperse large clusters of citrate capped noble metal nanoparticles acts as a platform for Surface Enhanced Raman Scattering (SERS) to detect chemical species of a part in billion, leading to real-time, rapid, reliable and ultra-sensitive detection of discrete molecules from the solid-vapor and liquid-vapor interface.[21] The experiments suggest that the interaction between the citrate capped noble metal nanoparticles is far more complicated than simple LJ fluids. More importantly, the surface zeta potential of the metal nanoparticles fall in the cold region, suggesting decrease in the electrostatic repulsion due to decrease in temperature. Temperature sensitive interaction is shown by other macro-molecular systems as well.[40,67] Particle aggregation in these systems is encountered in a non-equilibrium situation in presence of thermal drive and temperature sensitive particle interaction due to temperature difference and is qualitatively different from the aggregation state of ligand capped nanoparticles in equilibrium by changing parameters, like ligand coating and solvent conditions.[68]

The SERS from a Raman sensitive surface depends on the roughness of the exposed surface,[69] where the structure and stability of the large clusters are important. However, no microscopic understanding behind the stability of the particle aggregation and their structural aspects are attempted in the experiments on citrate capped noble metal nanoparticles in aqueous solution in presence of temperature difference in Ref.[21] Here we attempt to understand the particle aggregation in this system microscopically. We model particle interaction in terms of potential of mean force (PMF)[67] where the parameters of the interaction are sensitive to temperature. The zeta potential indicates presence of surface charges over the particles. These particles interact with each other by screened electrostatic repulsion. As temperature is lowered, larger number ligands are stabilized over the nanoparticle surface which screen the

surface charges more efficiently. This decreases the electrostatic repulsion. The ligands themselves are hydrophobic. Therefore, the hydrophobic attraction mediated between the ligand coated surfaces increases at lower temperature. Equilibrium aggregation, as balance of competing hydrophobicity mediated attraction and electrostatic repulsion, has been studied previously.[70] Here we focus on the competing interactions in non-equilibrium steady state condition driven by temperature difference.

We study the system using the Brownian dynamics (BD) simulations[71] in a box with the periodic boundary conditions in three directions. We equilibrate the system at hot temperature and then cool two ends leaving the middle region at the centre of box at hot temperature, as shown schematically in Fig. 2.1(a). We consider temperature dependence of the solvent viscosity γ in addition to the PMF. Hence, the noise used in the BD simulations has different variances in the hot and cold regions. We ignore hydrodynamic interactions which is a reasonable approximation for small volume fractions. After the steady state is reached, we characterize the order in the system by bond order parameter[72,73] and crystal fraction. We observe that the hot region is in the liquid state, while the cold region shows growth of crystalline order.

2.2 Model potential

The systematic forces arise due to electrostatic repulsion and hydrophobicity mediated attraction both of which are temperature dependent. We use the Derjaguin–Landau–Verwey–Overbeek (DLVO) repulsive electrostatic potential between a pair of ligand coated metal nanoparticles i and j at separation $r(= |\vec{r_i} - \vec{r_j}|)$ with the form:

$$V_R(r) = V_0 \frac{e^{-\kappa r}}{r}. \tag{2.1}$$

Here V_0 is the pre-factor of the repulsion given by $\frac{Z^2 e^2 e^{\kappa\sigma}}{\epsilon\sigma(1+\frac{\kappa\sigma}{2})^2}$ where ϵ is dielectric constant of the medium, Ze the effective surface charge on the nanoparticle. κ is the inverse Debye screening length given by,

$$\kappa^2 = \frac{4\pi e^2}{\epsilon k_B T} n_p Ze \tag{2.2}$$

n_p being density of nanoparticle in absence of salt in the solution. While taking the cross interactions between two particles at different temperatures, we take

mean Debye screening length in the pre-factor V_0 and the smaller of the two Debye screening lengths for the damping term.

Temperature dependence of the electrostatic repulsion in Eq. 2.1 is introduced as follows. Both V_0 and κ depend on the surface charge Z which is related to the surface zeta potential ϕ_0:

$$\frac{2Z\lambda_B}{\sigma} = (1 + \kappa\sigma/2)\phi_0 \tag{2.3}$$

for low values of ϕ_0 and η.[37] Here $\lambda_B (= \frac{e^2}{\epsilon k_B T})$ is the Bjerrum length. The temperature dependence is taken via ϕ_0. We set ϕ_0 = 1.2 and 1.0 for hot and cold regions respectively as in the experiments.[21] Eqs. 2.2 and 2.3 are coupled equation. Solving them simultaneously for a given ϕ_0, we get κ and Z in our simulation. We get $\kappa\sigma = 3.0$ and $Z = 160$ in the hot region and $\kappa\sigma = 2.5$ and $Z = 106$ in the cold region. It may be noted that the dielectric constant both in the screening length and the pre-factor by virtue of the equation of motion comes as product with $k_B T$ which is independent of temperature. Hence, we do not consider temperature dependence of the dielectric constant.

Ligands coating on the metal nanoparticle are solvophobic in character. A solvophobic nanoparticle repels solvent molecules stabilizing solvent depleted vapour region of radius Λ_0 with the nanoparticle at the core, creating a vapour-liquid interface where the Laplace pressure acts.[38] We take $2\Lambda_0/\sigma \approx 1.27$ observed for Lennard-Jones systems in a sub-critical liquid.[38] When two such solute particles approach each other to a close distance, the solvent particles get depleted from the overlapping region due to repulsion of both particles so that the vapour-liquid interface disappears and the Laplace pressure drops to zero in this region. This generates imbalance of the Laplace pressure over the particles that leads to effective attraction as shown in Ref.[38] Integrating the Laplace pressure over the area of the spheres, excluding the overlapping area that depends on s, one would generate the effective force between the particles. The effective force is observed to be harmonic in nature for small separation of the particles.[38] The harmonic attraction can be understood from the simple physical picture that increasing separation between the particles results in admitting more solvent particles between the solute particles which is not energetically favourable. The attraction between two large solvophobic solute particles is modelled through a harmonic potential of spring constant βf, as in Ref.[38] :

$$V_A(r) = \beta f (r - 1)^2. \tag{2.4}$$

where the surface-to-surface distance $(r-1)[=s] \leq 2\Lambda_0$. $\beta = 8\pi\gamma_s[\frac{2\Lambda_0}{\sigma} - 1]$ where γ_s is the surface tension at the liquid-vapour interface and f the fraction of ligands attached to a nanoparticle surface in solvent. The dependence on f is introduced to take into account that the ligands bound onto the nanoparticle surface gives rise to hydrophobicity.

Temperature dependence of different parameters in Eq. 2.4 are taken into account as follows. The spring constant βf shows temperature dependence. We use experimental value[74,75] of γ_s in hot and cold temperature and determine β and find that β is 1.29 times larger than that in the hot region. f is the number of ligand molecules bound on nanoparticle, which is dependent on temperature via the Boltzmann factor $\exp(-E_b/k_BT)$, where the binding energy taken as appropriate for citrate binding to gold nanoparticles, $E_b \approx -11kJ/mol$.[76] Multiplying both β and f in corresponding temperature, we get βf to be 50 for hot region and $\beta f = 300$ for cold region. For cross interactions between two particles at different temperature we take geometric mean of the respective βf.

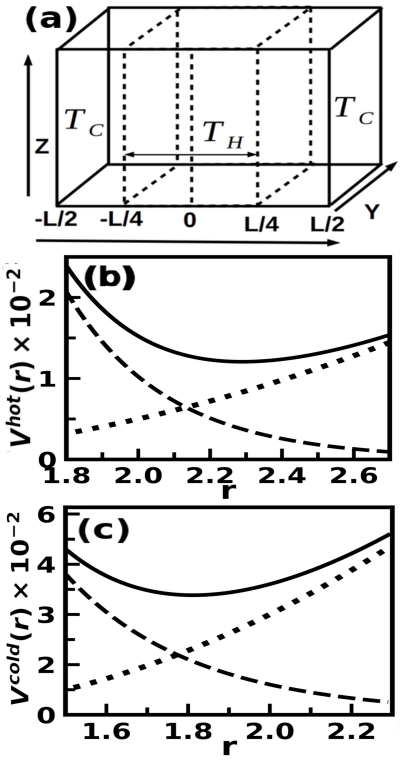

Figure 2.1: (a) Simulation box after creating temperature difference. $-L/4 < x < L/4$ is the hot region T_H and rest of the two side are in cold region T_C. (b-c) Potential $V(r)$ with pair particle separation r in hot region and cold region respectively: V_{tot}(Solid line), V_R (dashed line), V_A (dotted line).

2.3 Simulation details

We perform Brownian dynamics(BD) simulation on $N(=6400)$ colloidal particles of diameter $\sigma = (114nm)$ in an implicit aqueous solvent in a volume (V) of rectangular parallelepiped box of length L_x =39.5σ and $L_y = L_z$ =18 σ with the periodic boundary conditions in all three directions at the packing fraction $\eta = \frac{\pi}{6}\frac{N}{V}\sigma^3$ =0.26. The temperatures in the study are as follows: hot region at temperature T_H =373 K and cold region at temperature T_C =273K set along x axis. Each Brownian particle (i) position is updated according to Langevin's equation[77] (see details in Appendix A1) in the over damped limit with white noise:

$$\Gamma_\alpha \frac{d}{dt}\vec{r}_{i,\alpha} = \vec{\nabla}_i \sum_{j=1}^{N} V_i^{(\alpha)}(r_{ij}) + \vec{F}_{i,\alpha}(t) \tag{2.5}$$

Eq. 2.5 for ith particle could be discretized as[77]-

$$\vec{r}_{i,\alpha}(t+\delta t) = \vec{r}_{i,\alpha}(t) + \frac{1}{\Gamma_\alpha}\vec{\nabla}_i \sum_{j=1}^{N} V_i^{(\alpha)}(r_{ij})\delta t + \vec{R}_{i,\alpha}(\delta t) \tag{2.6}$$

Here α =(hot, H) and (cold, C) denotes the temperature regions in the simulation box. $V_i^{(\alpha)}$ is total potential for ith particle in the αth region with other particles j with distance $r_{ij} = (|\vec{r}_i - \vec{r}_j|)$, $V_i^{(\alpha)} = \sum_{j=1}^{N} V_A^{(\alpha)}(r_{ij}) + V_R^{(\alpha)}(r_{ij})$. The derivative $\vec{\nabla}_i$ is calculated with respect to the coordinate of the i-th particle. In our simulations, $\frac{e^2}{\epsilon\sigma}$ and σ are energy and length units, while $\tau_H(=\sigma^2/D_H)$ the time unit. $\vec{F}_{i,\alpha}$ in Eq. 2.5 is fluctuating force or random white noise chosen from Gaussian distribution with mean zero and variances $2D_\alpha\delta t$ on ith particle of αth type. In Eq. 2.6, $\vec{R}_{i,\alpha}(\delta t)$ is corresponding random displacement due to fluctuating force during time δt. Here δt is the integration time and D_α the Stokes-Einstein diffusion coefficient, given by $k_B T_\alpha/\Gamma_\alpha$ at temperature T_α, k_B the Boltzmann constant and $\Gamma_\alpha = 3\pi\eta_\alpha\sigma$ is viscous damping. The temperature dependence of viscosity is given in an empirical form, $2.761 \times 10^{-6} exp(\frac{1317}{T})$ Pa.s.[78] The discretized equation of motion is integrated with time step $0.0001\tau_H$. All the time dependent quantities are averaged over five different trajectories.

2.4 Structural Quantities

2.4.1 Pair correlation function

We calculate the probability distribution of separations between different pairs of particles, also known as the radial distribution function $g(r)$. It gives the probability of finding an atom around a central atom within a spherical shell of radius r to $r + \delta r$. We measure the minimum image separations r_{ij} for all the pairs of particles and find the histogram of these values with a bin width $\delta r = 0.1$[79] over the equilibrium/steady state configurations to find $g(r)$. Finally, average is taken over different independent trajectories.

2.4.2 Bond order parameter

We calculate different structural parameters in the steady state as functions of time. We take both cold regions for considering data of the cold region. We construct the distribution of bond orientation order parameter of order l defined as,[73]

$$q_l q_l(i) = \frac{1}{N_b(i)} \sum_{j \in N_b(i)} q_l(i).q_l(j) \tag{2.7}$$

where $q_l(i).q_l(j) = \sum_{m=-l}^{m=+l} (\frac{1}{(\sum_{-l}^{l} |q_{lm}(i)|^2)^{1/2}}) \cdot (\frac{1}{(\sum_{-l}^{l} |q_{lm}(j)|^2)^{1/2}}) \cdot q_{lm}(i) q^*_{lm}(j)$. Here $q_{lm}(i) = \frac{1}{N_b(i)} \sum_{j}^{N_b(i)} Y_{lm}(\theta_{ij}, \phi_{ij})$. Y_{lm} are the spherical harmonics. l is an integer and m goes from $-l$ to $+l$. (θ_{ij}, ϕ_{ij}) are orientation of bond between particle i and and its $N_b(i)$ neighbouring particles (j) within cut off distance up to the first minimum of the pair correlation function in the hot bulk system with respect to direction (x-axis) of temperature difference.

We consider solid-like connection c where orientationally ordered particles (i and j) within cut off distance up to the first minimum of the pair correlation function in the hot bulk system are connected, if $q_6(i).q_6(j)$ crosses a threshold value (=0.5).[72] Moreover, if a particle is connected with more than threshold (=7) number of particles within the cut-off distance, we consider it to be solid-like particle.[72]

We also define an average quantity $\bar{q}_{lm}(i)$, defined as follows, to determine the type of structure.

$$\bar{q}_{lm}(i) = \frac{1}{\tilde{N}_b(i)} \sum_{j \in \tilde{N}_b(i)} q_{lm}(j) \tag{2.8}$$

where, sum goes over $\tilde{N}_b(i)$ which contains all neighbors of particle i within cut off distance up to the first minimum of the pair correlation function in the hot bulk system plus the particle i itself. We define global rotational invariant quantity,

$$\bar{q}_l(i) = \sqrt{\frac{4\pi}{2l+1}\sum_{m=l}^{+l}|\bar{q}_{lm}(i)|^2} \tag{2.9}$$

We consider *l*= 4 and 6 in Eqs. 2.8 and 2.9 for each particle in a given configuration and construct $\bar{q}_4 - \bar{q}_6$ scatter plot as reported in the literature.[39]

2.4.3 Optimum number of structural clusters using the Machine Learning based auto encoder

We use the unsupervised machine learning (UML) algorithm(see details in Appendix A2) based on global rotational invariant bond-orientation order parameters combined with neural-network-based auto-encoders to detect optimum number of clusters of different structures in the aggregate as in Ref.[80] A schematic diagram of the UML is given in the Fig. 2.11 and detailed description is given in Appendix A2. We use $\bar{q}_l(i)$ as input to train encoder, where we use l=1,..,8. The main purpose to use auto-encoders is to project higher dimensional input in lower dimensional layer(called bottleneck) and finally reconstruct the input at decoder output. We train the network through minimizing MSE(mean square error) between input and output. Bottle neck captures important features of the input in low dimension after training. Then, we identify optimum dimension of bottleneck layer, which comes out c=2 in our case. We find $Y_1(i), Y_2(i)$ for each ith particle in the bottleneck layer. Then, we use a probabilistic method called Gaussian mixture models (GMM)[81,82] to cluster data in this two dimensional space using scikit-learn.[83] In GMM each particle is associated with a particular cluster in which cluster it shows highest membership percentage.

2.5 Results

At first the system is equilibrated at T_H. We subject the system to temperature difference as depicted in Fig. 2.1(a): hot region for $-L_x/4 < \mathrm{x} < L_x/4$ and cold regions $-L_x/2 < \mathrm{x} < -L_x/4$ and $L_x/4 < \mathrm{x} < L_x/2$. We show in Figs. 2.1(b) and (c) the dependence of $V_R^{(\alpha)}(r)$ and $V_A^{(\alpha)}(r)$ for the two temperatures considered in the simulations. The particles are assumed to take up the local interaction parameters and the noise as soon as they enter one region from another. We observe $V_R^{(\alpha)}(r)$

is dominant for lower r and $V_A^{(\alpha)}(r)$ dominant for larger r in both region. The total potential, $V^{(\alpha)}(r) = V_R^{(\alpha)}(r) + V_A^{(\alpha)}(r)$ has broad minimum. The minimum for the hot region is at 2.25 where as it is around 1.8 for the cold region.

Let us first consider the system in equilibrium at T_H and T_C. We show $g(r)$ data in Fig. 2.2(a) for both temperatures. The data confirm short-ranged order as in a liquid structure for both the cases. The first peak in both cases is located at separation less than the minimum of the interaction potential. We retrieve peaks of g(r) at the minimum of the potential only at extreme dilute limit. Thus, the liquid structure in the system is governed by the repulsive interaction.

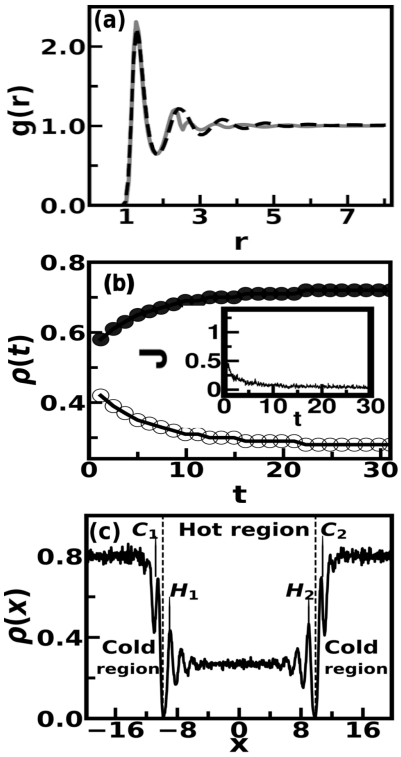

Figure 2.2: (a) Pair correlation function $g(r)$ over the distance r in the bulk system at hot temperature T_H(dotted black line) and at cold temperature T_C(grey line). (b) Density $\rho(t)$ in cold(solid circle) and hot(open circle) region. Inset: Total Flux J as a function of time. (c) $\rho(x)$ vs x plot in the steady state.

Next we take the equilibrium liquid structure at T_H and create temperature difference as shown schematically in Fig. 2.1(a). We ensure steady state of the system from density of particles ($\langle\rho(t)\rangle = \frac{2\langle N(t)\rangle}{V}$) at time t after creating temperature difference shown in Fig. 2.2(b) averaging over trajectories. We observe that the density in cold region increases with time and that decreases with time in hot region. The density in the cold regions fluctuates around 0.7 and around 0.3 in the hot region after $20\tau_H$. The steady state is also confirmed

from the total flux J (inset, Fig. 2.2(b)), given by the number of particles crossing the interfaces in a given time interval(=$0.03\tau_H$)) at the interfaces of hot and cold region, adding the two fluxes from hot to cold and cold to hot region. The steady state density profile of the system along the direction of temperature difference $\rho(x)$ in Fig. 2.2(c) shows the presence of inter-facial layers at the hot-cold junctions, C_1 and $C2$ in the cold part and there are layers H_1 and H_2 in the hot part of the box. The inter-facial width is about 6σ on both sides estimated from the density profile. The region away from interfaces $|x| < 6$ and $12.0 < |x| < L_x/2$ are defined as the hot and cold regions respectively over which density profiles are nearly uniform with values close to the corresponding bulk cases.

2.5.1 Structural changes

We observe structural changes in the system with progress in time. The snapshots for the system(half of the box from $0 < x < L_x/2.$) are shown in Fig. 2.3(a-b) for two different times (lower time, $6\tau_H$ and higher time, $540\tau_H$). We observe that the particles in the cold region gets ordered at higher time. To characterize this we use spherical harmonics of $l = 6$ order which distinguishes between liquid and crystal structure.[39,73] So, we concentrate on the bond orientation order parameter for $l = 6$ in the hot and cold regions using Eq. 2.7. We construct histogram $P(q_6q_6)$ of $q_6q_6(i)$ values for the particles in both hot and cold region. Fig. 2.4(a) shows the distributions for three different times. We find that in equilibrium at T_H, $P(q_6q_6)$ has peak around 0.3, which is indicative of disordered liquid phase,[73] consistent with the data in Fig.2(a). We observe that in the hot region (inset, Fig. 2.4(a)) the peak of $P(q_6q_6)$ shifts to slightly lower value, compared to the equilibrium one. The curves do not change much with time. Consequently, $P(q_6q_6)$ in cold regions shows time dependence. The distribution has peak around 0.1 at time 6 τ_H in Fig. 2.4(a) indicating liquid phase in colder region. At $t = 54\tau_H$, $P(q_6q_6)$ shows two peaks, around 0.1 and 0.8, suggesting coexisting liquid and crystal orders. At very large time(540 τ_H) $P(q_6q_6)$ is sharply peaked at 0.9,[73] suggesting crystal order, with a long tail extended to lower q_6q_6.

2.5.2 Growth kinetics

We show histogram of number of solid like connections per particle c as mentioned in the method, $P(c)$ in the cold regions computed over different trajectories with increasing time in Fig.2.4(b). We observe that at t=6τ_H, $P(c)$ is peaked at 2. $P(c)$ at t=54 τ_H shows two peaks, one around $c = 2$ and another a flat peak

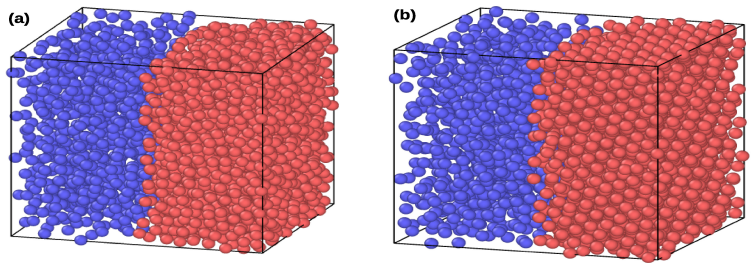

Figure 2.3: Snapshots of steady state configurations of half of the box ($0 < x < L_x/2$,) for two different times. Blue particles have interaction parameters corresponding to hot temperature T_H and red particles have parameters corresponding to cold temperature T_c. Panel (a) is shown for lower time ($6\tau_H$) configuration (b) higher time ($540\tau_H$) configuration. We observe ordering of red particles in the cold region at large time.

around $c = 10$. At t=$540\tau_H$, P(c) is sharply peaked around $c = 12$. Thus, the cold region has liquid like particles at low time. Solid like particles grow with time and coexist with liquid like particles. Eventually the particles are predominantly solid like for large enough time. We observe, on the other hand, in hot region (inset Fig. 2.4(b)) P(c) is peaked around 2 for all the time indicating that the hot region remains liquid like for all time.

The kinetics of structural growth in the cold regions is extracted through the crystal fraction θ_c, the ratio of solid like particles and number of particles present at a given time in the cold region and averaged over different independent trajectories. Bulk crystallization is described by the Avrami equation $\theta_c = 1 - exp(-kt^n)$,[84] where θ_c is transformed fraction of crystal at time t. Here, k the bulk crystallization rate constant, and n the Avrami exponent that depends on geometric factors, like shape of the particles and geometry of the crystal growth. We plot $\ln\langle Q\rangle = \ln(-(\ln(1 - \langle\theta_c\rangle)))$ versus $\ln t$ in Fig. 2.4 (c). We find three regimes of time dependence: (1) fitted with exponent n=0.82 and k=6.13 up to $18\tau_H$; (2) then fitted with n =4.2 and k=17.79 up to $90\tau_H$; and (3) finally to saturation. Such exponent is consistent with polyhedral growth in three dimensions.[85,86] The observation shows crystallization takes place in a two step manner from an initial slow to rapid crystal formation. The reason for two step nature is following: at first very few particles start to form solid like, formation of crystal nucleus is a slow event. Once critical crystal nucleus is formed, the crystallization spreads very first which reflects in the Avrami exponent.

We also examine growth of bond order in the cold regions. We construct to this end the spatial correlation of bond order parameter, $\phi_6(r) = \langle\frac{q_6q_6(r)q_6q_6(0)}{g(r)}\rangle$ where $g(r)$ is the pair correlation function, and average taken over different trajectories at a certain time. In crystal, the correlation is long-ranged, whereas

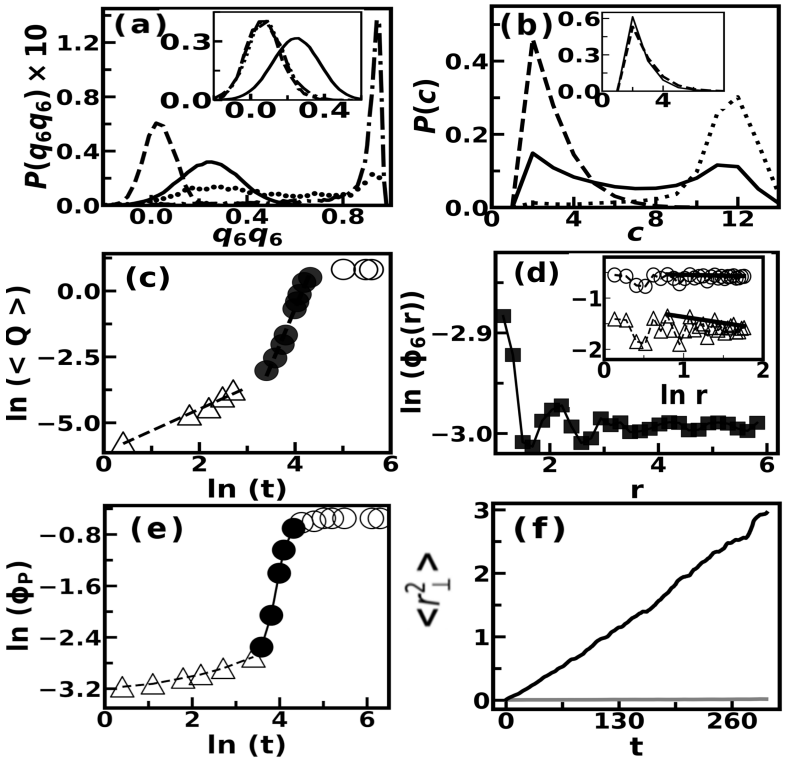

Figure 2.4: (a) $P(q_6q_6)$ distribution at Equilibrium(solid line), t = $6\tau_H$ (dashed line),$54\tau_H$ (dotted line), $540\tau_H$ (mixture of dashed and dotted line) after creating temperature difference in cold region (same for hot region inset picture). (b) P(c) vs c for different time t = $6\tau_H$ (dashed line),$54\tau_H$ (solid line), $540\tau_H$ (dotted line) for cold region and hot region(inset). (c) $\ln\langle Q\rangle$ vs t plot. Open triangles show lower time. solid circles denote middle time values while open circles show saturated portion. The dashed line is the fitted result. (d) $\ln\phi_6(r)$ as a function of r at $t = 6\tau_H$(close square). The solid line is guide to the eyes. Inset: Log-log plot of $\phi_6(r)$ vs r at $54\tau_H$(dotted line with open triangle), while the solid line shows algebraic fitting. Similar data at 540 τ_H (dotted line and open circle), along with algebraic fitting shown by the solid curve. (e) $\ln\phi_P$ versus $\ln t$ plot, where open triangle shows lower time, solid circle middle time and open circle for saturated results at higher time. The dotted line and the solid line show fitted lines in lower and middle time portion respectively. (f) MSD in cold region in plane yz (grey line) and MSD in plane yz (inside the interfacial plane (C_1 and C_2))(black line).

this decays exponentially to zero with r in a liquid.[87] The semi-log plots in Fig. 2.4(d) show that correlation for low time $6\tau_H$ decays to zero exponentially with r after peak at $r = 1.0$. However, at larger times the data fit better to an algebraic dependence on r for larger r, as shown in Fig.2.4(d)(inset) from the log-log plot. At $t = 54\tau_H$, (open triangle) the exponent of algebraic decay is -0.23(shown with deep line). The algebraic long-ranged order at $t = 54\tau_H$ is consistent with liquid-solid coexistence in Fig. 2.4(d).[88] The exponent at $540\tau_H$ (open circle) is -0.03, indicating a long-ranged orientational order as in crystal phase. The log-log plot of first peak ϕ_P of $\phi_6(r)$ at $r = 1.0$ for different times is shown in Fig. 2.4(e). We

observe three regimes of time dependence: (1) fitted with exponent 0.1 up to $18\tau_H$; (2) then with exponent 2.14 up to $90\tau_H$; and (3) finally saturation in time. The time span of these regimes suggests that the three regions correspond to three distinct spatial correlations in bond orientational order in the system, namely, liquid, liquid-crystal phase-coexistence and crystal.

We characterize the single particle motion in the cold region in terms of mean squared displacement (MSD) of the particles(Fig. 2.4(f)) in the plane parallel to the interface defined as, $\langle r_\perp^2 \rangle = \langle (\vec{r_\perp}(t) - \vec{r_\perp}(0))^2 \rangle$ where $\vec{r_\perp}(t) = y(t), z(t)$, ensuring that both $\vec{r}(t)$ and $\vec{r}(0)$ belong to the cold region. Here average is taken over initial position and the Brownian trajectories in steady states. We divide the in-plane MSD in two parts: 1) In the cold region away from the interfaces where the MSD does not show appreciable time dependence, consistent with crystallization. 2) MSD in the inter-facial planes (C_1 and C_2) where we observe that the MSD increases linearly in time at large times, indicating that the particles are diffusive in the interface.

2.5.3 Characterization of ordered phase in cold region

We perform machine learning calculations to find optimum number of clusters of different structure in the system in different regions. We train our network with $\bar{q}_l$(l=1,..,8) values, as input for the network for large time ($540\tau_H$) in the cold region. Y_1 and Y_2 are lower dimension bottleneck layer. We find two optimal clusters in lower dimension projection in Fig. 2.5(a), cluster1 shown in black and cluster 2 shown in grey. Thus, the system has two types of structures at large time in the cold region. On the other hand, the hot region shows only one cluster. We construct the scatter plot in $l = 4, 6$ plane using rotational invariant defined with Eqs. 2.8 and 2.9 to identify structures of the clusters in Fig. 2.5(a). Following the reports in literature,[39] we find in Fig. 2.5(b) that the cold region has predominantly BCC structure (cluster 1, Fig. 2.5(a)) at time $540\tau_H$ with a long tail along smaller values of $\bar{q}_4$ and $\bar{q}_6$, indicating liquid region (cluster 2, Fig.2.5(a)). We find in Fig. 2.5(c) hot region has liquid like structure at large time.

The in-plane (yz) density contours of the inter-facial layers C1 and C2 in Fig. 2.2(c) exhibit disordered liquid phase at time $6\tau_H$ (data not shown). The density contour plot at $540\tau_H$, however, shows regions of square symmetry with different orientations in Fig. 2.5(d). The mean $\langle q_6 q_6 \rangle$ for all in cold region and interfacial region are plotted with time in Fig. 2.5(e). We observe the growth of order in the interface takes almost similar time ($\approx 60\tau_H$) as that in the cold region. We observe

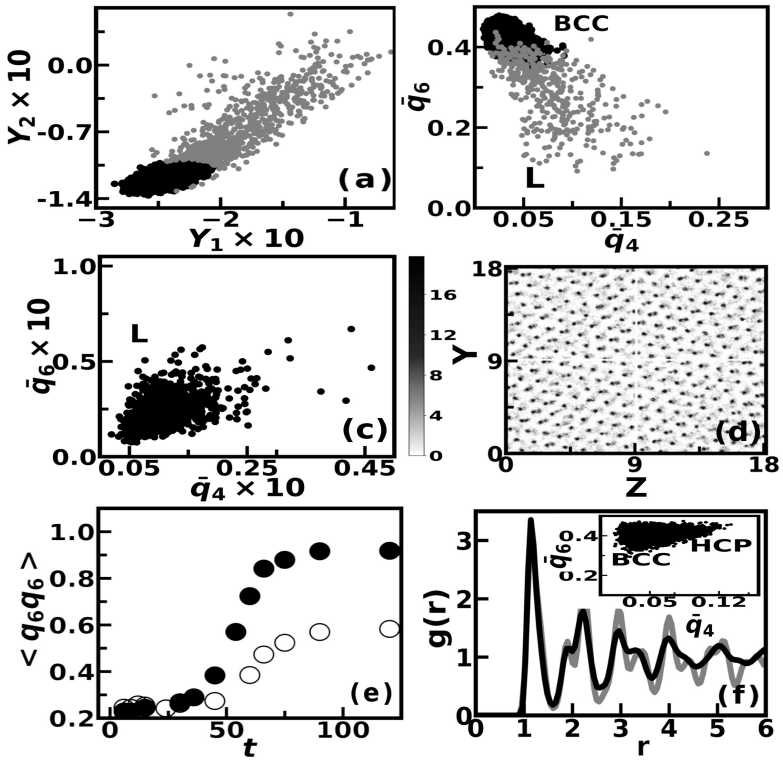

Figure 2.5: (a) Machine Learning lower dimensional ($Y_1 - Y_2$) plot for large time, cluster 1(black). cluster 2 (grey). (b) Scatter plot in $\bar{q}_4 - \bar{q}_6$ plane at large time in cold region, those cluster 1 (black) and cluster 2(grey) particles as in (a). (c) Scatter plot in $\bar{q}_4 - \bar{q}_6$ plane at large time in hot region. (d) Density contour plots in interfacial plane C1 in the cold region at t=540 τ_H (with colour bar on left). (e) $\langle q_6 q_6 \rangle$ versus time in cold region(close circle) and interfacial region(open circle). (f) $g(r)$ in bulk with temperature T_C, density$\rho(= 0.8)$ and interaction parameters as in the cold region (black line) and in system with interface in steady state cold region(grey line). Inset: Scatter plot in $\bar{q}_4 - \bar{q}_6$ plane for the bulk simulations.

$\langle q_6 q_6 \rangle$ in cold region saturates at 0.9 at large time, whereas it saturates around 0.6 at interface, denoting partial ordering compared to the cold region. This partial ordering in the inter-facial region is due to the proximity to the hot region.

We find from density profile in Fig. 2.2(c) that the density of the cold region is 0.8. We simulate a bulk system with $\rho(= 0.8)$ and temperature, interaction parameters and viscosity same as in the cold region without any temperature difference. Here, also we observe long-ranged order through $g(r)$ in Fig. 2.5(f), quite comparable to $g(r)$ in the steady state cold region(grey line). However, here we find coexistence of BCC and Hexagonal close packed(HCP) in orientational order, as revealed by the $\bar{q}_4 - \bar{q}_6$ scatter plot in inset, Fig. 2.5(f).[39]

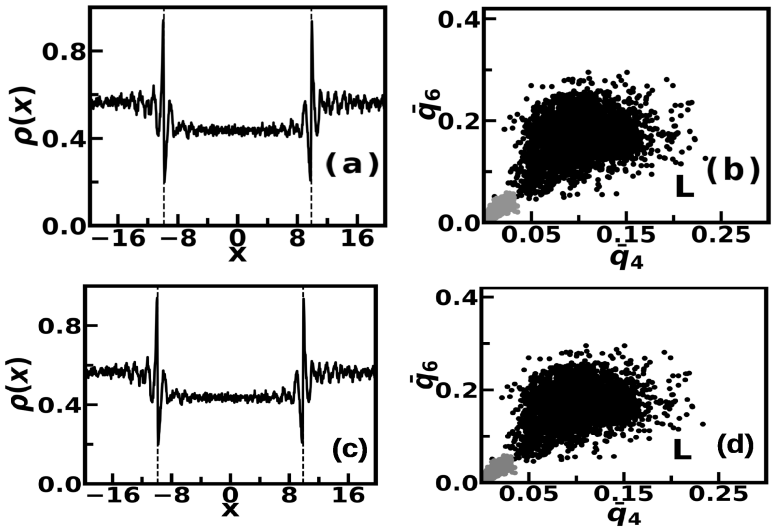

Figure 2.6: Data for the system where we keep interaction parameters same in both region as for cold temperature but maintain different temperature in different region(case 1): (a) Density profile $\rho(x)$, (b) Scatter plot in $\bar{q}_4 - \bar{q}_6$ plane at large time in cold region(black dot) and hot region(grey dot). Data for the system where we keep interaction parameters same in both region as for hot temperature but maintain different temperature in different region(case 2): (c) Density profile $\rho(x)$, (d) Scatter plot in $\bar{q}_4 - \bar{q}_6$ plane at large time in cold region(black dot) and hot region(grey dot).

2.5.4 Interaction versus kinetic effects

Note that temperature here affects both the particle interaction and kinetics. It is interesting to check which factor is important in stabilizing the crystal order in the system. We run to this end several simulations. (1) We keep interaction parameters the same in both regions as in the cold region but maintain different temperatures in two regions. The density profile in Fig. 2.6(a) shows hardly any hot-cold interface with little higher mean densities in cold region compared to hot region. Liquid order is shown in both region through $\bar{q}_4 - \bar{q}_6$ scatter plot in Fig. 2.6(b). The absence of order for this case in the cold region is due to less packing in the cold region compared to that in system with temperature dependent interaction parameters. (2) We keep interaction parameters the same in both region as in hot region of original system but different temperature in different region. Here also the observations are qualitatively similar to case (1) Fig. 2.6(c-d). (3) Further, we take temperature dependent interaction parameters along with the diffusivities as per the local temperature without considering explicit temperature dependence of viscosity. In these simulations, we observe similar crystal order and structure(scatter plot in Fig. 2.7).

We also take a binary mixture of particles with interaction parameters corre-

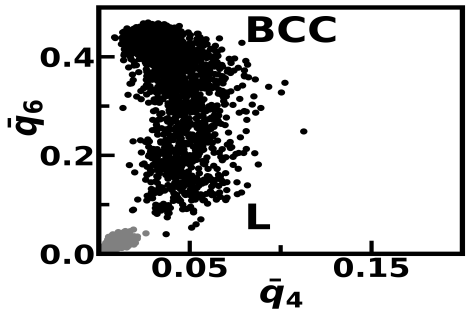

Figure 2.7: Scatter plot in $\bar{q}_4 - \bar{q}_6$ plane at large time in cold region(black) and hot region(grey dot) for the system where we take diffusivity as per the local temperature without considering the temperature dependent viscosity (case 3). The interaction parameters are temperature dependent.

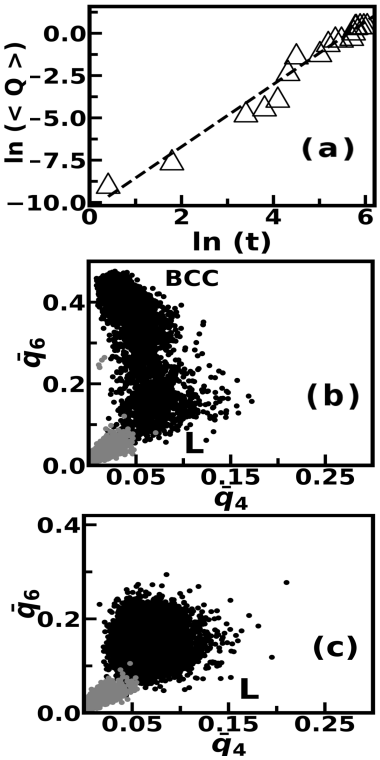

Figure 2.8: Data for the system with a binary mixture of particles with interaction parameters corresponding to the hot and cold region in the same ratio as in the steady state, in equilibrium at temperature T_C (case 4): (a) Scatter plot in $\bar{q}_4 - \bar{q}_6$ plane at large time in cold region(black dot) and hot region(grey dot), (b) $\ln\langle Q\rangle$ vs t plot. Data for the system with a binary mixture of particles with interaction parameters corresponding to the hot and cold region in the same ratio as in the steady state, in equilibrium at temperature T_H (case 5): (c) Scatter plot in $\bar{q}_4 - \bar{q}_6$ plane at large time in cold region(black dot) and hot region(grey dot).

sponding to the hot and cold region in the same ratio as in the steady state. We perform equilibrium simulations here at (4) T_c and (5) T_H starting from a random configuration. We observe phase separation between hot and cold particles at T_c. The $\bar{q}_4 - \bar{q}_6$ in Fig. 2.8(a) show BCC order among particles with parameters of the cold region, but the particles with parameters of the hot region remain liquid. Unlike the system with temperature difference, Fig. 2.8(b) shows that the growth of the crystal of cold particles takes place with a single Avrami exponent n =1.82. This is faster than early growth regime but slower than the intermediate regime of crystal growth in the system with hot-cold interface. So, temperature difference plays role in the rate of crystallization. Another notable thing here is phase separation and crystallization in equilibrium at temperature T_c can take place anywhere in the simulation box. This is quite different from the system with hot-cold interface where the region of crystal formation is pre-set. At T_H, we observe phase separation between hot and cold particles but there is no order (Fig. 2.8(c)). The absence of order can be attributed to higher particle diffusion at higher temperature. Thus, both the interaction and the kinetic effects via diffusivities governed by the local temperatures are important to set up the long-ranged order in the cold region of the system.

2.6 Discussions

We bring out a few subtle points:

Finite size effect- First, we note that the inter-facial width is large ($\sim 6\sigma$). This raises the question if finite size effects are important. For a smaller system with box length 16.75σ and the same particle number density, the density profile (Fig. 2.9(a) shows that the cold and hot region including the interface are formed. Although the mean densities in the hot and cold regions are similar as for the larger system size, the density profile shows larger fluctuations in the smaller system. However, we get similar structurally ordered phase shown by the $\bar{q}_4 - \bar{q}_6$ scatter plot in Fig. 2.9(b). Thus, the long-ranged order formation is not sensitive to system size.

Molecular Dynamics- Further, in BD simulations in the over-damped limit, we consider long time dynamics where local steady condition in different regions (hot and cold) is assumed. This can be relaxed in molecular dynamics (MD) simulations. We carry out MD simulations for our system where we re-scale the particle velocities with different temperature coefficients and assign the interaction parameters, depending on their location at a given instance. Temper-

ature profile along x direction is smooth as shown in Fig. 2.9(c) unlike abrupt temperature difference implemented in the BD simulations. We observe similar structural behaviour of the system as revealed from $\bar{q}_4 - \bar{q}_6$ scatter plots in Fig. 2.9(d). Thus, the BD trajectories within local equilibrium assumption lead to reasonably accurate description of the structural aspects in non-equilibrium cases.

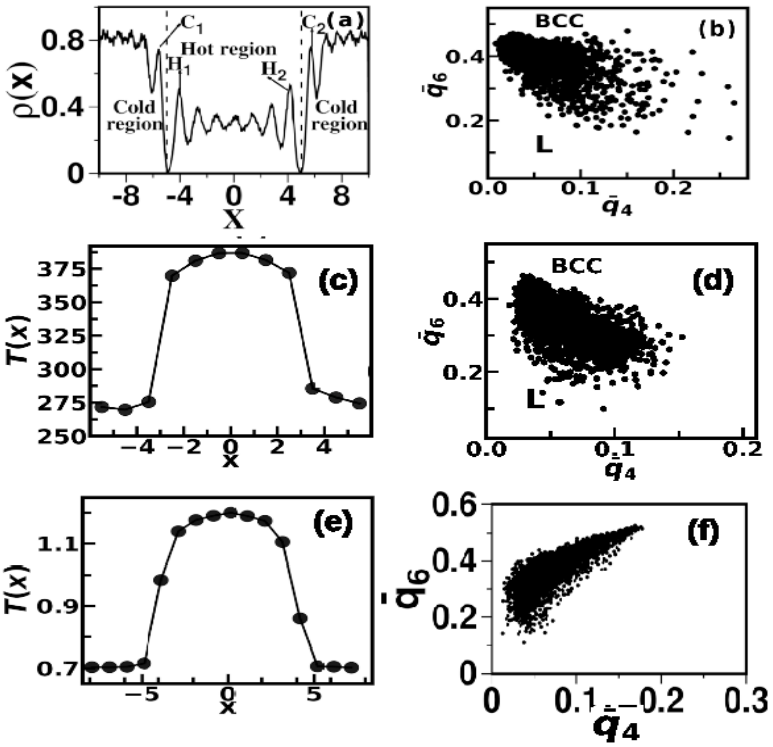

Figure 2.9: (a) Data for the system with lower number(4000) of particles. (a) Density profile $\rho(x)$. We observe that the density profile shows larger fluctuations compare to the large system case(main text). (b) Scatter plot in $\bar{q}_4 - \bar{q}_6$ plane at large time in cold region(black dot). (c) Temperature profile $T(x)$ in MD calculation. MD simulation of a Lennard Jones(LJ) system. (d) Scatter plot of MD simulation in $\bar{q}_4 - \bar{q}_6$ plane at large time in cold region. Ordering is similar as the BD calculations. Panel (e) shows temperature profile along x direction for LJ case. (f) Scatter plot in $\bar{q}_4 - \bar{q}_6$ plane at large time in cold region.

Lennard-Jones system- It may be worth to compare our results to recent simulations on non-equilibrium structure formation driven by different scalar activities in a system of Lennard-Jones(LJ) particles,[11] introduced by keeping particles in contact with different temperature baths. The model consists of (LJ) fluid with interaction potential of the form, $4\epsilon[(\frac{\sigma}{r})^{12} - (\frac{\sigma}{r})^{6}]$. Here ϵ is the strength of the potential and σ the diameter of the particle. The LJ system undergoes phase separation of particles according to their activities and crystallization for large density and the activity difference. This leads us to check if the long-

ranged order can be achieved by tuning parameters in much simpler Lennard-Jones(LJ) fluid in temperature gradient with MD simulation. We use temperature dependent strengths ϵ, namely, $T_H = 1.2, T_C = 0.7$ and $\epsilon_c/\epsilon_H = 1.5$ for hot and cold region respectively at bulk packing fraction 0.45. Our MD simulation data show temperature profile along x direction as in Fig. 2.9(e). We observe crystallization of the cold region of the system from $\bar{q}_4 - \bar{q}_6$ scatter plots in Fig. 2.9(f). However, the coexisting phases are HCP, face centred cube(FCC) crystalline phases and liquid. Thus, long-ranged crystalline order is possible even with thermophoretic LJ particles, suggesting that the exact form of the potential is not important to set the long-ranged order. However, the nature of crystal order may be different depending on the form of interaction. Clearly, the presence of scalar activity and thermal drive behave qualitatively in a similar way.

We also have studied steady state structural diagram in cold region in LJ system by changing relative interaction strength $\epsilon^* = \epsilon_C/\epsilon_H$ in hot and cold particles and also relative temperature $T^* = T_H/T_C$. We plot steady state structural diagram in Fig. 2.10 in $\epsilon^* - T^*$ plane. We denote the ordered state by S and liquid state by L in the diagram both in hot and cold region. We find hot region is always liquid (L) in steady state condition. The cold region shows $L \rightarrow S$ cross-over. For $\epsilon^* = 1$, we need large relative temperature difference to observe long range order formation in the cold region. But if we design particles such a way where relative interaction strength increases in cold region compared to the hot region, long range order start to emerge even for smaller temperature differences.

2.7 Conclusion

We have performed BD simulations in model systems in presence of hot-cold junctions considering temperature dependence of both the solvent viscosity and the potential of mean force between the particles. We observe crystalline order in the cold region where the kinetics of the growth of order in the cold region follows Avrami equation. The microscopic picture that emerges from our simulations suggests that the temperature dependent interactions play dominant role in realizing the long-ranged order in the system, the kinetics being faster in the presence of the hot-cold temperature junction. Our prediction may be verified by experiments on colloidal systems where the particle motions can be followed.[89] It will be worth to study the steady state phase diagram systematically. It may be noted that the exposed surface of a system depends on its structural order.

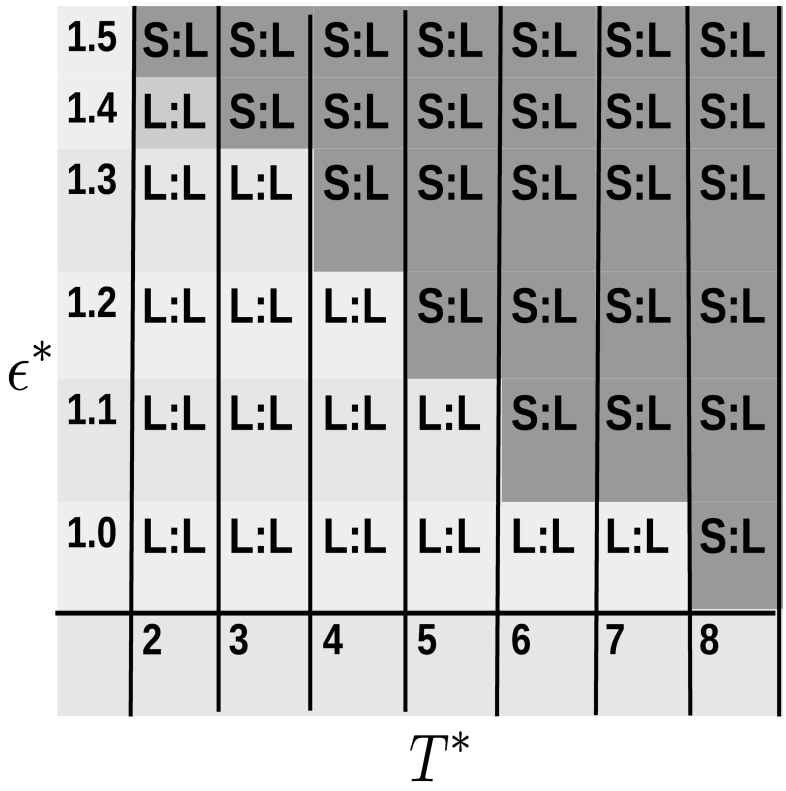

Figure 2.10: Schematic representation of different Steady state structural phases in cold and hot region for LJ fluid in $\epsilon^* - T^*$ plane. Symbol L and S denote liquid and ordered state respectively. Left side denotes the structure of cold region, right side for the hot region.

The presence of the long-range order in the system suggests that the surface area may be macroscopic and thus, useful for performing SERS measurements. Furthermore, we show that the formation of crystalline order holds for a large class of systems so that the exact form of the interaction potential does not seem to be important. This observation may help to guide the design of large surfaces for ultra-sensitive SERS and other surface-dependent applications.

Appendix

A1. Brownian Dynamics simulation details

Langevin equation describes the Brownian motion of a large and massive particle in a bath of solvent particles. The bath particles are much smaller and more numerous than the Brownian particles. The Brownian particles are much slower in timescale compared to the bath particles. The Brownian particles show relaxation of the initial velocity of the Brownian particle experiencing frequent collision with the bath particles. The forces on the Brownian particles consists of three parts: (1) frictional force proportional to the velocity $\vec{v_i}(t)$, in opposite direction, (2) negative gradient of total potential V_i coming due to other Brownian particles, and (3) randomly fluctuating force, $\vec{F_i}(t)$, which arises from collisions with surrounding particles. The random white noise $\vec{F_i}(t)$is the fluctuating force with mean zero and variance $\langle F_i^k(t)F_j^l(t')\rangle = 2D\delta_{kl}\delta_{ij}\delta(t-t')$ where k, l denote the cartesian components and D is the Stokes-Einstein diffusion coefficient, given by k_BT/Γ at temperature T. $\Gamma = 3\pi\gamma\sigma$ is viscous damping. The equation of motion of a Brownian particle of mass m is therefore written as:

$$\frac{d}{dt}(m\vec{v_i}) = -\Gamma v_i(i) + \vec{\nabla}_i \sum_{j=1}^{N} V_i(r_{ij}) + \vec{F_i}(t) \tag{2.10}$$

If we take single particle neglecting fluctuating force $\vec{F_i}$ Eq. 2.10 reduces to $\frac{d}{dt}(m\vec{v_i}) = -\Gamma v_i(i)$. We find that particle velocity relaxes with $v(t) = v(0)e^{-\frac{t}{\tau_r}}$, where $\tau_r = \frac{m}{\Gamma}$ is the velocity relaxation time. If Γ is very high(high friction in solvent) or $m \to 0$, the relaxation of momentum is instantaneous. We can neglect ($\frac{d}{dt}(m\vec{v_i}) \to 0$). In this limit we can arrive at overdamped limit of Langevin equation, which is also called Brownian Dynamics.

Each Brownian particle (i) position is updated according to discretized equation[77] in the over damped limit with white noise:

$$\Gamma\frac{d}{dt}\vec{r_i} = \vec{\nabla}_i \sum_{j=1}^{N} V_i(r_{ij}) + \vec{F_i}(t) \tag{2.11}$$

For discrete movement in small interval δt, random displacement due to fluctuating force $\vec{F_i}(\delta t)$ is incorporated in the equation of motion as:[77,79]

$$\vec{r_i}(t+\delta t) = \vec{r_i}(t) + \frac{1}{\Gamma}\vec{\nabla}_i \sum_{j=1}^{N} V_i(r_{ij})\delta t + \sqrt{(}2D\delta t)\vec{G} \tag{2.12}$$

where, $\vec{G}$ is an independent Gaussian random variable, with zero mean and unit variance. V_i is total potential for ith particle with other particles j with distance $r_{ij} = (|\vec{r}_i - \vec{r}_j|)$.

A2. Unsupervised machine Learning

We use the unsupervised machine learning (UML) algorithm with neural-network-based auto-encoders to detect optimum number of clusters of different structure in the aggregate following Ref.[80] An autoencoder is a neural network that is trained to perform the identity mapping, where the inputs of the network are reconstructed at the output layer. The network may be viewed as consisting of two parts: an encoder network, which performs a nonlinear projection of the input data onto a low-dimensional subspace(called bottle neck layer), and a decoder network that attempts to reconstruct the input data from the low-dimensional projection. A schematic diagram of the UML is given in the Fig. 2.11. We use global rotational invariant bond-orientation order parameters $Q(i) = \bar{q}_l(i)$ as input to train network. The dimension of input is here d. The input is reconstructed at output $Q^{'}(i)$ passing through in between layers with non linear connection.

The encoder learns a lower dimensional nonlinear projection in bottleneck layer which maintain salient features of input. Output is approximately reconstructed from bottleneck layer through decoder. This is done by training over ensemble of input samples. We have N particles in the system. We average over 1000 steady state configurations. So our total sample space is $N_s = 1000M$. We calculate for each sample $Q(i) = \bar{q}_l(i)$. Input dimension d=8 as (l=1,.,8). By training the autoencoder to perform the input reconstruction task over an ensemble of training examples, the encoder is forced to learn a low-dimensional nonlinear projection to bottle neck layer ($Y(i)$) that preserves the most relevant features of the data and from which the higher-dimensional inputs can be approximately reconstructed by the decoder.

Internal architecture- We set the number of nodes in the encoder and decoder hidden layers to 10d and use a hyperbolic tangent as the activation function, whereas a linear activation function is used for bottle neck and output layers as mentioned in the reference.[80] The internal parameters of the autoencoder is taken as follows: weights $W \equiv w_j$ and biases $B \equiv b_k$, are initialized with the normalized initialization i.e., the biases are initialized to zero, while the weights are drawn from a normal distribution with zero mean and variance

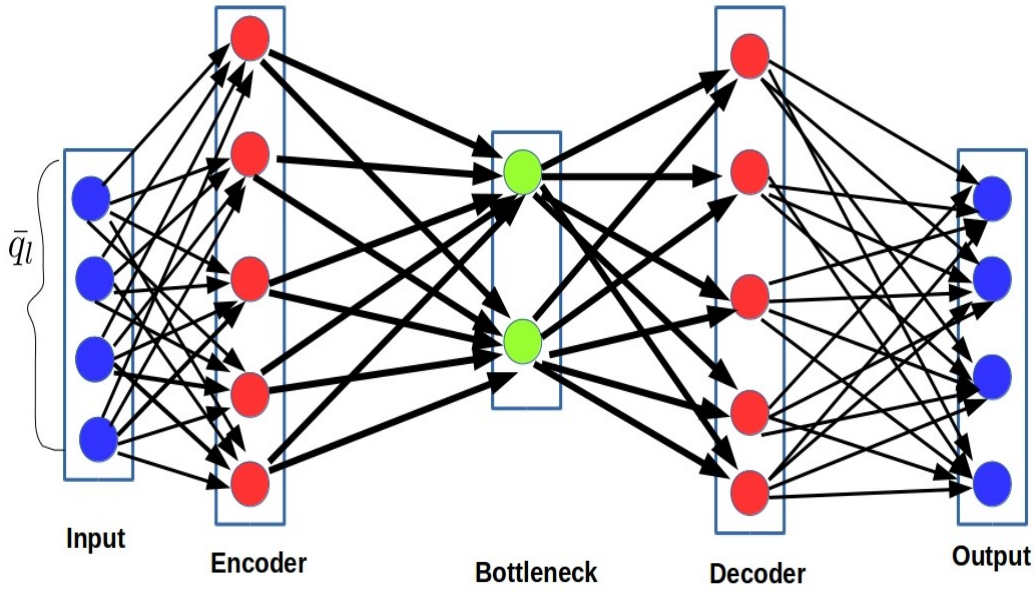

Figure 2.11: A schematic diagram of neural network based auto encoder used in the unsupervised machine learning

that depends on the size of the layers. These parameters are optimized by minimizing the reconstruction error(Mean Square Error(MSE)) of the input data over a training set of N training examples during the training. MSE is defined as $E = \frac{1}{N}\sum_{i=1}^{N_s} ||Q(i) - Q^{'}(i)||^2 + \lambda \sum_{j=1}^{M} w_j^2$. N_s is the total training sample and M is total number of weights. We set $\lambda = 10^{-5}$. The function is minimized using minibatch stochastic gradient descent with momentum using Keras open source software in Python.

Optimum number of bottleneck layer- Important part of the problem lies in the selection of dimension of bottleneck layer. We vary number of nodes c in the bottleneck, train the network, calculate MSE for each case. We plot MSE as a function of bottleneck node number. We obtain optimum node number by detecting elbow of the curve called L-method proposed by Salvador and Chan.[90] The dimension for the lower dimension subspace comes out c=2 for our case. For each particle i, 8 dimensional input features captures in two dimensional bottleneck Y_1, Y_2. Now We able to reduce degrees of freedom from $8N_s$ to $2N_s$ space. We project data from $8N_s$ to $2N_s$ using the trained network parameters.

Clustering in bottleneck layer- Now, in this two dimensional projection plane, we cluster the data using Gaussian mixture models (GMM)[83] with Bayesian Information Criteria (BIC).[81] GMM is a soft clustering method that assumes that each data are generated from a mixture of a finite number of Gaussian distributions with unknown parameters. These parameters are optimized iteratively using the

expectation-maximization (EM) algorithm to create a probability density function that agrees well with the distribution of the data. The number of Gaussian components in the mixture, N_g is measured by minimizing the BIC. BIC measures how well a GMM fits the observed data while penalizing models with many parameters to prevent overfitting. Each particle i is member to every cluster j with some membership percentage p_{ij} from the output of trained GMM and we attach each particle to a particular cluster with the highest membership value. This is done using sckiti-learn in python. Finally, the optimal number of clusters ($< N_g$) is found from entropy based clustering.[82]

Chapter 3 Long ranged order by thermoresponsive particles in hot region

3.1 Introduction

Here we further explore non-equilibrium structures created by thermoresponsive colloidal particles in presence of temperature gradient. In chapter 2, we develop a model for recent experiments[21] on ligand capped metal nano-particle systems which show formation of large clusters, useful for highly sensitive Surface enhanced Raman spectroscopy signals, in the cold region. Poly-N-isopropylacrylamide(PNIPAM) are thermoresponsive colloidal particles forming cross-linked microgel of entangled polymer networks that trap a large amount of water. These particles show potential applications in drug delivery,[91] tissue engineering, cell culture and photonic crystal.[92] The particle diameter increases due to trapped water at low temperature, while when heated, they release water resulting in reduced size in temperature window between $27^0C - 34^0C$.[93] This size change with temperature is reversible in bulk. But, experiments supported with simulations show hysteresis behaviour when microgel is placed at liquid-air interface.[94] Experiments further show that the size change of the particles can be tuned by random co-polymerization of PNIPAM with hydrophilic or hydrophobic species.[95] These thermo-responsive particles show ordered structure in low temperatures.[40]

In our model study, we subject the colloidal particles with temperature sensitive sizes under a temperature gradient to uncover structural changes in the steady state. The model system consists of particles interacting with the simple Lennard-Jones (LJ) interaction potential, $V_T(r) = \epsilon[(\frac{\sigma_T}{r})^{12} - (\frac{\sigma_T}{r})^6]$. Here ϵ is the strength of the potential which is independent of temperature. The

particle diameter σ_T is temperature dependent. $\sigma_T = \sigma_H$ at hot temperature and $\sigma_T = \sigma_C$ in cold temperature such that $\sigma_H < \sigma_C$. We study the model system using the Langevin dynamics simulations[79] in a box with the periodic boundary conditions in three directions. The only difference from the previous chapter, here we use underdamped limit of the Langevin equation. So that we can calculate temperature in the system using equipartition theorem from velocity of particles. We equilibrate the system at hot temperature and then we cool two ends leaving the middle region at the centre of box at the hot temperature at which the system is initially equilibrated as shown in Fig. 3.1(a). We ignore the hydrodynamic interactions which is a reasonable approximation for small volume fractions. We study the system for various size ratios of the cold and hot particles at a given temperature gradient. We characterize the structural order in the system by bond order parameter[72,73] in the steady state. We observe that with increase in diameter ratio, at first cold region gets ordered structure but hot region remains liquid. Beyond a certain size ratio, not only the cold region, but also the hot regions become ordered due to subtle interplay between packing in different regions in response to the thermal drift.

3.2 Simulation Details

The particle dynamics are computed via the underdamped Langevin equation of motion(see details in Appendix A1, chapter 2) of the ith particle with mass m at position $\vec{r_i}(t)$ at time t:

$$m_i \frac{d^2\vec{r}_{i,\alpha}}{dt^2} = -\zeta \frac{d\vec{r}_{i,\alpha}}{dt} - \nabla \sum_{j=1}^{N} V_i^{(\alpha)}(r_{ij}) + \vec{f}_{i,\alpha}(t) \tag{3.1}$$

Here α =(hot(H) and cold(C)) denotes the temperature regions in the simulation box. N is the total number of particles in the system. ζ is the friction coefficient. We ignore the temperature dependence of ζ in our calculation. This simplified assumption follows from chapter 2 where it is observed temperature dependence of viscosity has almost no importance in structure formation in presence of temperature difference. $V_i^{(\alpha)}$ is total potential energy of the ith particle in the α region with other particles j at a distance $r_{ij}(= |\vec{r_i} - \vec{r_j}|)$. For cross interaction between two different-sized particles, we use $(\sigma_H + \sigma_C)/2$. The components of $\vec{f_{i,\alpha}}(t)$ are the Gaussian white noise with zero mean and variance, $6\zeta k_B T_H \delta(t^{'} - t^{''})$ at hot temperature T_H and $6\zeta k_B T_C \delta(t^{'} - t^{''})$ in cold temperature T_C. k_B is the

Boltzmann constant. Here $\zeta = m\gamma$, where γ is the damping term due to friction.

In our simulations, ϵ strength of LJ potential is the unit of energy, σ_H the length unit and $\tau(= \sqrt{\frac{m\sigma_H^2}{\epsilon}})$ the time unit. We set $\gamma = 100$. The discretized equations of motion are integrated with time step 0.001τ. We perform simulation on $N(= 4000)$ colloidal particles in a volume (V) of rectangular parallelepiped box of length L_x =57.1 and $L_y = L_z$ =10 with the periodic boundary conditions in all three directions at the packing fraction $\eta = \frac{\pi}{6}\frac{N}{V}\sigma_H^3$ =0.36.

At first the system is equilibrated at T_H. We create sharp temperature gradient along x direction. A schematic diagram is given in Fig. 3.1(a). We thermostat the region (i) $-L_x/4 <$ x $< L_x/4$ with temperature T_H and (ii) regions $-L_x/2$ $<$ x $< -L_x/4$ and $L_x/4 <$ x $< L_x/2$ with temperature T_C as depicted in Fig. 3.1(a). The particle diameter changes according to the local thermostat region as soon as they enter from one region to other. We vary ratio of diameter in cold and hot particles $\sigma^* = \frac{\sigma_C}{\sigma_H}$. All the time dependent quantities are averaged over three different trajectories. We take both cold regions for considering data pertaining to the cold region.

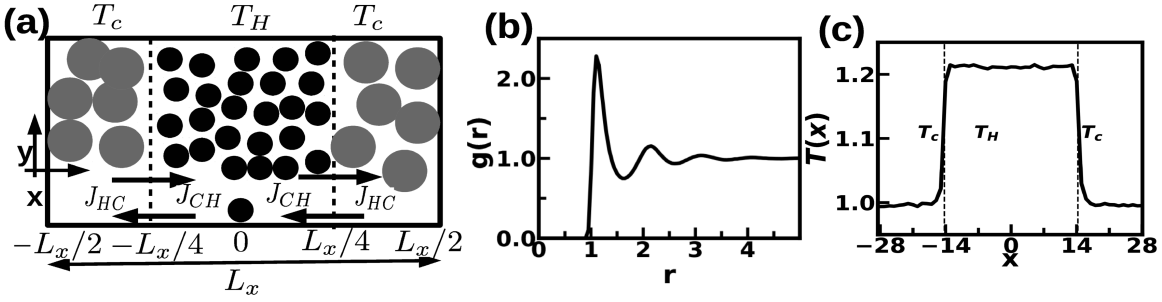

Figure 3.1: Schematic diagram of the model system. The diagram shows simulation box after creating temperature gradient. $-L/4 < x < L/4$ is the hot region T_H and rest of the two sides are in cold region T_C. The small black circles are particles in the hot region. The grey circles show swollen large size particles in the cold region. The black circles are particles in hot region. Arrows in two interfaces denote particle flux from hot region to cold region J_{HC} and cold region to hot region J_{CH}. (The z-axis not shown is pointing into the page). (b) Pair correleation function $g(r)$ over r in equilibrium at T_H. (c) $T(x)$ versus x plot at steady state after creating temperature gradient.

3.3 Results

We first consider the system in equilibrium at $T_H = 1.2$ and $\eta_{eq} = 0.36$. We characterize the equilibrium structure by the radial distribution function $g(r)$(see details in section 2.4.1, chapter 2). The $g(r)$ data in Fig. 3.1(b) shows short-

ranged order as in a liquid structure. Next, we create temperature gradient in the equilibrated system as shown schematically in Fig. 3.1(a) where cold region is maintained at $T_C = 1$. In our case $T^* = \frac{T_H}{T_C} = 1.2$. We take $\sigma^* = 1.8$.

We plot temperature profile $T(x)$(Fig. 3.1(c) from kinetic energy of the particles in a bin width of σ_H along the x direction in steady state. Fig. 3.1(c) indicates sharp temperature gradient in the system. In presence of sharp temperature gradient, there are two sharp interfaces in the system. We compute the flux J_{HC}, given by the number of particles crossing both the interfaces from hot to cold region in a given time interval (0.2τ) and the opposite flux J_{CH} as well. The flux directions are shown by arrows in Fig. 3.1(a). The flux difference, $\Delta J = J_{HC} - J_{CH}$ at both interfaces of the system are plotted in Fig. 3.2(a). The flux increases from negative values and saturates in zero ensuring steady state around 100τ. The negative value indicates that $J_{CH} > J_{HC}$. Thus, initially more particles are pushed out from cold region and accumulate in hot region than those crossing from the hot to the cold region.

We calculate the time dependent changes in the packing fraction with respect to the equilibrium condition η_{eq}, $\delta\eta_H(t) = \eta_H(t) - \eta_{eq}$ and similar data for the cold region $\delta\eta_C(t) = \eta_C(t) - \eta_{eq}$. Here $\eta_H(t)$ and $\eta_C(t)$ are the packing fractions at time t in the hot and the cold region respectively. We show the data in Fig. 3.2(b). $\delta\eta_H(t)$ increases initially and then saturates. On the other hand, $\delta\eta_C$ decreases for low times and then saturates. The steady values reach around 100τ.

3.3.1 Structural Changes

We repeat our simulations for different σ^* keeping $T^* = 1.2$ fixed and initial equilibrium liquid structure at T_H. We characterize the temporal evolution of the structure in terms of the time dependent distributions of bond orientation order parameter of order l defined as Ref.[73] Spherical harmonics of $l = 6$ order distinguishes between liquid and crystal structure.[39,73] So, we concentrate on the bond orientation order parameter for $l = 6$ in the cold and hot region using q_6q_6 as illustrated in Chapter 2, Eq. 2.7. Next we construct histogram $P(q_6q_6)$ of $q_6q_6(i)$ values for the particles in both cold and hot regions to observe the structural change at different times, shown in Fig. 3.2(c). We further calculate the global rotational invariant quantity[39]for each particle $\bar{q}_l(i)$(Eq 2.8, Chapter 2) and construct the scatter plot in $l = 4, 6$ plane in both cold and hot region to determine the type of structure.

We find that in equilibrium at T_H, $P(q_6q_6)$ has peak around 0.3, which is

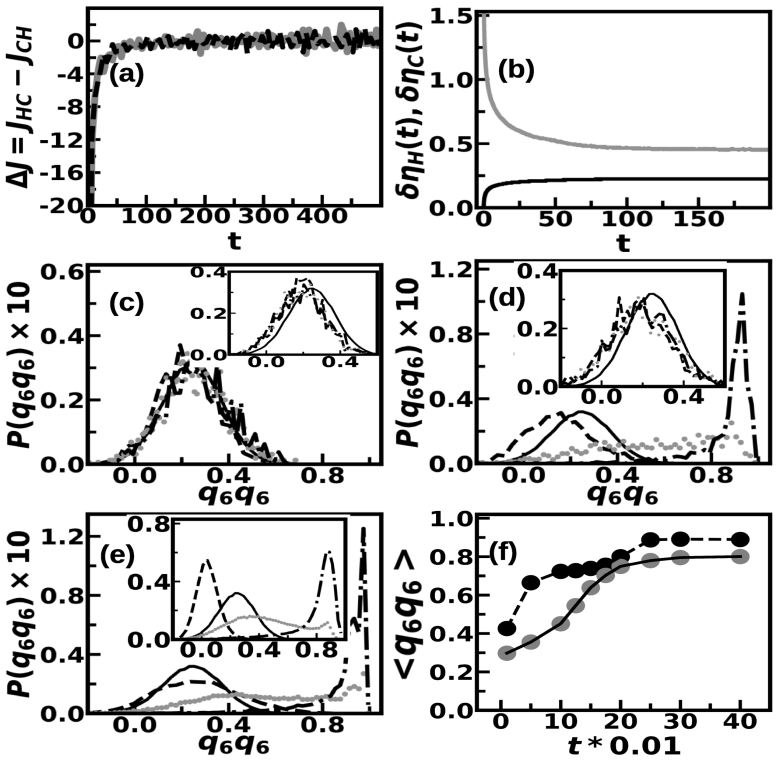

Figure 3.2: (a) Flux $\Delta J = J_{HC} - J_{CH}$ as a function of time in both interfaces for $\sigma^* = 1.8$. (b) $\delta\eta_H$, $\delta\eta_C$ versus t for hot region(black) and cold region(grey) for $\sigma^* = 1.8$. (c) $P(q_6q_6)$ distribution at Equilibrium(solid line), t = 0.5τ (dashed line),1000τ (grey line), $t = 4000\tau$ (mixture of black dashed and dotted line) after creating temperature gradient in cold region of $\sigma^* = 1.2$. Inset: $P(q_6q_6)$ distribution at Equilibrium(solid line), t = 0.5τ (dashed line),1000τ (grey line), $t = 4000\tau$ (mixture of black dashed and dotted line) after creating temperature gradient in hot region. (d) $P(q_6q_6)$ distribution at Equilibrium(solid line), t = 0.5τ (dashed line),1000τ (grey line), $t = 4000\tau$ (mixture of black dashed and dotted line) after creating temperature gradient in cold region of $\sigma^* = 1.6$. Inset: $P(q_6q_6)$ distribution at Equilibrium(solid line), t = 0.5τ (dashed line),1000τ (grey line), $t = 4000\tau$ (mixture of black dashed and dotted line) after creating temperature gradient in hot region. (e) $P(q_6q_6)$ distribution at Equilibrium(solid line), t = 0.5τ (dashed line),250τ (grey line), $t = 4000\tau$ (mixture of black dashed and dotted line) after creating temperature gradient in cold region of $\sigma^* = 1.8$. Inset: $P(q_6q_6)$ distribution at Equilibrium(solid line), t = 0.5τ (dashed line),1000τ (grey line), $t = 4000\tau$ (mixture of black dashed and dotted line) after creating temperature gradient in hot region. (f) $\langle q_6q_6 \rangle$ versus time in cold region(black circle) and hot region(grey circle) for $\sigma^* = 1.8$. The dotted and continuous lines are guides to the eyes.

indicative of a disordered liquid phase,[73] consistent with the data in Fig. 3.1(b). Let us consider the case of low σ^*(=1.2) in presence of temperature gradient. Here we observe in inset of Fig. 3.2(c), $P(q_6q_6)$ in hot region has a peak around 0.3 for all time shown indicating liquid order. Similarly cold region remains liquid for all time as shown in Fig. 3.2(c). The structural order changes at σ^*=1.6. Here we observe cold region has peak around 0.3 at low time 0.5 τ in Fig. 3.2(d). At an

intermediate time $t = 1000\tau$, $P(q_6q_6)$ shows broad peak, suggesting coexisting liquid and crystal orders. At larger time $t = 4000\tau$, $P(q_6q_6)$ is sharply peaked at 0.9[73] as for crystal order, with a long tail extended to low q_6q_6. On other hands hot region remains liquid for all times as shown in inset of Fig. 3.2(d). Further structural changes are observed at a higher σ^*(=1.8). Here $P(q_6q_6)$ in cold regions has peak around 0.3 at time 0.5τ in Fig. 3.2(e) indicating liquid order. At $t = 250\tau$, $P(q_6q_6)$ shows broad peak, suggesting coexisting liquid and crystal orders. At larger times in steady state, as shown in from Fig. 3.2(f), $P(q_6q_6)$ is sharply peaked at 0.9 with a long tail extended to low q_6q_6 indicating crystal order. We observe similar changes of $P(q_6q_6)$ in the hot region as well with time in inset of Fig. 3.2(e). The distribution at time 0.5τ is liquid like. It shows broad peak at time 1000τ. Finally at steady state it is sharply peaked around 0.85. We show $\langle q_l q_l(t)\rangle$ with average over the simulated trajectories in both regions in Fig. 3.2(f). We observe that $\langle q_6q_6\rangle$ increases in both regions with time. In cold region it saturates at 0.85 at large time, whereas it saturates around 0.75 in hot region.

We summarize the steady state structural changes in Fig. 3.3(d). We observe that for σ^* up to 1.2, both cold and hot region remains liquid in the steady state. The cold region shows long ranged order along with liquid order in the hot region at $\sigma^* = 1.3$. Both hot and cold regions show long ranged order after $\sigma^* = 1.6$. Following the literature reports,[39] we find in Fig. 3.3(a) for $\sigma^* = 1.2$ that cold region is mostly liquid(L) order with very few hexagonal closed pack (HCP) and face centred cube(FCC) crystalline orders in the steady state. The scenario changes for large $\sigma^* = 1.6$ as shown in Fig. 3.3(b). Here we observe the cold region has coexisting liquid(L), HCP and FCC crystalline orders in the steady state. We find in Fig. 3.3(c) for even higher $\sigma^* = 1.8$ that the hot region has coexisting liquid(L), HCP and FCC crystalline orders in the steady state. We also find that the cold region at steady state gets similar coexistence phases as hot region(data not shown). We calculate percentage of liquid, HCP and FCC orders (O_p) in cold region in the steady state in Fig. 3.3(e). We observe in Fig. 3.3(e) that for small diameter ratio $\sigma^* = 1.2$, predominant order is liquid in cold region. The scenario changes at $\sigma^* = 1.3$, the cold region has predominantly HCP order. The percentage of FCC type ordering increases and that of the HCP ordering decreases as σ^* increases more($\sigma^* = 1.6, 1.8$), whereas the liquid portion remains constant. In hot region (data not shown) for small $\sigma^*(= 1.2, 1.3)$ predominant order is liquid. The scenario remains same for a slightly higher ratio $\sigma^* = 1.6$. For more larger $\sigma^*(= 1.8)$, HCP ordering grows in steady state, while coexisting with small percentage of FCC and liquid orders.

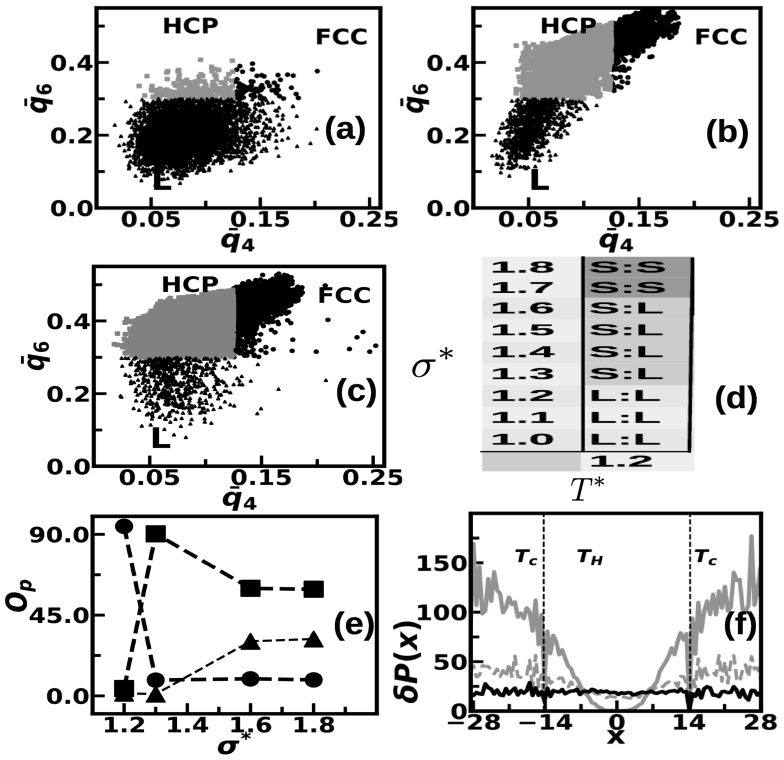

Figure 3.3: (a) Scatter plot in $\bar{q}_4 - \bar{q}_6$ plane at steady state in cold region for $\sigma^* = 1.2$. The black circles denote FCC structure, grey circles show HCP structure and black triangles are the liquid structure. (b) Scatter plot in $\bar{q}_4 - \bar{q}_6$ plane at steady state in cold region for $\sigma^* = 1.6$. (c) Scatter plot in $\bar{q}_4 - \bar{q}_6$ plane at steady state in hot region for $\sigma^* = 1.8$. The symbols in panels (b) and (c) are same as in panel (a). (d) Steady state structural diagram in $\sigma^* - T^*$ plane. Symbols L and S denote liquid and ordered state respectively. Left side denotes the structure of cold region, right side for the hot region. (e) Percentage O_p of different order versus σ^* in cold region. Liquid (circle), HCP(square), FCC(triangle). The dotted lines are guides to the eyes. (f) Relative Pressure profile $\delta P(x)$ versus x for different time at 10τ(grey continuous line), 50τ(grey dotted line) and steady state(black line).

Physically the emergence of the long ranged order in the hot region in the steady state condition can be understood from the increase in packing fraction. It may be noted that the system does not show the long ranged order in equilibrium at T_H. We measure pressure in equilibrium at T_H the average pressure, $P = 1.2$ and that in the steady state $P_{st} = 21.5$ for $\sigma^* = 1.8$ and $T^* = 1.2$. Pressure calculation details are given in Appendix A1. We plot the excess pressure profile $\delta P(x) = P(x) - P_{eq}(x)$ along the direction of temperature gradient x(Fig. 3.3(f)). $\delta P(x)$ is larger in cold region than the hot region at low time. This is so because the packing is larger in the cold region than in the hot region at lower time. Subsequently, $\delta P(x)$ falls in cold region and simultaneously increases in hot region. Finally the pressure profile reaches steady state flat value in the whole

simulation box. The imbalance in pressure is relaxed as the particles get pushed out from the cold to the hot region. This is also consistent with the time dependent changes in the packing fractions. Subsequent increase in packing in the hot region results in elevated pressure in the hot region till the mechanical pressure balance is achieved in the steady state. It is evident that high pressure in both the hot and cold regions in steady state leads to long ranged order in both regions.

3.3.2 Growth kinetics

The kinetics of growth of the ordered structure is extracted through θ_c, the ratio of the number of solid like particles to that of the total number of particles present at a given time and averaged over different independent trajectories. Bulk crystallization is described by the Avrami equation $\theta_c = 1 - exp(-kt^n)$,[84] where θ_c is transformed fraction of crystal at time t. Here, k is the bulk crystallization rate constant, and n the Avrami exponent that depends on factors, like shape of the particles and geometry of the crystal growth. We plot $\ln \langle Q \rangle = \ln[-(\ln (1 - \langle \theta_c \rangle))]$ versus $\ln t$ for various σ^*. We tabulate the results in Table 3.1 with fitting parameters exponent n and rate k. First, in Fig. 3.4(a) we compare the kinetics of the crystal growth of cold region for two cases: (1) $\sigma^* = 1.3$ the cold region first starts to emerge an ordered structure here, whereas the hot region remains liquid; and (2) $\sigma^* = 1.7$ both hot and cold region first shows long-ranged order at steady state. We observe that for both cases, crystal growth is in two-step fashion and initially slow to rapid growth at a later time. The data are tabulated in Table 3.1. The exponents are consistent with polyhedral growth in three dimensions[85,86] and similar to observation in chapter 2. The growth exponent increases with decreasing σ^* values. This is due to less packing in less σ^*(inset of Fig. 3.4(a)).

Then, we discuss kinetics in hot and cold regions for the case $\sigma^* = 1.8$ where both cold and hot regions show long ranged order. We find two distinct regimes of time dependence for both regions before saturation takes place for sufficiently large times(Fig. 3.4(b)). Thus, the formation of the long ranged order takes place in a two-step manner from an initial slow to rapid crystal formation for both regions. The growth is faster in hot region due to less packing as observed from Fig. 3.2(b).

3.3.3 Robustness of the ordered structures

We check if the long-ranged structures both in the cold and hot region is an artifacts of the constant volume ensemble that we have simulated. We perform a

σ^*	Region	n at lower time	n at large time	k at lower time	k at large time
1.3	Cold	0.32	1.61	3.27	12.51
1.7	Cold	0.19	0.95	2.1	6.21
1.8	Cold	0.07	0.53	1.94	3.33
1.8	Hot	0.56	1.59	4.46	11.5

Table 3.1: Avrami Exponent in different cases

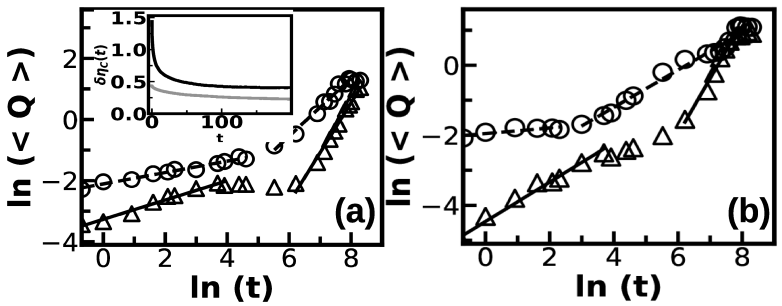

Figure 3.4: (a) $\ln\langle Q\rangle$ versus t plot in the cold region for $\sigma^* = 1.7$(open black circle), $\sigma^* = 1.3$(open black triangle). The fitted lines for $\sigma^* = 1.7$(black dashed line), $\sigma^* = 1.3$(black continuous line). Inset: $\delta\eta_C$ versus t for cold region of $\sigma^* = 1.7$(black) and $\sigma^* = 1.3$(grey). (b) $\ln\langle Q\rangle$ versus t plot for $\sigma^* = 1.8$. Open circle denotes kinetics for cold region. The dashed line is fitted line in cold region for both lower and larger time. Open triangle denotes kinetics for hot region. The continuous line is fitted line in hot region for both lower and larger time.

simulation where we maintain constant pressure(details in Appendix A2) same as the steady state pressure ($P = 21.5$) in the system allowing volume of the box to fluctuate while maintaining the temperature gradient. We follow similar procedure. At first, equilibrate the system in T_H, then create temperature gradient. Here, we observe the equilibrium configuration is ordered(snapshot shown in Fig. 3.5(b). We find that steady state structure in cold and hot regions also shows ordered state as revealed by the $\bar{q}_4 - \bar{q}_6$ scatter plot(data not shown). Thus, the enhancement of pressure in the steady state helps in experiencing order even in the hot region.

In constant pressure simulation, a difference is observed in kinetics of the long ranged order formation in steady state from equilibrium ordered configuration. We observe $\langle q_6 q_6\rangle$ over time in both hot and cold regions in Fig. 3.5(a). This quantity shows the structural change for both hot and cold regions as a function of time. The lower time change in cold region is shown in inset of Fig. 3.5(a) for clarity. The initial decrease in $q_6 q_6$ value indicates that the system becomes disordered at first after creating temperature gradient for both cold and hot regions.

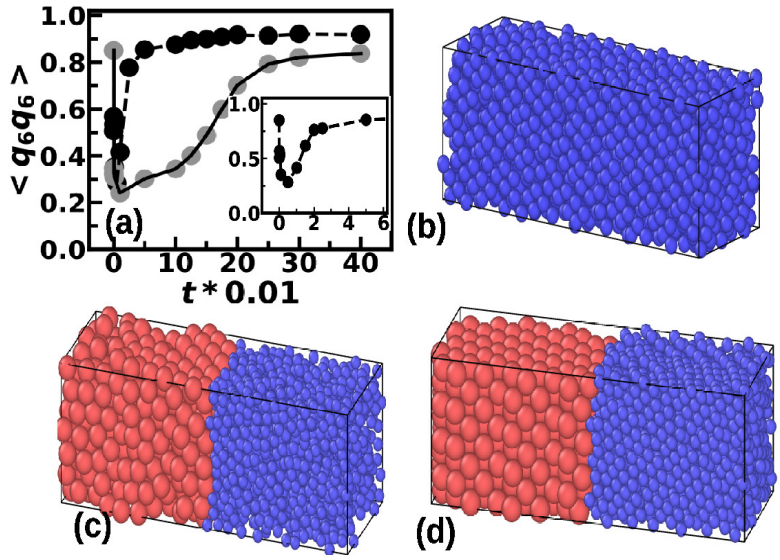

Figure 3.5: (a) $\langle q_6 q_6 \rangle$ versus time in cold region(black circle) and hot region(grey circle) for $\sigma^* = 1.8$ in constant pressure simulation in temperature gradient with pressure maintained at $P = 21.5$. The dotted and continuous lines are guides to the eyes. Inset: lower time portion of the cold region for better view. Snapshots of steady state configurations of half of the box $(0 < x < L_x/2,)$ for two different cases. Blue particles have interaction parameters corresponding to hot temperature T_H and red particles have parameters corresponding to cold temperature T_C. Panel (b) is shown for equilibrium configuration at T_H. (c) After creating temperature gradient at time $(150\tau_H)$. (d) Steady state configuration. We observe ordering of red and blue particles in the cold and hot region respectively at large time.

Structural order grows again in both regions with time. We provide snapshots for better understanding. In Fig. 3.5(b) equilibrium ordered configuration is shown. After creating temperature gradient the diameter of the particles in cold region increases as shown in Fig. 3.5(c-d) at $t = 150\tau$ and in steady state. The snapshot in Fig. 3.5(c) at $t = 150\tau$ shows disorder. Finally at steady state both regions regain long ranged order Fig. 3.5(d).

We also study if the finite size effects are important. We simulate a larger system with box length $L_x = 75.5, L_y = 11, L_z = 11$ and the same particle number density with $N = 6400$ particles. We use the parameter $\sigma^* = 1.8, T^* = 1.2$. Here, we get similar structurally ordered phases in both hot and cold regions shown by the $\bar{q}_4 - \bar{q}_6$ scatter plot in 3.6(a). Thus, the long-ranged order formation in the hot and cold region is not sensitive to system size.

We use another protocol to change the particle diameter in response to the local temperature in the system. We estimate that the velocity auto-correlation function(details in Appendix A3) at T_H decay to be ~ 100 simulation steps(0.1τ). We measure temperature profile $T(x)$ from kinetic energy of the particles in a

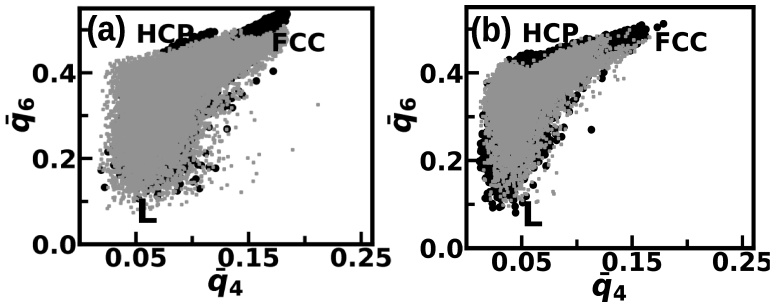

Figure 3.6: (a) Scatter plot in $\bar{q}_4 - \bar{q}_6$ plane at steady state in both cold(black) and hot(grey) region for $\sigma^* = 1.8$ for larger system size $N = 6400$. (b) Scatter plot in $\bar{q}_4 - \bar{q}_6$ plane at steady state in both cold(black) and hot(grey) region for $\sigma^* = 1.5$. The temperature gradient is created with different protocol.

bin width of σ_H along the x direction and averaged over 100 steps. We change the diameter linearly with slope $\frac{\sigma_H - \sigma_C}{T_H - T_C}$ as per the temperature profile after every 100 simulation steps. The steady-state structure of both hot and cold regions are shown in 3.6(b). We observe both the hot and cold region form long ranged order from $\sigma^* = 1.5$ for $T^* = 1.2$, qualitatively similar to the other protocol of diameter tuning by the local temperature.

3.4 Conclusion

The most intriguing result that we report here is the formation of crystalline order even in the hot region in addition to the cold region for sufficiently large σ^*, although there are differences in the steady state crystalline order and kinetics are different in the two regions. The order formation is due to an order of magnitude increase in the steady state pressure. The huge increase in pressure is connected to the flux of particles due to temperature dependent packing which competes with the thermal flux. Structural order in extreme pressure conditions is important in other contexts. One such example is interior of earth, which is in a constant out-of-equilibrium place where temperature and pressure are very high. The earth's core is abundant in crystalline materials like alumina, silica and iron.[96–98] Our model illustrates a simple case where high temperature crystallization can be studied in the laboratory and provide insight into the mechanism of formation of long-ranged order in extreme conditions in steady state.

Appendix

A1. Pressure calculation in the system

We further calculate stress tensor per particle for different timesteps. Stress tensor is defined for i-th particle as following: $S_{xy,i} = -m_i v_{x,i} v_{y,i} - W_{xy,i}(i)$. m is the mass of the particles. $v_{x,i}$ is the velocity of x direction. $W_{xy,i}$ is the virial contribution of the i-th particles coming from all possible interactions, $W_{xy,i} = \frac{1}{2}\sum_{j=1}^{j=N}(r_{x,i}F_{y,i} + r_{x,j}F_{y,j})$. It gives pairwise energy contribution where j loops over the particles i, $r_{x,i}$ and $r_{x,j}$ are the x component of positions of the 2 atom pair i and j. $F_{y,i}$ and $F_{y,j}$ are the y component forces on the 2 atoms i and j resulting from the pairwise interaction. The formula for total pressure P of a system in three dimension is $P = -\frac{\sum_i (S_{xx,i}+S_{yy,i}+S_{zz,i})}{3V}$. V is the volume of the region. Summation is over all particles in the region and average is taken over different trajectories. Pressure can also be calculated along a particular direction for a group of particles. Here we calculate pressure along temperature gradient direction x, P. We sum over the stress tensor of particles belonging to a strip of width δx along (x-direction) and divide the number by the volume of the strip. We take average over steady state configurations.

A2. Constant Pressure Simulation

We use Berendsen barostat isotropic coupling in the system to maintain the pressure. In each step we measure instantaneous average pressure P in the whole system and $\mu(t) = 1 - \frac{K\delta t}{\tau_P}(P^{'} - P(t))$. Here $P^{'}$ is the desired pressure we want to maintain in the system, K is the isothermal compressibility and τ_P is the relaxation time of the barostat. We take $K = 1$ and $\tau_P = 1000\delta t$[99] in the calculation. We scale the box length in each direction with $\mu(t)$ in each step. We follow a similar procedure where we equilibrate the system at T_H with $P^{'} = 21.5$, then create a temperature gradient along x direction. In the temperature gradient set up, thermostating of hot and cold region length is also scaled with $\mu(t)$ as well in each step.

A3. Velocity Autocorrelation

We calculate velocity autocorrelation at T_H. We measure $v_i(t_0)$ at time t_0 and $v_i(t_0 + \Delta t)$ at $t_0 + \Delta t$ for ith particle. We measure $C(\Delta t) = \langle v_i(t_0)v_i(t_0 + \Delta t)\rangle_{i,t_0}$ for different Δt. We take average over different time origins t_0 and over different particles. The velocity autocorrelation time is estimated from the first fall of correlation to zero.

Chapter 4 Motion of fluid droplets driven through a face mask

*

4.1 Introduction

Using face mask (FM) has been commonplace much beyond the usual medical purpose,[100] since the COVID-19 pandemic. The World Health Organization (WHO) mandates the use of FM to prevent the spread of COVID-19.[101] By now it is established[44,102,103] that the SARS-COV-2 virus responsible for COVID-19 is air-borne, like many other air-borne diseases, namely, tuberculosis, pneumonia and so forth. FM is the simplest measure to prevent spreading of any air-borne disease[41,103,104]by intercepting respiratory droplets of micrometer size, emitted when an affected person talks, sneezes or coughs. Respiratory micro-droplet propagation through air has been intensively studied.[41,105–108] However, relatively much less is known about micro-droplet movement through an FM.

FMs are typically made of fabric materials of entangled polymeric networks,[102] which allow essential molecules to be exchanged with the atmosphere and the human body but stop the movement of larger particles.[49,102] There are several layers in these FMs. The fibre diameter of filtration layer is about a few micrometers[109–112] with volume fraction typically less than 30%.[109] They capture 95% of the micro-droplets. The micro-droplets larger than the mean pore size are stopped due to geometrical constraints. The smaller micro-droplets are captured through interception, diffusion, and electrostatic attraction.[44,45,110]

*based on publication "Model studies on motion of respiratory droplets driven through a face mask". Rahul Karmakar, Aishani Ghosal and Jaydeb Chakrabarti; EPL, 141 (2023) 27001 ; doi: 10.1209/0295-5075/acaf9f

Such capture is the essence of an FM. But they show reduction in efficiency in humid conditions due to charge loss.[46] In search for stable FM performances, different possibilities are explored which include, for instance, using tribo-electric generators,[44,47,48] mixture of fabrics with different compositions,[49] and multiple layers.[42] Nano-fibres[45] and metal-organic framework filters[50,51] are shown to be promising route for better FM. However, they are plagued with breathing difficulty due to pores of nano-meter sizes. Reduction of leakage through FM is also necessary for better efficiency.[113]

Given this backdrop, theoretical understanding of various aspects of FM network to control the efficiency of intercepting micro-droplets would be highly imperative. A numerical study using the continuum fluid dynamics equations suggests that the droplet movement is a combined effect of capillary action and breathing force inside the FM.[114] At a more microscopic level, one may consider the respiratory droplets as colloidal particles moving through a porous polymeric network structure. Particle movement through a polymer network has been widely studied[115–120] due to its importance in intra-cellular transport, fluid rheology, materials engineering and so forth. It is reported that polymer networks are typically viscoelastic and heterogeneous in nature and it affects tracer movement[116] leading to non-Gaussian displacement distribution and sub-diffusivity.[120] It is also observed that the movement can be tuned with different network properties like network rigidity, binding affinity of tracer with network and tracer size.[115] Higher rigidity and affinity result in slower motion or caging behavior for tracer movement inside polymer network. Polymer mobility also affects tracer movement compared to frozen polymer network.[120]

In case of FM there are a few important aspects: (1) The WHO recommends that mask should be made up of three layers:[42,43] a polar material like cotton layer inside towards mouth and hydrophobic material in the middle and the outermost layers.[43,44,121] (2) The penetration of the droplet inside the porous mask also depends on the wettability of the fabric materials by the micro-droplets.[122] (3) It is necessary to consider breath-ability, an indicator of resistance to airflow by the mask while breathing and given in terms of the pressure drop inside the mask during airflow.[49] The average pressure difference in normal breathing is found to be around 2.5 ± 0.4 Pa.[49] We study a model to understand these aspects at a qualitative level. A schematic of the model is shown in Fig. 4.1. The FM is modelled in terms of a network of polymeric strands with two different kinds of beads of micrometer size.[109] The beads have low volume fraction so that there is sufficiently large void spaces (nearly 80%),[109] to allow exchange of small

molecules easily. One class of beads (h-beads) are taken to mutually interact more strongly than the other class of beads (p-beads). The h-beads mimic hydrophobic species those are known to collapse[38,52,53] and ensure strong interpenetration of the polymer strands forming network. The network is under asymmetric confinement, consisting of walls, each of which is having favourable interaction with a given type of bead. One wall preferentially interacts with h-beads, called the h-wall at $z = 0$ and the other one interacts favourably with p-beads denoted as the p-wall at $z = z_P$. This serves as a model for the three layered model suggested by WHO.[43] Our attention is specifically on the composition of the middle layer. We treat the micro-droplets as tracer colloidal particles (TCP) smaller than the typical pore size of the network but slightly bigger than the polymer beads. The shape and size changes of the droplets are ignored in this simple level of description. The p-beads interact more strongly with TCPs. This corresponds to the wettability of the network by the micro-droplets. The TCPs move from one wall to the other through a heterogeneous media in the presence of pressure difference needed for breath-ability. The pressure difference is modelled in terms of a force having maximum value F_0 at the h-wall and vanishing at the p-wall. We choose F_0 that creates pressure drop across the walls comparable to the experimental value[49] under a normal breath-ability condition. Our focus is on the factors which control the capture of the TCP below the natural pore size.

We study the motion of the polymeric beads and the TCPs using the Langevin dynamics simulations.[123] The equation of motion consists of the inertial term, the interaction forces, the drag force due to medium and drive force only on the TCPs. In case of polymeric beads, we consider the force arising from the elasticity but ignore the drive force compared to the elastic force. It may be noted that in this description, the dispersing medium is not considered explicitly, but taken in terms of drag force. The volume fraction of the TCPs ($\sim 26\%$) is also low as that for the polymeric beads($\sim 21\%$) so that we ignore the hydrodynamic forces for the beads and TCPs. Let us consider the movement of the TCPs from h-wall to p-wall. The fraction of tracer particles reaching the p-wall is the permeation P through the mask, while the efficiency of the mask $e = 100 - P$. We find that the permeation of the TCPs is an activated process, the energy landscape responsible for the activated process being governed by the TCP and p-bead interaction. Large activation barrier leads to a lower P and hence, larger e. We study the efficiency of intercepting the TCPs, fixing size, the driving force and the ambient temperature while varying composition of the polymeric strands, TCP interaction with the p-beads, network rigidity and confinement size. We find

that a 50:50 mixture of polymeric beads and stronger TCP and p-bead interaction give better efficiency. Mask efficiency linearly increases with increasing network rigidity and with decreasing confinement size. These may be helpful to design a mask with large efficiency ensuring normal breath-ability condition.

4.2 Model potential

The FM consists of such identical strands. Each polymeric strand is composed of two kinds of beads of the same diameter σ and mass m in a given h:p ratio, randomly distributed over the strand. The non-bonded interaction between two monomers i and j with separation r_{ij} is taken through the Lennard-Jones(L-J) 12-6 potential:

$$V_{\alpha\beta}(r_{ij}) = 4\epsilon_{\alpha\beta}[(\frac{\sigma}{r_{ij}})^{12} - (\frac{\sigma}{r_{ij}})^{6}], r_{ij} < 3\sigma \tag{4.1}$$

Here $\alpha(= h, p)$ and $\beta(= h, p)$ stand for the bead types and r_{ij} is separation between two beads. The bonded interaction corresponding to stretching between two neighbouring beads at separation r_{ij}:

$$V_{bond}(r_{ij}) = \frac{1}{2}k_b(r_{ij} - r_0)^2 \tag{4.2}$$

where $r_0 = 1.5\sigma$ is the equilibrium distance between monomers and k_b the force constant. The change in bond angle costs energy:

$$V_{angle}(\theta) = \frac{1}{2}k_\theta(\theta - \theta_0)^2 \tag{4.3}$$

where k_θ the force constant and $\theta = \cos^{-1}(\frac{\vec{r}_{ij}\cdot\vec{r}_{jk}}{|\vec{r}_{ij}||\vec{r}_{jk}|})$ is the angle produced by three consecutive monomers i,j,k and θ_0 is equilibrium angle, set to 114 degrees.[124] We consider a rigid network where the elastic deformation of any kind costs a lot of energy and ignore the distinction between these two elastic constants. Thus, we take $k_b = k_\theta = k$ to reduce the number of variables.

We place the polymeric system within two walls: The h-wall interacts with a bead via the L-J 9-3 potential:

$$V_{f,wh}(z_i) = \epsilon_{f,wh}[\frac{2}{15}(\frac{\sigma}{z_i})^9 - (\frac{\sigma}{z_i})^3] \tag{4.4}$$

Similarly, p-wall interacts with a bead :

$$V_{f,wp}(z_i) = \epsilon_{f,wp}[\frac{2}{15}(\frac{\sigma}{z_P - z_i})^9 - (\frac{\sigma}{z_P - z_i})^3] \tag{4.5}$$

Here $f = (h, p)$ stands for the bead type and z_i is the z-coordinate of i-th particle. The σ values for all the interactions are taken to be the same but $\epsilon_{h,wh} > \epsilon_{p,wh}$ and $\epsilon_{p,wp} > \epsilon_{h,wp}$.

The TCPs interact with each other with strength $\epsilon_{tr,tr}$. The strength are $\epsilon_{tr,h}$ and $\epsilon_{tr,p}$ for interaction of TCPs with h and p beads. They interact with two walls through the L-J 9-3 potential with parameters $\epsilon_{tr,wh}$ and $\epsilon_{tr,wp}$ for h and p walls respectively. We choose them to interact more favourably with the p-beads and the p-wall than the h-beads and the h-wall respectively so that $\epsilon_{tr,wp} > \epsilon_{tr,wh}$. We further take force over a TCP, $F(z) = F_0(1 - z/z_P)$.

We take ϵ_{hh} as unit of energy. The unit of mass is the mass of water of density 1 gm/cm^3 in a sphere of diameter 1 μm. The bead diameter (σ =1 μm)[109–112] is the unit of length. We fix dimensionless $\epsilon_{pp} = 0.33$(1/3 of ϵ_{hh}) while the cross interaction between h and p monomers is taken to follow the Berthelot mixing rule. We fix dimensionless wall particle interactions, $\epsilon_{h,wh} = 1.0$, $\epsilon_{p,wh} = 0.033$, $\epsilon_{p,wp} = 0.33$ and $\epsilon_{h,wp} = 0.033$. For these choices of interaction parameters, the polymeric network is uniformly spread throughout gap between two walls as shown in Fig. 4.2(a). The dimensionless L-J energy parameters for TCPs: $\epsilon_{tr,tr} = 1.0$, $\epsilon_{tr,wh} = 0.033$, $\epsilon_{tr,wp} = 1.0$. Mass of the polymeric bead particles is taken to be that for water droplet of diameter σ. Similarly, mass of the tracer particles is that for a water droplet of diameter σ_{tr}. We vary several parameters: $\bar{\epsilon} = \epsilon_{tr,p}/\epsilon_{tr,h}$, the network rigidity k and the confining length z_P. We perform simulations for various reduced temperature $T^* = \frac{k_B T}{\epsilon_{hh}}$.

4.3 Simulation details

The particle dynamics are computed via the under-damped Langevin(see details in Appendix A1, chapter 2) equation of motion of the ith particle with mass m_i at position $\vec{r_i}(t)$ at time t:

$$m_i^\alpha \frac{d^2\vec{r_i}^\alpha}{dt^2} = -\zeta_i \frac{d\vec{r_i}^\alpha}{dt} - \nabla \sum_j V^\alpha(\vec{r_i}^\alpha - \vec{r_j}^\alpha) + \vec{f_i^\alpha}(t) + \vec{F_i}^\alpha \tag{4.6}$$

where α is the particle type. α can be either the polymer beads or the TCP. ζ_i^α is the friction coefficient. V^α is the sum of all the relevant interactions for a given particle type. For the network beads, we consider bonded and non-bonded

interactions with other network beads, TCPs and the walls and set $\vec{F}_i^{\alpha} = 0$. For TCPs we consider interaction with other TCPs, network beads, the wall and in addition the external force, $\vec{F}_i$. The components of $\vec{f}_i^{\alpha}(t)$ are the Gaussian white noise with zero mean and variance, $6\zeta_i^{\alpha} k_B T \delta(t^{'} - t^{''})$, where k_B is the Boltzmann constant, and T the temperature. Here $\zeta_i^{\alpha} = m_i^{\alpha}\gamma$, where γ is the damping term due to friction of the network.

We perform simulation using the LAMMPS package.[125] Using the values of mass m, σ and ϵ_{hh}, we estimate a time scale, $\tau(= \sqrt{\frac{m\sigma^2}{\epsilon_{hh}}}) \sim 0.35$ millisecond. The time step for integration is taken 0.001τ. Damping term is taken as $\frac{1}{\gamma} = 10\tau$. All the quantities are averaged over five different independent trajectories each 6500τ long. We take $L_x = 30\sigma$ and $L_y = 20\sigma$, in x- and y- directions respectively with the periodic boundary conditions (PBC) and no PBC in z-direction.

We create an interpenetrating polymer network confined by h and p-wall at first. The network consists of 27 identical polymeric strands, each having randomly distributed 50 monomers in a number ratio h:p. Packing fraction of total polymeric beads in our model $\eta = \frac{\pi}{6}\frac{N}{V}\sigma^3 = 0.21$. It denotes almost 80% is voids in the system, which is reasonable as real situation.[109] Then we insert TCPs through Grand Canonical Monte Carlo(GCMC) at a chemical potential and temperature corresponding to packing fraction (0.47) in bulk liquid phase near the h-wall(see details in Appendix A). We exert external force on TCPs and study their motion through the network medium from h-wall to p-wall. For $\sigma_{tr} = 1\mu m$, $< N_{tr} >= 600$, $F_0 = 1$ creates pressure drop ~ 1 Pa across the walls which is comparable to the experimental value[49] under a normal breath-ability condition. We restrict to the range, $F_0 = 1 - 10$.

The network structure is characterised by computing the inter-strand correlation function among the beads belonging to different strands, $C(r)$. This is calculated from the number of beads, belonging to two different strands, within a separation r to $r + dr$, normalized by the corresponding shell volume and averaged over configurations. $C(r)$ gives information on how the bead in a given strand is surrounded by beads of the other strands and hence, the peak height in $C(r)$ at r=1 gives an estimate how the chains are linked among each other. While calculating distance between two beads, we do not include periodic boundary condition in the confining z-direction. Permeability $P(\%)$ at the p-wall is obtained by numerically integrating the density profile under the peak close to z_P and efficiency, $e(\%) = 100 - P$.

We calculate stress tensor per particle for different time step from LAMMPS software package. Stress tensor is defined for ith particle as following: $S_{xy,i} =$

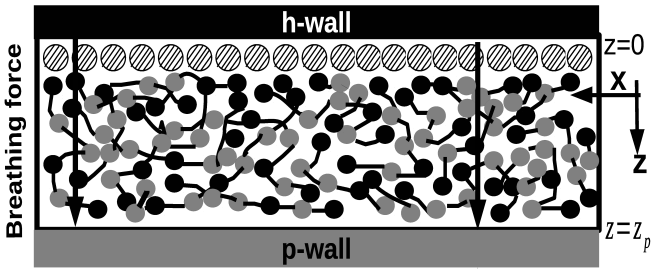

Figure 4.1: A model diagram of Polymeric network confined in asymmetric h(black) and p(grey) wall. Polymer consists of two beads: h-beads are shown in solid black circle and p-beads are shown in solid grey circle. h-beads prefer h-wall and p-beads prefer p-wall. Tracers particles (open black circle with hatch) are added close to h-wall. Tracers prefer p-beads and p-wall. Force on each tracer particle (mimic breathing) is added from h-wall to p-wall. Force are represented by black arrows from h-wall to p-wall. Force is maximum at $z = 0$ and zero at $z = z_P$. (The y-axis not shown is pointing into the page).

$-m_i V_{x,i} v_{y,i} - W_{xy,i}(i)$. m_i is the mass of the particles. $v_{x,i}$ is the velocity of x direction. The virial contribution of the i-th particle from all possible interactions, $W_{xy,i} = \frac{1}{2}\sum_{j=1}^{j=N_P}(r_{x,i}F_{y,i} + r_{x,j}F_{y,j}) + \frac{1}{2}\sum_{j=1}^{j=N_b}(r_{x,i}F_{y,i} + r_{x,j}F_{y,j})$. The first term is a pairwise energy contribution where j loops over the N_P neighbors of atom i, $r_{x,i}$ and $r_{x,j}$ are the x component of positions of the 2 atom pair i and j. $F_{y,i}$ and $F_{y,j}$ are the y component forces on the 2 atoms i and j resulting from the pairwise interaction. The second term is a bond contribution of similar form for the N_b bonds which atom i is part of. Bonded interactions over only for the network polymeric bead particles. The formula for total pressure P_{sys} of a system in three dimension is $P_{sys} = -\frac{1}{3V}\sum_i(S_{xx,i} + S_{yy,i} + S_{zz,i})$. V is the volume of the region. Summation is over all particles in the region. Pressure can also be calculated along a particular direction for a group of particles. Here we calculate pressure along confinement direction z, P_{zz} of network beads only. We sum (zz) component of the stress tensor of network beads belonging to a strip of width δz along confinement direction(z-direction) and divide the number by the volume of the strip. We take average over steady state configurations.

4.4 Results

We make an interpenetrating polymer network using the Langevin dynamics simulations as given in Eq. 4.6 between the asymmetric walls. An equilibrium snapshot of the interpenetrating polymer with h:p =50:50(25 p-beads and 25 h-beads), $k = 50$, and $z_P = 5.5$ is shown in Fig. 4.2(a). The $C(r)$ data in Fig. 4.2(b) shows a sharp first peak at r=1. This confirms that the monomers among

different polymeric chains stay close to each other which is signature of an interpenetrating network.

We insert TCPs above the h-wall via the GCMC at a chemical potential and temperature (see the Appendix A) corresponding to the packing fraction (0.47) in bulk liquid phase. We set $\bar{\epsilon} = 3.3$ while keeping the other parameters same as in the interpenetrating polymer. Fig. 4.2(c) shows the tracer density profile $\rho_{tr}(z)$. We observe distinct peaks along z direction, the strongest near h-wall. The peak near h-wall denotes particles stopped due to geometrical effect. We numerically integrate this peak N_h and divide by total number of TCPs N_{tot}. We plot $Q = 100(1 - \frac{N_h}{N_{tot}})$ with σ_{tr} in Fig. 4.2(c)(inset). This quantity goes to zero if no tracer can permeate into the network. The corresponding TCP diameter estimates the mean pore size of the network. The data shows that Q linearly falls with σ_{tr}. The linear extrapolation of this quantity to zero gives an estimate of mean pore size of the network(~ 2). Then we apply driving force along +z direction on TCPs.

4.4.1 Permeation of tracer colloidal particles in steady state condition

We show in Fig. 4.2(d) that change in P with time for $\sigma_{tr} = 1.5$ for different F_0. All curves saturate at large times that ensures the steady state. We define saturation time t_s from Fig. 4.2(d) when P reaches 50% of the saturation value. In Fig. 4.2(e) we show t_s (for $\sigma_{tr} = 1.5$) decreases with F_0 with a power law dependence with an exponent -0.36. The t_s increases linearly with σ_{tr} for $F_0 = 1.0$, shown in Fig. 4.2(f). Converting to physical units we find that for $\sigma_{tr} = 1.5$, $t_s \approx 0.6\,\mathrm{sec}$. This compares well to normal healthy human breathing time.

In order to understand the nature of permeation process, we explore the temperature dependence of P. We consider the saturated value of P for a given condition. The $\ln P$ versus $1/T^*$ plot for $\sigma_{tr} = 1.5$ and different F_0 in Fig. 4.3(a) show linear fall, suggesting an activated Arrhenius process.[54] The slope of the linear dependence gives the activation barrier F_B. We show similar data for $\sigma_{tr} = 1.2$ for $F_0 = 1.0$ in Fig. 4.3(a). Here the line is almost flat, denoting that the TCPs of this size experience almost no barrier. The barrier is sensitive to F_0 as well. We show in Fig. 4.3(b) that F_B varies linearly with F_0 for $\sigma_{tr} = 1.5$.

Next we consider the microscopic origin of F_B. We compute the potential energy profile along the z direction per tracer particle, averaged over steady state configurations. $V_H(z)$ is the potential energy profile for interaction of the TCPs with the h-beads, $V_P(z)$ that with p-beads and the total potential energy, $V(z) = V_H(z) + V_P(z)$. We show in Fig. 4.3(c) $V_H(z), V_P(z)$ and $V(z)$ versus z for

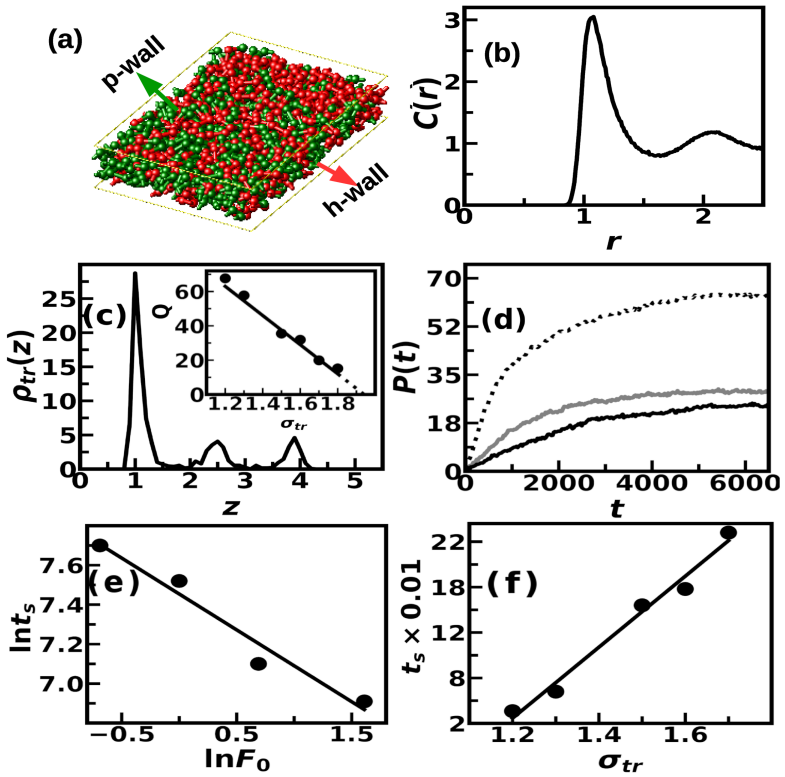

Figure 4.2: (a) A configuration of Polymeric network confined in asymmetric h and p wall. h-beads are shown in red and p-beads are shown in green. Here parameters are taken: $T^* = 1.0$, h:p=50:50, $\epsilon_{hh} = 1.0$, $\epsilon_{pp} = 0.33$, $\epsilon_{h,wh} = 1.0$, $\epsilon_{p,wh} = 0.033$, $\epsilon_{p,wp} = 0.33$, $\epsilon_{h,wp} = 0.033$, $k = 50$, $z_P = 5.5$. (b) Plot of inter-strand correlation function of beads belonging to two different polymeric strands $C(r)$ over r for $T^* = 1.0$, h:p-50:50(black) with $\epsilon_{hh} = 1.0$, $\epsilon_{pp} = 0.33$, $\epsilon_{h,wh} = 1.0$, $\epsilon_{p,wh} = 0.033$, $\epsilon_{p,wp} = 0.33$, $\epsilon_{h,wp} = 0.033$, $k = 50$, $z_P = 5.5$.(c) Tracer density profile $\rho_{tr}(z)$ versus z plot for $T^* = 1.0$, $\sigma_{tr} = 1.5$ with $F_0 = 0$, h:p=50:50, $\bar{\epsilon} = 3.3$, $k = 50$, $z_P = 5.5$. Inset: Q versus σ_{tr} plot with $T^* = 1.0$, $F_0 = 0$, h:p=50:50, $\bar{\epsilon} = 3.3$, $k = 50$, $z_P = 5.5$. The solid line is the best fit. (d) $P(t)$ versus t plot for $F_0 = 1$(black continuous line), $F_0 = 2$(grey continuous line), $F_0 = 5$(black dotted line). (e) t_s versus F_0 log-log plot with $\sigma_{tr} = 1.5$. The solid line slope -0.36 represents best fit. (f) t_s versus σ_{tr} plot (solid circles) with $F_0 = 1.0$. The solid line represents the best fit. The other parameters in panel (d)-(f) are the same as in (c).

$\sigma_{tr} = 1.2$ with $F_0 = 1.0$(main panel) and $\sigma_{tr} = 1.5$(inset). We find that both $V_H(z)$ and $V_P(z)$ are almost flat, but $V_P(z)$ is deeper than $V_H(z)$ and $V(z) \approx V_P(z)$. Thus, $V_P(z)$ is primarily responsible for the energy barrier. A larger TCP experiences more p-beads in course of its motion to experience a deeper energy landscape than smaller TCPs which we observe in Fig. 4.3(d) for $\sigma_{tr} = 1.5$ for the same F_0. The minima of $V_P(z)$ close to h-wall matches well with the F_B value for $\sigma_{tr} = 1.5$ for $F_0 = 1$ in Fig. 4.3(b).

We show various factors affecting $V_P(z)$:

(1) We plot $V_P(z)$ versus z for different $\bar{\epsilon}$ with $F_0 = 1.0$ and $\sigma_{tr} = 1.5$ in

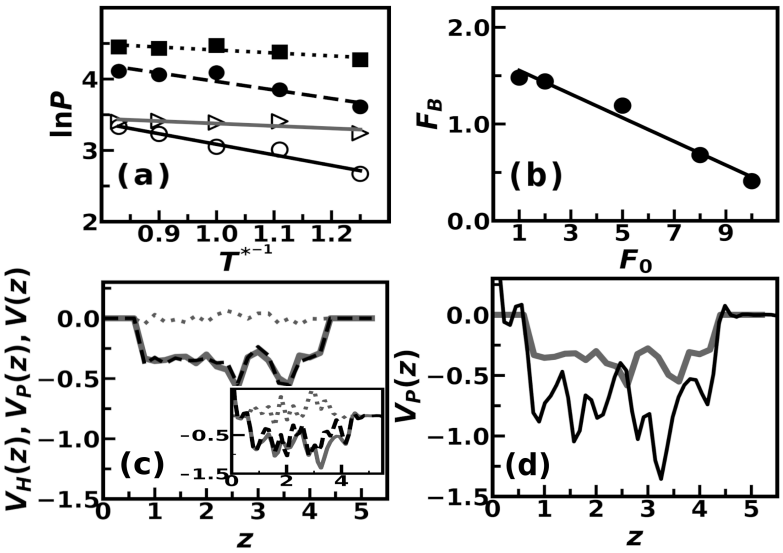

Figure 4.3: (a) $\ln P$ versus $\frac{1}{T^*}$ plot for $\sigma_{tr} = 1.5$ with h:p=50:50, $\bar{\epsilon} = 3.3$, $k = 50$, $z_P = 5.5$ for $F_0 = 1$(open circle), $F = 5$(close circle), $F = 10$(close square) and for $\sigma_{tr} = 1.2$ with $F_0 = 1$(open triangle). The best fitted lines are also shown. (b) F_B versus F_0 with h:p=50:50, $\bar{\epsilon} = 3.3$, $k = 50$, $z_P = 5.5$ $\sigma_{tr} = 1.5$(close circle) along with the fitted lines (c) Potential energy profile over z for $T^* = 1.0$, $\sigma_{tr} = 1.2$ with h:p=50:50, $\bar{\epsilon} = 3.3$, $k = 50$, $z_P = 5.5$, $F_0 = 1$: V_H(grey dotted line), $V_P(z)$ (grey continuous line), $V(z)$ (black dashed line). Inset: similar data for $\sigma_{tr} = 1.5$. (d) Potential Energy profile $V_P(z)$ for $\sigma_{tr} = 1.2$ (grey line) and $\sigma_{tr} = 1.5$(black line) with other parameter same as (c).

Fig. 4.4(a). We find the minimum of the energy of the profile gets deeper at $\bar{\epsilon} = 5$ than that at $\bar{\epsilon} = 3.3$. For even lower $\bar{\epsilon}(= 2.0)$, $V_P(z)$ is almost flat profile showing no barrier. The large tracer and p-bead interaction tends to localize the TCPs with the space of the network.

(2) The localization tendency is opposed by the driving force. The external force helps the TCPs to overcome the p-bead interaction energy. We illustrate the energy profile in presence of external drive in Fig. 4.4(b). We fix $\sigma_{tr} = 1.5$ and $\bar{\epsilon} = 3.3$ and vary F_0. A deeper minimum is observed in $V_P(z)$ close to the p-wall at a higher $F_0(= 10.0)$ compared to a lower $F_0(= 1.0)$. This shift helps the TCPs to move closer to the p-wall, increasing P.

(3) Tracer particle localization within the mask can also be achieved by changing the network rigidity k. We show energy profile $V_P(z)$ for two different k in Fig. 4.4(c). We observe minimum of profile gets deeper for higher $k(= 500)$ compared to lower $k(= 50)$, suggesting more localisation of particles inside the network.

(4) We also plot energy profile $V_P(z/z_P)$ versus z/z_P for two different confinement lengths keeping monomer density the same as in Fig. 4.4(d). We divide z with confinement length z_P to ensure the range (0,1) for both cases. We observe

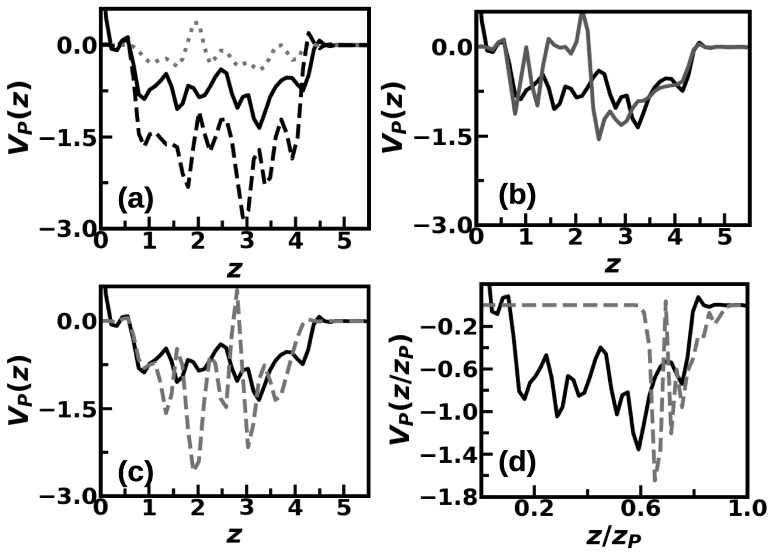

Figure 4.4: (a) $V_P(z)$ versus z plot with $T^* = 1.0$ for $k = 50$, $z_p = 5.5$, $F_0 = 1.0$ for $\bar{\epsilon} = 3.3$(black line); $\bar{\epsilon} = 2$ (grey dotted line) and $\bar{\epsilon} = 5$ (black dashed line). (b) $V_P(z)$ versus z plot with $T^* = 1.0$ for $\bar{\epsilon} = 3.3$, $k = 50$, $z_p = 5.5$ for $F_0 = 1.0$(black line); $F_0 = 10.0$(grey line). (c) $V_P(z)$ versus z plot of $\sigma_{tr} = 1.5$ with $T^* = 1.0$, h:p=50:50, $F_0 = 1$, $\bar{\epsilon} = 3.3$, $z_P = 5.5$ $k = 50$(black), $k = 500$(dotted grey). (d) $V_P(z/z_P)$ versus z/z_P plot of $\sigma_{tr} = 1.5$ with $k = 50$ for $z_P = 5.5$ (black), $z_P = 16.5$ (dotted grey). Other parameters are same as panel (a).

that for large $z_P(= 16.5)$, deeper minima are observed close to the p-wall with a relatively flat profile elsewhere compared to lower $z_P(= 5.5)$. So, particles easily pass through the network in less confined system.

4.4.2 Mask efficiency

Next we illustrate how the mask efficiency e can be tuned by the network properties. Mask efficiency is defined by $e(\%) = 100 - P(\%)$. Lower the value of P is, lower is the number of tracer particles penetrating into the region close to the p-wall, meaning better efficiency of the FM to intercept the TCPs. We fix the temperature at the room temperature $(T^* = 1.0)$, make sure of the breathability condition $(F_0 = 1.0)$ and consider the droplet size in the micrometer range $(\sigma_{tr} = 1.5)$. We observe changes in e varying $\bar{\epsilon}$ for different composition, namely, h:p ratio. We show e versus p plot for both low and large $\bar{\epsilon}$ in Fig. 4.5(a). For low $\bar{\epsilon}$ (=0.5) e decreases linearly with p. For larger $\bar{\epsilon}$ (=5.0) e higher than that with lower $\bar{\epsilon}$ for all h. Moreover, e has a maximum for this $\bar{\epsilon}$ at $p = 50\%$.

In order to understand the composition dependence, we note that there are competitive aspects. We show the first peak height of the inter-strand correlation function, C_{max} as a function of p in Fig. 4.5(b) which clearly shows a linear fall of

C_{max} with p. Note that increase in p means decrease in h. Since the h beads ensure the inter-strand connectivity in the network, the connectivity decreases with increasing p. This allows the TCPs to permeate through the network more easily. The fall in e for low $\bar{\epsilon}$ (=0.5) follows this trend particularly for large p. On the other hand, larger $\bar{\epsilon}$ creates a larger barrier to the TCP movement as observed in Fig. 4.4(a). These two opposing tendencies control the composition dependence of e. For larger $\bar{\epsilon}$ (=5.0), the competing effects results in the maximum at certain p value.

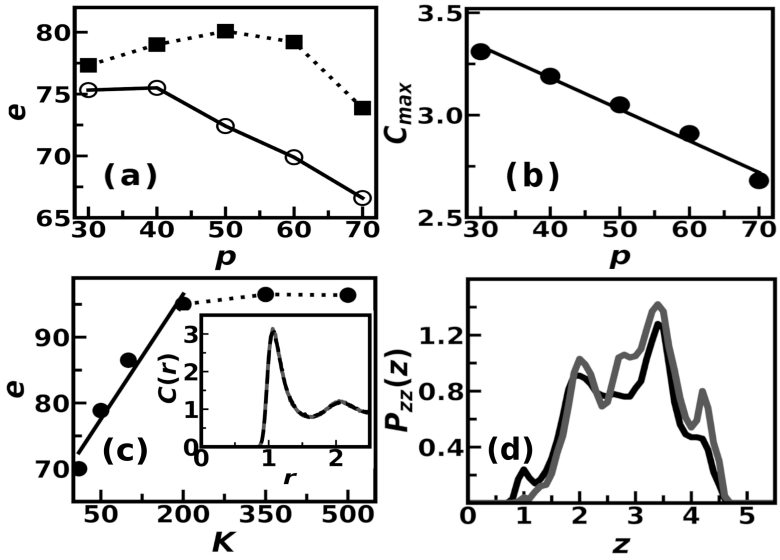

Figure 4.5: (a) e versus p plots of $\sigma_{tr} = 1.5$ with $T^* = 1.0$, $k = 50$,$z_P = 5.5$,$F_0 = 1$, for $\bar{\epsilon} = 0.5$(open circle). The black line is guide to the eyes; $\bar{\epsilon} = 5.0$(black square). The dotted line is guide to the eyes. (b) C_{max} versus p plots with $T^* = 1.0$, $\epsilon_{hh} = 1.0$, $\epsilon_{pp} = 0.33$, $\epsilon_{h,wh} = 1.0$, $\epsilon_{p,wh} = 0.033$, $\epsilon_{p,wp} = 0.33$, $\epsilon_{h,wp} = 0.033$, $k = 50$, $z_P = 5.5$. (c) e versus k plot (solid circles) for $\sigma_{tr} = 1.5$ with $T^* = 1.0$, h:p=50:50, $F_0 = 1$, $\bar{\epsilon} = 3.3$, $z_P = 5.5$. Solid line represents the best fit and dotted line is a guide to the eyes). Inset: pair correlation function of beads belonging to two different polymeric strands $C(r)$ versus r for $k = 50$(dotted black) and $k = 500$(grey). Other parameters are $T^* = 1.0$, h:p-50:50, $\epsilon_{hh} = 1.0$, $\epsilon_{pp} = 0.33$, $\epsilon_{h,wh} = 1.0$, $\epsilon_{p,wh} = 0.033$, $\epsilon_{p,wp} = 0.33$, $\epsilon_{h,wp} = 0.033$, $z_P = 5.5$. (d) $P_{zz}(z)$ versus z plots for $k = 50$(black) and $k = 500$(grey). Other parameters are as same as panel (c).

We also examine how the rigidity and confinement length z_P affect e. We plot e with k in Fig. 4.5(c). We observe linear increase in e with k and saturation for large k. Unlike the case of Fig. 4.5(b) there is no such significant change in the interpenetration property of the network for different rigidities as shown by $C(r)$ for different k values in the inset of Fig. 4.5(c). We further compute the normal (zz) component of the pressure tensor of the network beads as a function of z. The normal pressure profile $P_{zz}(z)$ in Fig. 4.5(d) shows peaks close to both walls. The peak of $P_{zz}(z)$ close to p-wall increases with rigidity.

Thus, the network resists more particles from passing through it towards p-wall with increasing k resulting in enhanced efficiency. This is consistent with deeper $V_P(z)$ in Fig. 4.4(c) observed for large k. In other words, a large k allows a better interaction of the network with the TCP.

In order to examine how the thickness of the network region affects e, we increase z_P keeping the monomer density fixed. We plot e with z_P in Fig. 4.6(a). We find as z_P increases as e decreases linearly and eventually gets saturation beyond $z_P = 16.5$. Inter-strand correlation function $C(r)$ for different confinement length is shown in Fig. 4.6(b). It shows the first peak height of $C(r)$ decreases with increasing z_P. The peak is lowest for the bulk limit. We describe the bulk case as an interpenetrating network without confinement. To prepare a bulk network, we remove the walls and use the periodic boundary condition in each direction. Fig. 4.6(c) shows that C_{max} linearly drops with z_P up to $z_P = 16.5$ after which the bulk limit sets in. Thus, the system gets less confined, the network structure gets loose. A loose network provides a flat $V_P(z)$, shown in Fig. 4.4(d), and better mobilities of the TCPs and hence, poorer e.

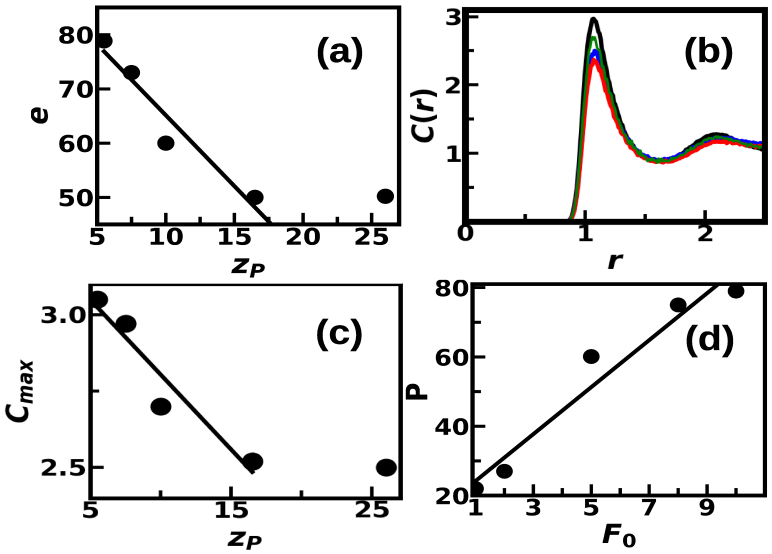

Figure 4.6: (a) e versus z_P plot (solid circles) for $T^* = 1.0$, $\sigma_{tr} = 1.5$ with $F_0 = 1$, h:p=50:50, $\bar{\epsilon} = 3.3$, $k = 50$. (b) Plot of $C(r)$ versus r for $z_P = 7.5$(black) , $z_P = 10.5$(green), $z_P = 26.0$ (blue), bulk(red) with $T^* = 1.0$, h:p=50:50, $k = 50$,$z_P = 5.5$. first peak of $C(r)$ decreases with increasing z_P and merge with bulk case. The other parameters for all case is $\epsilon_{hh} = 1.0$, $\epsilon_{pp} = 0.33$, $\epsilon_{h,wh} = 1.0$, $\epsilon_{p,wh} = 0.033$, $\epsilon_{p,wp} = 0.33$, $\epsilon_{h,wp} = 0.033$. (c) C_{max} versus z_P (solid circles). Parameters are $T^* = 1.0$, h:p-50:50, $\epsilon_{hh} = 1.0$, $\epsilon_{pp} = 0.33$, $\epsilon_{h,wh} = 1.0$, $\epsilon_{p,wh} = 0.033$, $\epsilon_{p,wp} = 0.33$, $\epsilon_{h,wp} = 0.033$, $k = 50$. (d) P versus F_0 plot(solid circles) for the reverse case with $T^* = 1.0$, h:p=50:50, $\bar{\epsilon} = 3.3$, $k = 200$, $z_P = 5.5$. Solid line represents the best fits.

So far we have calculated tracer permeation during inhalation cycle. Now

we consider exhalation with FM on. Using parameters for $e \sim 95\%$ ($\bar{\epsilon} = 3.3$, $F_0 = 1.0$, $T^* = 1.0$, $k = 200$, and $z_P = 5.5$) we put TCPs with $\sigma_{tr} = 1.5$ close to p-wall as done previously. We apply driving force from p-wall to h-wall. We find in Fig 4.6(d) that the P at h-wall increases linearly with F_0. Thus, TCPs are efficiently drained away.

Our results suggest that large efficiency can be achieved by a deeper $V_P(z)$ profile. For instance, >90% efficiency in intercepting tracer micro droplets under normal breath-ability condition at room temperature can be achieved under the following conditions: (1) Composition of h:p=50:50 so that the number of p-beads is sufficient in number to interact with the TCPs, keeping the network structure sufficiently robust. (2) $\bar{\epsilon} > 3$ to allow large interaction of the p-beads with the TCPs. (3) Fairly rigid network ($k \geq 200$); and (4) $z_P \sim$ few microns so that the network remains sufficiently strong to resist the TCP penetration.

4.4.3 Efficiency Diagram

We also calculate an efficiency diagram of $\sigma_{tr} = 1.5$ in plane $\bar{\epsilon}$ and h:p ratio of polymer chains(Fig. 4.7). We fix the other parameters $k = 200$, $z_P = 5.5$. We observe for every h:p ratio, a crossover from $e < 90\%$ to $e > 90\%$ occurs with increasing $\bar{\epsilon}$. The cross-over point is different for different h:p ratio. It is found that cross-over happens at large $\bar{\epsilon}$ for extreme points along h:p axis. The cross-over happens comparatively at small $\bar{\epsilon}$ around h:p=50:50. Efficiency diagram suggests possible composition of FM and relative interaction of tracer-p bead interaction to achieve efficiency of FM $e > 90\%$. It may be helpful in designing better FM.

4.5 Conclusions

To summarize, we study the permeation of TCPs within a network of polymers in presence of a driving force, using Langevin dynamics simulations. The parameters in our studies are chosen so as to ensure breath-ability conditions in an FM. We find that the droplet permeation through the network is an activated process. The activation barrier increases with (1) increasing tracer size, (2) decreasing driving force and (3) increasing network-tracer interactions. The barrier height is mainly determined by the magnitude of the more favourable interaction experienced by the TCP in the network. For a given tracer size, driving force and temperature, the efficiency of the mask depends on: (1) h:p ratio, (2) increasing interaction strength of tracer and p-beads, (3) increasing the rigidity

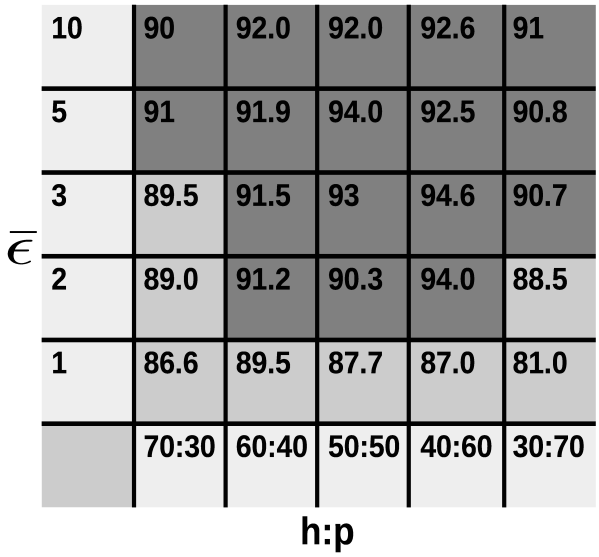

Figure 4.7: Efficiency diagram of e in $\bar{\epsilon}$ - h : p plane. Dark shaded region represent $e > 90\%$. Light shaded region represent $e < 90\%$.

and (4) decreasing the thickness of the network. Our model is sufficiently robust to be helpful in designing mask with better efficiency while retaining normal breath-ability conditions. We do not include the electrostatic interaction in our model. However, it may be interesting to take charge bead of FM network to observe long range electrostatic effect in efficiency of FM in future. It may be also worth to take into account the shape of size change of micro-droplets to observe more realistic transport inside FM in future.

Appendix

A. Insertion of tracer colloidal particles

We insert the tracer colloidal particles(TCPs) as per the following steps:

1) We calculate chemical potential of TCP corresponding to the packing fraction (0.47) in the bulk liquid phase in a cubic box. Chemical potential is calculated through Widom's test particle insertion method for different size of TCPs and different temperatures.

2) We generate TCP of a particular size σ_{tr} through Grand canonical Monte Carlo (GCMC) at a temperature T^* using measured chemical potential. We use box dimensions $L_x = 30$, $L_y = 20$ and $L_z = \sigma_{tr}$ to create a monolayer of TCPs. We use periodic boundary condition in x and y directions and allow particle motion in these directions. We perform GCMC using LAMMPS package. We run for 200000 steps for equilibration. GCMC is performed after each 10 steps with 100 average number of GCMC exchanges.

3) We place equilibrated polymer network and p-wall above the TCPs and the h-wall combination. The overlaps between network beads and TCP close to h-wall are removed through minimization algorithm in the LAMMPS and subsequently carry out the Langevin dynamics simulations.

σ_{tr}	η	T^*	μ
1.2	0.47	0.8	-3.39
1.2	0.47	0.9	-2.69
1.2	0.47	1.0	-1.94
1.2	0.47	1.1	-0.76
1.2	0.47	1.2	-0.23
1.5	0.47	0.8	-3.49
1.5	0.47	0.9	-3.07
1.5	0.47	1.0	-2.12
1.5	0.47	1.1	-1.51
1.5	0.47	1.2	-0.98
1.7	0.47	0.8	-4.31
1.7	0.47	0.9	-3.48
1.7	0.47	1.0	-2.7
1.7	0.47	1.1	-1.92
1.7	0.47	1.2	-1.43

Table 4.1: Chemical potential value for different σ_{tr} and temperature T^*.

Chapter 5 Reverse Osmosis of binary mixture through polymeric membrane

5.1 Introduction

In the previous chapter, we observe that tracer permeation can be controlled by changing different properties of polymeric network. Here we discuss another important case, namely, how reverse osmosis can be controlled. Osmosis is a physical process where a solvent flow across a semipermeable membrane from a region of lower to higher solute concentration[55] in the solution. It is the basis of the transport of ions across cell membranes, the regulation of blood salt levels by the kidneys, water uptake by plants, technologies for kidney dialysis[126] and many more. Reverse osmosis(RO) is a method where pressure is applied to overcome the natural osmotic pressure and enable solvent flow from higher to lower solution concentration in steady state conditions. RO technique is one of the most advanced ways to extract solvents from mixtures, widely used in industries like water treatment,[56,57] biofuels,[127] petrochemical,[128] and pharmaceuticals processes.[129] RO is important in industry and households for purification of water. Similarly, RO for separation of smaller molecular size solute from organic solvents have also developed in recent times.[61]

Thin Film Composite (TFC) is widely used as RO membrane prepared through interfacial polymerization(IP) process.[130] IP is a diffusion-controlled process where trimesoyl chloride in organic phase comes into contact with diamine in aqueous(polar) solvent. The reaction occurs only at the interface as the trimesoyl chloride can't diffuse into the aqueous phase.[59] As the polymerization process only occurs at the interface, the process is called interfacial polymerization. The prepared entangled polymer is attached to polysulfone support for the

mechanical strength of the TFC membrane. Typical thickness of polyamide layer is around $10 - 100$ nm.[131] Simulation studies[132] capture the IP process through coarse-grain model and reproduce experimental results.[133]

TFC RO Membrane can be thought of as polymer matrix.[59] The performance of membrane is directed by thickness, pore size distribution, roughness, hydrophilicity, chemical properties[59] etc. These properties can be tuned by various ways tuning membrane matrix during preparation for better performance. Experiment shows improving hydrophilicity by introducing different chemical improve water permeation and salt rejection.[134] Studies also suggest that tuning TFC membrane using nanoparticles[135] as additives for better permeability. Incorporation ions like copper Cu^{++}[60] in membrane matrix show better pesticide removal from water and also better antibacterial properties. Performance in permeation increases introducing polypyrrole layer in TFC membrane.[136] Nonpolar mixtures are also separated using hydrophobic rich TFC membrane.[61,137] Selective separation in both organic and polar solvents are recently developed using trianglamine macrocycle as a monomer for cross-linked membranes through IP process.[138]

Both osmosis and reverse osmosis are governed by transport properties of fluid through RO membrane. Permeation or solvent recovery (P) is estimated as how much solvent is transported from one side of membrane to other side due to applied pressure overcoming osmotic pressure. The goal is to increase permeation as much as possible. Different permeation of solvent is observed in different solutions.[139] The other important point is to reject solute out of the solution allowing only solvent to permeate through the membrane. It is given by rejection rate (R) of the membrane. Studies have been carried out using full atomistic simulation using non-equilibrium molecular dynamics(NEMD).[3,139] Free energy profiles of water and ions are also studied inside thin films using metadynamics to estimate barrier for permeation and rejection process.[140] Another important criteria of membrane is fouling (F). It is the measure of amount of solute accumulated inside the membrane during permeation. This degrades the future performance of membrane. Studies show anti-fouling properties by incorporation graphene oxide (GO) sheets in the polyamide layer.[141]

The microscopic understanding of importance of different factors which control permeation, rejection and fouling is yet far from understood. Here, we investigate these factors in a model study. Instead of fully atomistic simulation, we perform coarse-grained modelling to figure out the key components controlling the transport through the membrane. The model RO membrane(M) is prepared using several identical polymeric strands with two different types of beads of

nano meter size. One beads(h-beads) mutually interacts more strongly compared to the other class of beads(p-bead). The h-beads mimic the hydrophobic species while the p-beads mimic the hydrophilic species. The network is under asymmetric confinement, consisting of walls, each of which is having favourable interaction with a given type of bead. This mimics interface where the membrane is stabilized. After preparing RO membrane as a polymeric network we remove wall on two sides and attach two reservoirs containing Lennard Jones(LJ) solvent particles on two sides to solvate the membrane along z and the z-motion of the membrane beads set to zero to mimic the rigid support. A schematic of the model is shown in Fig. 5.1. Next we replace the left reservoir(LR)($z = 0$ to $z = z_A$) with binary mixture of LJ particles where a few solute particles are added and the same number solvent particles are removed so that the number density of particles in both the reservoirs remain the same. The solute particles are larger than the solvent particles but smaller than the mean pore size so that transport through the membrane is possible for both but more favourable for the solvent. The right reservoir(RR)($z = z_B$ to $z = z_C$) remains the same as that during solvation. Two reflecting walls are attached in two extreme end of the reservoirs along z-direction. The partial volume fraction of solvent at the LR is lower than right reservoir which creates an osmotic pressure from right to left. Now we add external force $F(z)$ from left to right along z to overcome the osmotic pressure and observe the motion of both solvent and solute. Force is taken maximum at $z = 0$ and falls linearly to zero at $z = z_A$.

We study the system using molecular dynamics simulation. Our aim is to reduce the transport of solute particles across the membrane as much as possible without impeding the solvent motion by tuning different interactions in the system. The forces are due to interaction and external drive only on the solvents and the solutes in LR. The temperature of the system is maintained using Nose-Hover thermostat. The volume fraction of polymeric beads($\sim 25\%$) is as low as solvents($\sim 23\%$). The solutes volume fraction is low as well($\sim 0.04\%$). The increase in solvent density in steady state in RR with respect to the initial solvent density is measured as solvent recovery P. We also observe change in solute density in right reservoir with respect to the initial solute density at left reservoir, denoted as rejection rate R. Finally, we measure fouling of RO membrane F, as the volume fraction of solute stuck inside the RO membrane at steady state.

We fix size ratio of solute and solvent, driving force, ambient temperature and vary the relative interactions. We take different energy parameters in LJ potential: the bead bead interaction ($\epsilon_{\alpha,\beta}$), bead wall interaction ($\epsilon_{\alpha,wh}$ and $\epsilon_{\alpha,wp}$),

solvent-solvent interaction ($\epsilon_{S,S}$), solute-solute interaction ($\epsilon_{L,L}$), solvent-solute interaction ($\epsilon_{S,L}$), solvent-bead interaction ($\epsilon_{S,\alpha}$), solute-bead interaction ($\epsilon_{L,\alpha}$). We define relative interaction of solute with h,p beads $\bar{\epsilon}_L = \frac{\epsilon_{L,h}}{\epsilon_{L,p}}$, relative interaction of solvent with h,p beads $\bar{\epsilon}_S = \frac{\epsilon_{S,h}}{\epsilon_{S,p}}$ and vary $\bar{\epsilon}_L, \bar{\epsilon}_S$. We find that with increasing $\bar{\epsilon}_L$, rejection rate R and solvent recovery P improves but the fouling F also increases. To reduce F while maintaining R and P, we need to increase $\bar{\epsilon}_S$ sufficiently.

5.2 Model potential and simulation details

The RO membrane consists of several identical polymeric strands. Each polymeric strand is composed of two kinds of beads of the same diameter σ and mass m in a given h:p=(50:50) ratio, randomly distributed over the strand. The non-bonded interaction between two monomers i and j with separation r_{ij} is taken through the LJ 12-6 potential:

$$V_{\alpha,\beta}(r_{ij}) = \begin{cases} 4\epsilon_{\alpha,\beta}[(\frac{\sigma}{r_{ij}})^{12} - (\frac{\sigma}{r_{ij}})^{6}], & \text{if } r_{ij} < 2.5\sigma \\ 0, & \text{otherwise} \end{cases}$$

Here $\alpha(= h, p)$ and $\beta(= h, p)$ stand for the bead types and r_{ij} is separation between two beads. $\epsilon_{h,h}$ is the interaction between h-h beads. $\epsilon_{p,p}$ is the interaction between p-p beads. $\epsilon_{h,p}$ is taken through Berthelot rule. σ is different for all different species. The bonded interaction corresponding to stretching between two neighbouring beads at separation r_{ij}:

$$V_{bond}(r_{ij}) = \frac{1}{2}k_b(r_{ij} - r_0)^2 \tag{5.1}$$

where $r_0 = 1.5\sigma$ is the equilibrium distance between monomers and k_b the force constant. The change in bond angle also costs energy given by:

$$V_{angle}(\theta) = \frac{1}{2}k_\theta(\theta - \theta_0)^2 \tag{5.2}$$

where k_θ the force constant and $\theta = \cos^{-1}(\frac{\vec{r}_{ij}\cdot\vec{r}_{jk}}{|\vec{r}_{ij}||\vec{r}_{jk}|})$ is the angle produced by three consecutive monomers i,j,k and θ_0 is equilibrium angle, set to 114 degrees.[124] We consider a rigid network where the elastic deformation of any kind costs a lot of energy and ignore the distinction between these two elastic constants. Thus, we take $k_b = k_\theta = k = 100$ to reduce the number of variables.

The h-wall interacts with a bead via the LJ 9-3 potential:

$$V_{\alpha,wh}(z_i) = \epsilon_{\alpha,wh}[\frac{2}{15}(\frac{\sigma}{z_i})^9 - (\frac{\sigma}{z_i})^3] \tag{5.3}$$

Similarly, p-wall interacts with a bead :

$$V_{\alpha,wp}(z_i) = \epsilon_{\alpha,wp}[\frac{2}{15}(\frac{\sigma}{z_P - z_i})^9 - (\frac{\sigma}{z_P - z_i})^3] \tag{5.4}$$

Here $\alpha = (h, p)$ stands for the bead type and z_i is the z-coordinate of i-th particle. The σ values for all the interactions are taken to be the same but $\epsilon_{h,wh} > \epsilon_{p,wh}$ and $\epsilon_{p,wp} > \epsilon_{h,wp}$.

The solvent particles S interact with each other with strength $\epsilon_{S,S}$. $\epsilon_{S,h}$ and $\epsilon_{S,p}$ are interactions of S with h and p beads respectively. The solute L particles interact with each other with strength $\epsilon_{L,L}$. $\epsilon_{L,h}$ and $\epsilon_{L,p}$ are interactions of L with h and p beads respectively. $\epsilon_{S,L}$ follows Berthelot rule. We further take external force over S and L in LR as $F(z) = F_0(1 - z/z_A)$.

We take $\epsilon_{h,h}$ as unit of energy. The unit of length is diameter of S particles $\sigma_S = 0.5$ nm. The unit of mass is the mass of water of density 1 gm/cm^3 in a sphere of diameter 0.5 nm. The polymeric bead diameter is taken ($\sigma_b = 2\sigma_S$ =1 nm). The solute particle diameter is taken $\sigma_L = 1.8\sigma_S$. The diameters of all different particles are given in Table 5.1. The other energy interaction parameters are given in Table 5.2. For cross interaction diameters follow Berthelot rule. When preparing RO membrane, we use interaction of the wall with h and p-beads. For these choices of bead-bead interaction parameters, the polymeric network is uniformly spread throughout the gap between two walls. The unit mass is taken to be that for water droplet of diameter 0.5 nm. The masses of all different particles are given in Table 5.3. We vary: $\bar{\epsilon}_S = \epsilon_{S,h}/\epsilon_{S,p}$ and $\bar{\epsilon}_L = \epsilon_{L,h}/\epsilon_{L,p}$ at reduced temperature $T^* = \frac{k_B T}{\epsilon_{h,h}} = 1$.

Diameter of different particles	dimensionless value
σ_S	1.0
σ_L	1.8
σ_h	2.0
σ_p	2.0

Table 5.1: Diameter of particles

We perform simulation using the LAMMPS package[125] using Nose-Hover thermostat. Using the values of mass m, σ_S and ϵ_{hh}, we estimate a time scale,

Nature of interaction	dimensionless variable	dimensionless value
h,h	$\epsilon_{h,h}$	1.0
p,p	$\epsilon_{p,p}$	0.33
h,wh	$\epsilon_{h,wh}$	1.0
p,wh	$\epsilon_{p,wh}$	0.033
p,wp	$\epsilon_{p,wp}$	0.33
h,wp	$\epsilon_{h,wp}$	0.033
S,S	$\epsilon_{S,S}$	1.0
L,L	$\epsilon_{L,L}$	1.0

Table 5.2: Table for ϵ

Mass of different particles	dimensionless value
m_S	1.0
m_L	5.832
m_h	8.0
m_p	8.0

Table 5.3: Mass of particles

$\tau(=\sqrt{\frac{m\sigma_S^2}{\epsilon_{hh}}}) \sim 11$ picoseconds. The time step for integration is taken 0.001τ. All the quantities are averaged over three different independent trajectories each 600000τ long. We take $L_x = 30$ and $L_y = 20$, in x- and y- directions respectively with the periodic boundary conditions (PBC) and no PBC in z-direction.

First, we generate the interpenetrating polymer in an asymmetric pair of walls. We create RO membrane(M) using equilibrated interpenetrating polymer network confined by h and p-wall at first mimicking interfacial polymerization process in experimental thin film membrane preparation. The network consists of 9 identical polymeric strands, each having randomly distributed 50 monomers in a number ratio h:p=(50:50). Packing fraction of total polymeric beads in our model $\eta_b^M = \frac{\pi}{6}\frac{N}{V}\sigma_b^3 = 0.26$. For different parameter values we solvate the membrane, removing the wall. Here we restrict the polymeric beads motion along z-direction but allow them to move in x-y plane. We attach two reservoir (LR and RR) on both side of the RO membrane consists of solvent(S) particles to solvate the membrane with S particles without any external force. The z-distance of both reservoir $z_{LR} = z_{RR} = 20$. Two reflecting walls are placed at two extreme ends of two reservoirs. Next we add $N_L^{LR}(= 400)$ L particles in

the LR removing 400 S particles randomly from the LR so that total number density of particles (S+L) remain same in the box as RR. The partial volume fraction at LR, $\eta^{LR}_{S,int} = 0.26$ and $\eta^{LR}_{L,int} = 0.1$. The partial volume fraction at RR $\eta^{RR}_{S,int} = 0.27$ and $\eta^{RR}_{L,int} = 0.0$. The partial volume fraction at RR $\eta^{M}_{S,int} = 0.12$ and $\eta^{M}_{L,int} = 0.0$. The partial volume fraction of S is lower in LR compared to RR. Then we apply force to overcome osmotic pressure. We use $F_0 = 1$, which corresponds to $0.05\ kJ/mol/$Å in physical unit.

We calculate change in packing fraction of S particles $\eta^{\alpha}_{S}(t)$ with time, where α = LR, RR, M corresponds to the Left reservoir, right reservoir and inside membrane respectively. $\eta^{\alpha}_{S}(t) = \frac{\pi}{6}\rho^{\alpha}_{S}(t)\sigma^{3}_{S}$, here $\rho^{\alpha}_{S}(t)$ is number density of S at time t in $\alpha - th$ region. Similarly, we calculate packing fraction of L particles $\eta^{\alpha}_{L}(t)$ with time in $\alpha - th$ region. $\eta^{\alpha}_{L}(t) = \frac{\pi}{6}\rho^{\alpha}_{L}(t)\sigma^{3}_{L}$, here $\rho^{\alpha}_{L}(t)$ is number density of L at time t in $\alpha - th$ region. At large time in steady state we measure packing fraction of S at RR $\eta^{RR}_{S,steady}$, packing fraction of L at RR $\eta^{RR}_{L,steady}$ and packing fraction of L inside M $\eta^{M}_{L,steady}$. We define solvent permeation or recovery $P = 100(\frac{\eta^{RR}_{S,steady} - \eta^{RR}_{S,int}}{\eta^{RR}_{S,int}})$. Solute rejection rate R is defined as $R = 100(1 - \frac{\eta^{RR}_{L,steady}}{\eta^{LR}_{L,int}})$. We also define $F = 100\eta^{M}_{L,steady}$.

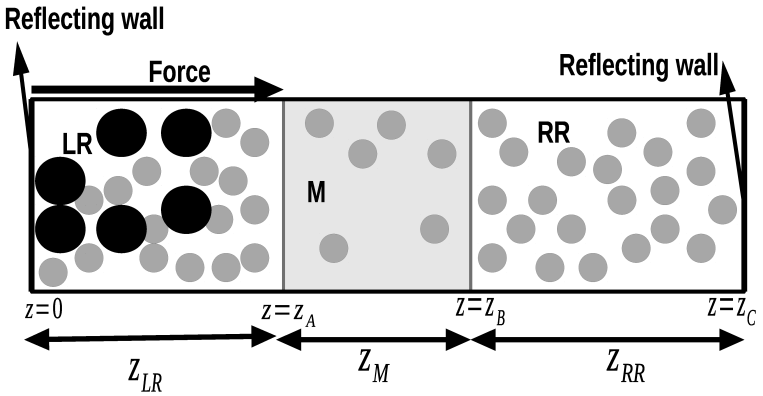

Figure 5.1: (a) Schematic diagram of RO process. M is the RO membrane in the middle solvated with S(grey) particles. LR is left reservoir containing S(grey) and L(black) particles. RR is the right reservoir containing S particles only initially. Two reflecting wall is attached in two extreme ends. Force is given in LR.

5.3 Results

At first we prepare the RO membrane. We show inter-strand correlation function $C(r)$ as Chapter 4 to ensure chains are linked to each other. The C(r) data in Fig. 5.2(a) shows a sharp first peak at $r = 2$(corresponding to bead diameter

σ_b which is two times larger than the unit of length σ_S). This confirms that the monomers among different polymeric chains stay close to each other which is a signature of an interpenetrating network. We show in the previous chapter that the mean pore size of the membrane is $\sim 4\sigma_S$(Chapter 4). Then we solvate the RO membrane attaching two reservoir without applying force. We plot packing fraction of S $\eta_S^{LR}(t), \eta_S^{RR}(t)$ with time in Fig. 5.2(b). After equilibration Membrane becomes solvated with S particles where($\eta_S^{LR} = \eta_S^{RR} = 0.27$, $\eta_S^{M} = 0.12$). Then,

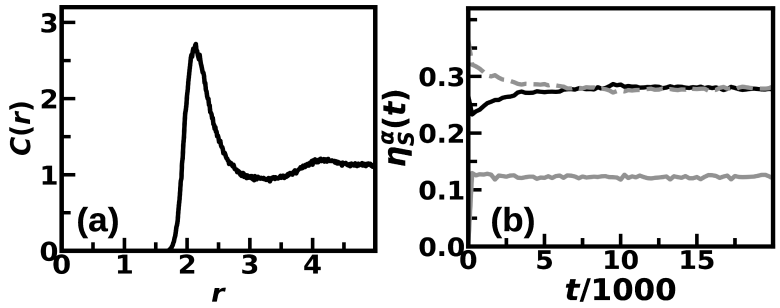

Figure 5.2: (a) Plot of inter-strand correlation function of beads belonging to two different polymeric strands $C(r)$ over r. (b) Packing fraction $\eta_S^{\alpha}(t)$ over time during solvation without applying force with $\bar{\epsilon}_S = 1.74$. $\alpha =$ RR(grey dotted line), LR(black line) and M(grey line).

we add 400 L particles in LR removing same number of S to maintain same number density in LR and RR. Here $\alpha_L = 1.8\sigma_S$ so that both L and S particles can permeate through the membrane but it is more favourable for S to permeate through. The initial packing fraction of S,L in each of the box LR, M, RR before addition of force : $\eta_{S,int}^{LR} = 0.26$, $\eta_{L,int}^{LR} = 0.1$, $\eta_{S,int}^{M} = 0.12$, $\eta_{L,int}^{M} = 0.0$, $\eta_{S,int}^{RR} = 0.27$, $\eta_{L,int}^{RR} = 0.0$. The partial volume fraction of S becomes lower in LR compared to RR. We model two types of solution (1) solutions of particles favouring h beads and (2) solutions of particles favouring p beads.

5.3.1 Case of solutions of particles favouring h beads

We apply force, $F_0 = 1$. We fix $\bar{\epsilon}_S = 1.74$ and $\bar{\epsilon}_L = 3.48$. Fig. 5.3(a-c) ensures that the system reaches at steady state in all LR, M, RR for both S and L particles at large time. We observe in Fig. 5.3(a) that the $\eta_S^{LR}(t)$ decreases in LR with time from initial packing $\eta_{S,int}^{LR}$ till they saturate in steady state. We also observe $\eta_L^{LR}(t)$ decreases then saturates. In Fig. 5.3(b) $\eta_S^{M}(t)$ increases in steady state from initial value. $\eta_L^{M}(t)$ also slightly increases inside M(Fig. 5.3(b)). In Fig. 5.3(c) we observe the steady state packing fraction of S in RR ($\eta_{S,steady}^{RR}$) is larger than the initial value in RR. However, the steady state packing fraction of L $\eta_{L,steady}^{RR}$

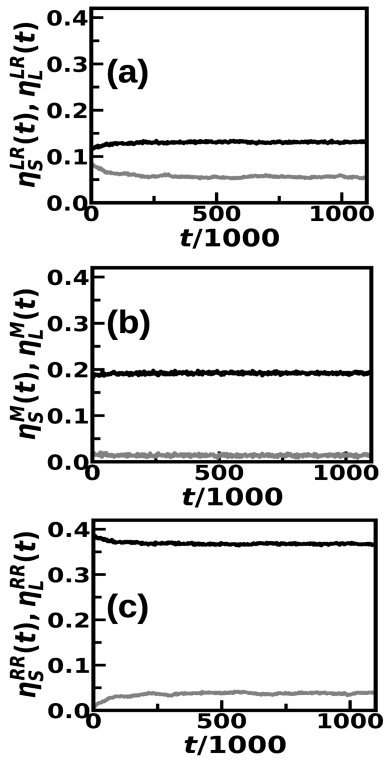

Figure 5.3: (a) Packing fraction $\eta_S^{LR}(t)$(black line), $\eta_L^{LR}(t)$(grey line) over time with applying force $F_0 = 1$. The parameters are $\bar{\epsilon}_S = 1.74$, $\bar{\epsilon}_L = 3.48$. (b) Packing fraction $\eta_S^M(t)$(black line), $\eta_L^M(t)$(grey line) over time. (c) Plot for $\eta_S^{RR}(t)$(black line), $\eta_L^{RR}(t)$(grey line) over time. The other parameters in panel (b-c) are same as panel (a).

Box	Steady state packing fraction
LR	$\eta_{S,steady}^{LR} = 0.13$, $\eta_{L,steady}^{LR} = 0.05$
M	$\eta_{S,steady}^{M} = 0.19$, $\eta_{L,steady}^{M} = 0.02$
RR	$\eta_{S,steady}^{RR} = 0.36$, $\eta_{L,steady}^{RR} = 0.05$

Table 5.4: Steady state packing fraction of S,L in different region

increases as well in RR. So, the force helps both S and L to permeate from LR to RR. We tabulate steady state values in each box LR, M, RR in Table. 5.4. We find for this case $R = 62.46\%$, $P = 32\%$, $F = 2\%$.

Now our aim is to increase R and P as high as possible while maintaining F as low as possible. We increase $\bar{\epsilon}_L = \frac{\epsilon_{L,h}}{\epsilon_{L,p}}$ and fix $\bar{\epsilon}_S = 1.74$. Here we restrict to $\bar{\epsilon}_L > 1$ as we increase $\epsilon_{L,h}$. We observe R increases with increasing $\bar{\epsilon}_L$ in Fig. 5.4(a). We observe from inset of Fig. 5.4(a) that R increases with $\bar{\epsilon}_L$ in power law with exponent 0.4 and finally comes to saturation for large $\bar{\epsilon}_L$. The physical

reason behind the observation is the following: as $\bar{\epsilon}_L$ gets larger, L particles are favourable to stay inside M. This reduces the number of L inside RR which reflects in higher R. In Fig. 5.4(b) we observe P increases with increasing $\bar{\epsilon}_L$. We observe from inset of Fig. 5.4(b) that increasing nature of P with $\bar{\epsilon}_L$ follows power law with exponent 0.23. We observe from Fig. 5.4(c) that F also increases rapidly with $\bar{\epsilon}_L$. In inset of Fig. 5.4(c) we observe the dependence of F with $\bar{\epsilon}_L$ in logarithmic plot with exponent 1.82.

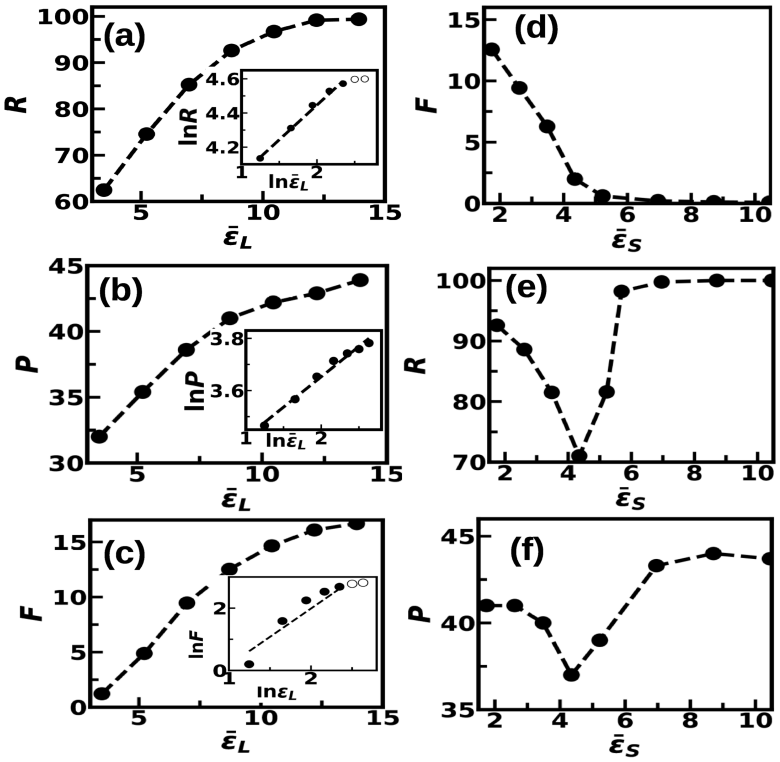

Figure 5.4: (a)R vs $\bar{\epsilon}_L$ plot with $\bar{\epsilon}_S = 1.74$. Black circles are points and the dotted line is guide to the eyes. Inset: $\ln R$ vs $\ln \bar{\epsilon}_L$ plot with $\bar{\epsilon}_S = 1.74$. Black close circles denote the increasing portion and open circles are saturated regions. The dashed line is the fitted line. (b) P vs $\bar{\epsilon}_L$ with $\bar{\epsilon}_S = 1.74$. Black circles are points and the dotted line is guide to the eyes. Inste: $\ln P$ over $\ln \bar{\epsilon}_L$ plot with $\bar{\epsilon}_S = 1.74$. Black close circles denote the increasing portion. The dashed line is the fitted line. (c) F vs $\bar{\epsilon}_L$ with $\bar{\epsilon}_S = 1.74$. Black circles are points and the dotted line is guide to the eyes. Inset: $\ln F$ vs $\ln \bar{\epsilon}_L$ plot with $\bar{\epsilon}_S = 1.74$. Black close circles denote the increasing portion and open circles are saturated regions. The dashed line is the fitted line. (d) F vs $\bar{\epsilon}_S$ plot with $\bar{\epsilon}_L = 8.71$. The black circles are points and the dashed line is guide to the eyes. (e) R vs $\bar{\epsilon}_S$ plot with $\bar{\epsilon}_L = 8.71$. The black circles are points and the dashed line is guide to the eyes. (f) P vs $\bar{\epsilon}_S$ plot with $\bar{\epsilon}_L = 8.71$. The black circles are points and the dashed line is guide to the eyes.

Now our aim is to decrease fouling keeping recovery and rejection at large level. We choose $\bar{\epsilon}_L = 8.71$ from Fig 5.4(a-c), where $R \sim 90\%$, $P \sim 40\%$ and $F = 13\%$. Now we increase $\bar{\epsilon}_S$ by increasing $\epsilon_{S,h}$. Here also we restrict to

$\bar{\epsilon}_S > 1$ as we increase $\epsilon_{S,h}$. In Fig. 5.4(d) we plot F with increasing $\bar{\epsilon}_S$. We observe F sharply decreases close to zero with increasing $\bar{\epsilon}_S$, beyond $\bar{\epsilon}_S > 4$. We observe in Fig. 5.4(e) and Fig. 5.4(f) there are minima in both R and P respectively. The minima is around $\bar{\epsilon}_S = 4$ for R and P. Rejection rate reaches 100% rejection rate for very large $\bar{\epsilon}_S \geq \bar{\epsilon}_L$. The physical reason behind the observed nature is following: For sufficiently large $\bar{\epsilon}_S$ the membrane is highly solvated. It resists L particles from coming from LR to M and subsequently to RR. Thus, we observe that both $\bar{\epsilon}_L$ and $\bar{\epsilon}_S$ need to be large and $\bar{\epsilon}_S \geq \bar{\epsilon}_L$ which mean $\epsilon_{S,h}\epsilon_{L,p} \geq \epsilon_{S,p}\epsilon_{L,h}$ for efficient performance.

5.3.2 Case of solutions of particles favouring p beads

In such cases $\bar{\epsilon}_S, \bar{\epsilon}_L < 1$ so that we describe data in terms of $\bar{\epsilon}_L^{-1}$ and $\bar{\epsilon}_S^{-1}$. Here we fix $\bar{\epsilon}_S = 0.57$ and vary $\bar{\epsilon}_L$. We observe in Fig. 5.5(a) R increases with increasing $\bar{\epsilon}_L^{-1}$. In inset of Fig. 5.5(a) we observe R increases with $\bar{\epsilon}_L^{-1}$ in power law fashion with exponent 0.34. In Fig. 5.5(b) we observe P increases with increasing $\bar{\epsilon}_L^{-1}$. In inset of Fig. 5.5(b) we observe power law increase of P with $\bar{\epsilon}_L^{-1}$ with exponent 0.21. Simultaneously F increases with increasing $\bar{\epsilon}_L^{-1}$ (Fig. 5.5(c)). In inset of Fig. 5.5(c) we observe increase of F is in power-law nature with exponent 1.79. We choose $\bar{\epsilon}_L = 0.114$, where $R \sim 90\%$, $P \sim 42\%$ and $F = 13\%$. Now, we vary $\bar{\epsilon}_S$ in the regime $\bar{\epsilon}_S < 1$. We observe in Fig. 5.5(d) that F decreases with increasing $\bar{\epsilon}_S^{-1}$. We observe in Fig. 5.5(e) and Fig. 5.5(f) there are minima in both R and P respectively. The minima is around $\bar{\epsilon}_S = 0.2$ for both cases. Rejection rate reaches 100% rejection rate for lower value of $\bar{\epsilon}_S \leq \bar{\epsilon}_L$ or $\epsilon_{S,h}\epsilon_{L,p} \leq \epsilon_{S,p}\epsilon_{L,h}$.

5.4 Conclusion

Since h-beads interact more strongly than the p-beads, the h-beads can be thought of as hydrophobic/nonpolar species and p-beads as polar species. It may be interesting to point out the implication of our model for realistic systems. Here solution consisting of S and L particles both preferring the h-beads can be thought of the case as a nonpolar solution. Our model calculation shows that the interaction of the nonpolar/hydrophobic moieties of the membrane should be strongly interacting with the solvent and solute particles, while the interaction with the nonpolar solvent needs to be at least as strong as that of nonpolar solute satisfying the inequality $\epsilon_{S,h}\epsilon_{L,p} \geq \epsilon_{S,p}\epsilon_{L,h}$. This could be a guiding principle to choose appropriate material for the RO membrane given the solution over which

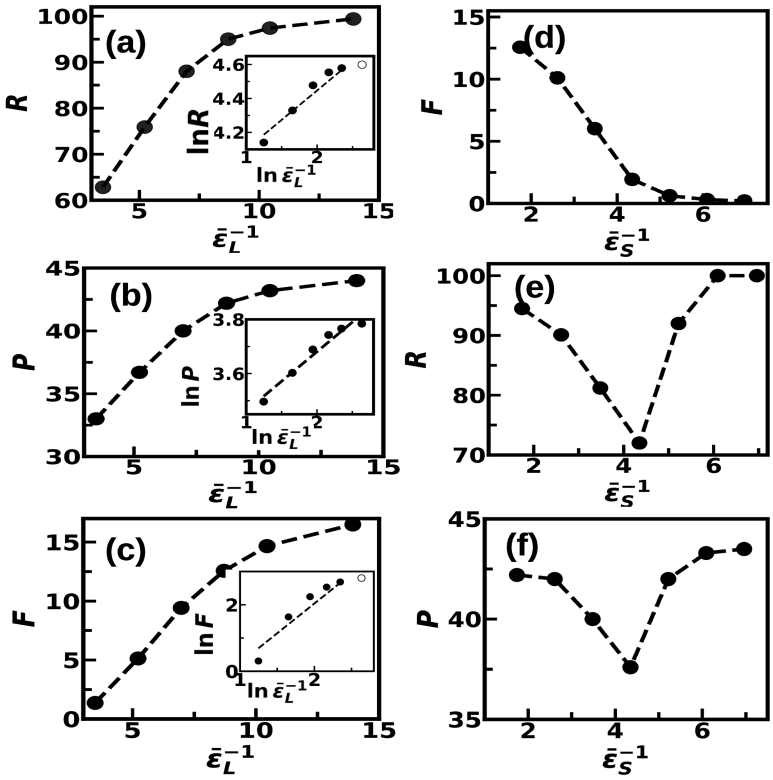

Figure 5.5: (a) R vs $\bar{\epsilon}_L^{-1}$ with $\bar{\epsilon}_S = 0.57$. Black circles are points and the dotted line is guide to the eyes. Inset: $\ln R$ vs $\ln \bar{\epsilon}_L^{-1}$ plot with $\bar{\epsilon}_S = 0.57$. Black close circles denote the increasing portion and open circles are saturated regions. The dashed line is the fitted line. (b) P vs $\bar{\epsilon}_L^{-1}$ with $\bar{\epsilon}_S = 0.57$. Black circles are points and the dotted line is guide to the eyes. Inset: $\ln P$ over $\ln \bar{\epsilon}_L^{-1}$ plot with $\bar{\epsilon}_S = 0.57$. Black close circles denote the increasing portion. The dashed line is the fitted line. (c) F vs $\bar{\epsilon}_L^{-1}$ with $\bar{\epsilon}_S = 0.57$. Black circles are points and the dotted line is guide to the eyes. Inset: $\ln F$ vs $\ln \bar{\epsilon}_L^{-1}$ plot with $\bar{\epsilon}_S = 0.57$. Black close circles denote the increasing portion and open circles are saturated regions. The dashed line is the fitted line. (d) F vs $\bar{\epsilon}_S^{-1}$ plot with $\bar{\epsilon}_L = 0.114$. The black circles are points and the dashed line is guide to the eyes. (e) R vs $\bar{\epsilon}_S^{-1}$ plot with $\bar{\epsilon}_L = 0.114$. The black circles are points and the dashed line is guide to the eyes. (f) P vs $\bar{\epsilon}_S^{-1}$ plot with $\bar{\epsilon}_L = 0.114$. The black circles are points and the dashed line is guide to the eyes.

the RO operation needs to be performed. On the other hand, solution consisting of S and L particles both preferring the p-beads can be thought of the case as a polar solution. The model shows that interaction of polar/hydrophilic moieties of the membrane should be strongly interacting with solution components. Similarly, interaction with polar solvent needs to be of similar strength as that of polar solute satisfying the inequality $\epsilon_{S,h}\epsilon_{L,p} \leq \epsilon_{S,p}\epsilon_{L,h}$. We arrive at optimal conditions for different interaction to achieve maximal RO operation.

Bibliography

[1] Hartmut Löwen. Colloidal soft matter under external control. *Journal of Physics: Condensed Matter*, 13(24):R415, 2001.

[2] Suman Dutta and J Chakrabarti. Length-scales of dynamic heterogeneity in a driven binary colloid. *Physical Chemistry Chemical Physics*, 22(31):17731–17737, 2020.

[3] Meng Shen, Sinan Keten, and Richard M Lueptow. Dynamics of water and solute transport in polymeric reverse osmosis membranes via molecular dynamics simulations. *Journal of Membrane Science*, 506:95–108, 2016.

[4] Xiankun Lin, Tieyan Si, Zhiguang Wu, and Qiang He. Self-thermophoretic motion of controlled assembled micro-/nanomotors. *Phys. Chem. Chem. Phys.*, 19:23606–23613, 2017.

[5] Zhiguang Wu, Xiankun Lin, Yingjie Wu, Tieyan Si, Jianmin Sun, and Qiang He. Near-infrared light-triggered "on/off" motion of polymer multilayer rockets. *ACS Nano*, 8(6):6097–6105, 2014. PMID: 24806430.

[6] R Di Leonardo, F Ianni, and G Ruocco. Colloidal attraction induced by a temperature gradient. *Langmuir*, 25(8):4247–4250, 2009.

[7] Stefan Duhr and Dieter Braun. Two-dimensional colloidal crystals formed by thermophoresis and convection. *Applied physics letters*, 86(13):131921, 2005.

[8] Yu Abe, Bo Zhang, Leonardo Gordillo, Alireza Mohammad Karim, Lorraine F Francis, and Xiang Cheng. Dynamic self-assembly of charged colloidal strings and walls in simple fluid flows. *Soft matter*, 13(8):1681–1692, 2017.

[9] Zhihua Lin, Changyong Gao, Meiling Chen, Xiankun Lin, and Qiang He. Collective motion and dynamic self-assembly of colloid motors. *Current opinion in colloid & interface science*, 35:51–58, 2018.

[10] Dhruv P Singh, Udit Choudhury, Peer Fischer, and Andrew G Mark. Non-equilibrium assembly of light-activated colloidal mixtures. *Advanced Materials*, 29(32):1701328, 2017.

[11] S Siva Nasarayya Chari, Chandan Dasgupta, and Prabal K Maiti. Scalar activity induced phase separation and liquid–solid transition in a lennard-jones system. *Soft matter*, 15(36):7275–7285, 2019.

[12] Simon N Weber, Christoph A Weber, and Erwin Frey. Binary mixtures of particles with different diffusivities demix. *Physical review letters*, 116(5):058301, 2016.

[13] Joakim Stenhammar, Raphael Wittkowski, Davide Marenduzzo, and Michael E Cates. Activity-induced phase separation and self-assembly in mixtures of active and passive particles. *Physical review letters*, 114(1):018301, 2015.

[14] Jan Smrek and Kurt Kremer. Small activity differences drive phase separation in active-passive polymer mixtures. *Physical review letters*, 118(9):098002, 2017.

[15] Zachary M Sherman and James W Swan. Dynamic, directed self-assembly of nanoparticles via toggled interactions. *ACS nano*, 10(5):5260–5271, 2016.

[16] Suman Dutta and J Chakrabarti. Anomalous dynamical responses in a driven system. *EPL (Europhysics Letters)*, 116(3):38001, 2016.

[17] Suman Dutta and J Chakrabarti. Transient dynamical responses of a charged binary colloid in an electric field. *Soft matter*, 14(22):4477–4482, 2018.

[18] Prateek K Jha, Vladimir Kuzovkov, Bartosz A Grzybowski, and Monica Olvera De La Cruz. Dynamic self-assembly of photo-switchable nanoparticles. *Soft Matter*, 8(1):227–234, 2012.

[19] Michał Sawczyk and Rafal Klajn. Out-of-equilibrium aggregates and coatings during seeded growth of metallic nanoparticles. *Journal of the American Chemical Society*, 139(49):17973–17978, 2017.

[20] Raphael K Grötsch, Caren Wanzke, Maximilian Speckbacher, Arzu Angı, Bernhard Rieger, and Job Boekhoven. Pathway dependence in the fuel-driven dissipative self-assembly of nanoparticles. *Journal of the American Chemical Society*, 141(25):9872–9878, 2019.

[21] Maku Moronshing and Chandramouli Subramaniam. Room temperature, multiphasic detection of explosives, and volatile organic compounds using thermodiffusion driven soret colloids. *ACS Sustainable Chemistry & Engineering*, 6(7):9470–9479, 2018.

[22] J Calvin Giddings. Field-flow fractionation: analysis of macromolecular, colloidal, and particulate materials. *Science*, 260(5113):1456–1465, 1993.

[23] Stefan Duhr and Dieter Braun. Optothermal molecule trapping by opposing fluid flow with thermophoretic drift. *Physical review letters*, 97(3):038103, 2006.

[24] Arash Nikoubashman. Self-assembly of colloidal micelles in microfluidic channels. *Soft Matter*, 13(1):222–229, 2017.

[25] Stefan Duhr and Dieter Braun. Why molecules move along a temperature gradient. *Proceedings of the National Academy of Sciences*, 103(52):19678–19682, 2006.

[26] A Pérez-Madrid, JM Rubi, and P Mazur. Brownian motion in the presence of a temperature gradient. *Physica A: Statistical Mechanics and its Applications*, 212(3-4):231–238, 1994.

[27] JM Rubı and P Mazur. Simultaneous brownian motion of n particles in a temperature gradient. *Physica A: Statistical Mechanics and its Applications*, 250(1-4):253–264, 1998.

[28] Jérôme Burelbach, David B Brückner, Daan Frenkel, and Erika Eiser. Thermophoretic forces on a mesoscopic scale. *Soft matter*, 14(36):7446–7454, 2018.

[29] Efstathios E Michaelides. Brownian movement and thermophoresis of nanoparticles in liquids. *International Journal of Heat and Mass Transfer*, 81:179–187, 2015.

[30] C Debuschewitz and W Köhler. Molecular origin of thermal diffusion in b e n z e n e+ c y c l o h e x a n e mixtures. *Physical Review Letters*, 87(5):055901, 2001.

[31] Shawn A Putnam and David G Cahill. Transport of nanoscale latex spheres in a temperature gradient. *Langmuir*, 21(12):5317–5323, 2005.

[32] Hong-Ren Jiang, Hirofumi Wada, Natsuhiko Yoshinaga, and Masaki Sano. Manipulation of colloids by a nonequilibrium depletion force in a temperature gradient. *Physical review letters*, 102(20):208301, 2009.

[33] Ning Wei, Hui-Qiong Wang, and Jin-Cheng Zheng. Nanoparticle manipulation by thermal gradient. *Nanoscale research letters*, 7(1):154, 2012.

[34] Tetsuro Tsuji, Yuta Sasai, and Satoyuki Kawano. Thermophoretic manipulation of micro-and nanoparticle flow through a sudden contraction in a microchannel with near-infrared laser irradiation. *Physical Review Applied*, 10(4):044005, 2018.

[35] Alois Würger. Thermal non-equilibrium transport in colloids. *Reports on Progress in Physics*, 73(12):126601, 2010.

[36] Tetsuro Tsuji, Hirotaka Iseki, Itsuo Hanasaki, and Satoyuki Kawano. Negative thermophoresis of nanoparticles interacting with fluids through a purely-repulsive potential. *Journal of Physics: Condensed Matter*, 29(47):475101, 2017.

[37] Frank Smallenburg, Niels Boon, Maarten Kater, Marjolein Dijkstra, and René van Roij. Phase diagrams of colloidal spheres with a constant zeta-potential. *The Journal of chemical physics*, 134(7):074505, 2011.

[38] J Chakrabarti and Suman Dutta. Analytical form of forces in hydrophobic collapse. *Chemical Physics Letters*, 620:109–113, 2015.

[39] Wolfgang Lechner and Christoph Dellago. Accurate determination of crystal structures based on averaged local bond order parameters. *The Journal of chemical physics*, 129(11):114707, 2008.

[40] Zhibing Hu, Peter Schall, et al. Single crystal growth and anisotropic crystal-fluid interfacial free energy in soft colloidal systems. *Physical Review E*, 84(1):011607, 2011.

[41] Wilson CK Poon, Aidan T Brown, Susana OL Direito, Daniel JM Hodgson, Lucas Le Nagard, Alex Lips, Cait E MacPhee, Davide Marenduzzo, John R Royer, Andreia F Silva, et al. Soft matter science and the covid-19 pandemic. *Soft matter*, 16(36):8310–8324, 2020.

[42] Shubham Sharma, Roven Pinto, Abhishek Saha, Swetaprovo Chaudhuri, and Saptarshi Basu. On secondary atomization and blockage of surrogate cough droplets in single-and multilayer face masks. *Science advances*, 7(10):eabf0452, 2021.

[43] World Health Organization. Advice on the use of masks in the context of covid-19: interim guidance, 6 april 2020. Technical documents, 2020.

[44] Mamata Karmacharya, Sumit Kumar, Oleksandra Gulenko, and Yoon-Kyoung Cho. Advances in facemasks during the covid-19 pandemic era. *ACS Applied Bio Materials*, 4(5):3891–3908, 2021.

[45] Sana Ullah, Azeem Ullah, Jaeyun Lee, Yeonsu Jeong, Motahira Hashmi, Chunhong Zhu, Kye Il Joo, Hyung Joon Cha, and Ick Soo Kim. Reusability comparison of melt-blown vs nanofiber face mask filters for use in the coronavirus pandemic. *ACS Applied Nano Materials*, 3(7):7231–7241, 2020.

[46] Fabrice NH Karabulut, Günther Höfler, Naveen Ashok Chand, and Gareth W Beckermann. Electrospun nanofibre filtration media to protect against biological or nonbiological airborne particles. *Polymers*, 13(19):3257, 2021.

[47] Guoxu Liu, Jinhui Nie, Changbao Han, Tao Jiang, Zhiwei Yang, Yaokun Pang, Liang Xu, Tong Guo, Tianzhao Bu, Chi Zhang, et al. Self-powered electrostatic adsorption face mask based on a triboelectric nanogenerator. *ACS applied materials & interfaces*, 10(8):7126–7133, 2018.

[48] Barnali Ghatak, Sanjoy Banerjee, Sk Babar Ali, Rajib Bandyopadhyay, Nityananda Das, Dipankar Mandal, and Bipan Tudu. Design of a self-powered triboelectric face mask. *Nano Energy*, 79:105387, 2021.

[49] Abhiteja Konda, Abhinav Prakash, Gregory A Moss, Michael Schmoldt, Gregory D Grant, and Supratik Guha. Aerosol filtration efficiency of common fabrics used in respiratory cloth masks. *ACS nano*, 14(5):6339–6347, 2020.

[50] Zhimin Hao, Juntao Wu, Chaolu Wang, and Jingang Liu. Electrospun polyimide/metal-organic framework nanofibrous membrane with superior thermal stability for efficient pm2. 5 capture. *ACS applied materials & interfaces*, 11(12):11904–11909, 2019.

[51] Zhongmin Tang, Na Kong, Xingcai Zhang, Yuan Liu, Ping Hu, Shan Mou, Peter Liljeström, Jianlin Shi, Weihong Tan, Jong Seung Kim, et al. A materials-science perspective on tackling covid-19. *Nature Reviews Materials*, 5(11):847–860, 2020.

[52] Bruce J Berne, John D Weeks, and Ruhong Zhou. Dewetting and hydrophobic interaction in physical and biological systems. *Annual review of physical chemistry*, 60:85–103, 2009.

[53] Pieter Rein ten Wolde and David Chandler. Drying-induced hydrophobic polymer collapse. *Proceedings of the National Academy of Sciences*, 99(10):6539–6543, 2002.

[54] Matt Petrowsky and Roger Frech. Temperature dependence of ion transport: the compensated arrhenius equation. *The Journal of Physical Chemistry B*, 113(17):5996–6000, 2009.

[55] Thomas W Lion and Rosalind J Allen. Osmosis in a minimal model system. *The Journal of Chemical Physics*, 137(24):244911, 2012.

[56] Yang Song, Fang Xu, Mingjie Wei, and Yong Wang. Water flow inside polamide reverse osmosis membranes: A non-equilibrium molecular dynamics study. *The Journal of Physical Chemistry B*, 121(7):1715–1722, 2017.

[57] Harry F Ridgway, John Orbell, and Stephen Gray. Molecular simulations of polyamide membrane materials used in desalination and water reuse applications: Recent developments and future prospects. *Journal of Membrane Science*, 524:436–448, 2017.

[58] Geoffrey M Geise, Hae-Seung Lee, Daniel J Miller, Benny D Freeman, James E McGrath, and Donald R Paul. Water purification by membranes: the role of polymer science. *Journal of Polymer Science Part B: Polymer Physics*, 48(15):1685–1718, 2010.

[59] WJ Lau, AF Ismail, N Misdan, and MA Kassim. A recent progress in thin film composite membrane: A review. *Desalination*, 287:190–199, 2012.

[60] Romil Mehta, H Brahmbhatt, Gopal Bhojani, M Mukherjee, and A Bhattacharya. Poly (piperizinamide) with copper ion composite membranes: Application for mitigation of hexaconazole from water and combat microbial contamination. *Journal of hazardous materials*, 376:102–111, 2019.

[61] Wataru Kushida, Ralph Rolly Gonzales, Takuji Shintani, Atsushi Matsuoka, Keizo Nakagawa, Tomohisa Yoshioka, and Hideto Matsuyama. Organic solvent mixture separation using fluorine-incorporated thin film composite reverse osmosis membrane. *Journal of Materials Chemistry A*, 10(8):4146–4156, 2022.

[62] Erminia Leonardi, Bruno D'Aguanno, and Celestino Angeli. Temperature and composition dependence of the soret coefficient in lennard-jones mixtures presenting evaporation/condensation phase transition. *The Journal of chemical physics*, 134(11):114512, 2011.

[63] Mauro Ferrario, S Bonella, and G Ciccotti. On the establishment of thermal diffusion in binary lennard-jones liquids. *The European Physical Journal Special Topics*, 225(8):1629–1642, 2016.

[64] Bjørn Hafskjold. Non-equilibrium molecular dynamics simulations of the transient ludwig-soret effect in a binary lennard-jones/spline mixture. *The European Physical Journal E*, 40(1):1–9, 2017.

[65] Martin P Lautenschlaeger, Martin Horsch, and Hans Hasse. Simultaneous determination of thermal conductivity and shear viscosity using two-gradient non-equilibrium molecular dynamics simulations. *Molecular Physics*, 117(2):189–199, 2019.

[66] Hiroki Matsubara, Gota Kikugawa, and Taku Ohara. All-and one-particle distribution functions at nonequilibrium steady state under thermal gradient. *Physical Review E*, 99(5):052110, 2019.

[67] Philipp Schapotschnikow, Rene Pool, and Thijs JH Vlugt. Molecular simulations of interacting nanocrystals. *Nano letters*, 8(9):2930–2934, 2008.

[68] Yiyong Mai and Adi Eisenberg. Self-assembly of block copolymers. *Chemical Society Reviews*, 41(18):5969–5985, 2012.

[69] Paul L Stiles, Jon A Dieringer, Nilam C Shah, and Richard P Van Duyne. Surface-enhanced raman spectroscopy. *Annu. Rev. Anal. Chem.*, 1:601–626, 2008.

[70] Sutapa Dutta, Piya Patra, and Jaydeb Chakrabarti. Self-assembly in amphiphilic macromolecules with solvent exposed hydrophobic moieties. *Biopolymers*, 110(12):e23330, 2019.

[71] M. Rex and H. Löwen. Lane formation in oppositely charged colloids driven by an electric field: Chaining and two-dimensional crystallization. *Phys. Rev. E*, 75:051402, May 2007.

[72] Pieter-Reináten Wolde et al. Simulation of homogeneous crystal nucleation close to coexistence. *Faraday discussions*, 104:93–110, 1996.

[73] Hossein Eslami, Neda Khanjari, and Florian Muller-Plathe. A local order parameter-based method for simulation of free energy barriers in crystal nucleation. *Journal of Chemical Theory and Computation*, 13(3):1307–1316, 2017. PMID: 28195473.

[74] J Pellicer, V García-Morales, Luis Guanter, MJ Hernández, and M Dolz. On the experimental values of the water surface tension used in some textbooks. *American Journal of Physics*, 70(7):705–709, 2002.

[75] George S Kell. Density, thermal expansivity, and compressibility of liquid water from 0. deg. to 150. deg.. correlations and tables for atmospheric pressure and saturation reviewed and expressed on 1968 temperature scale. *Journal of Chemical and Engineering Data*, 20(1):97–105, 1975.

[76] Jordan Beurton, Philippe Lavalle, Arnaud Pallotta, Thomas Chaigneau, Igor Clarot, and Ariane Boudier. Design of surface ligands for blood compatible gold nanoparticles: effect of charge and binding energy. *International Journal of Pharmaceutics*, page 119244, 2020.

[77] Donald L Ermak. A computer simulation of charged particles in solution. i. technique and equilibrium properties. *The Journal of Chemical Physics*, 62(10):4189–4196, 1975.

[78] Pradipta Kr Das. Effect of temperature on zeta potential of functionalized gold nanorod. *Microfluidics and Nanofluidics*, 21(5):95, 2017.

[79] Michael P Allen and Dominic J Tildesley. *Computer simulation of liquids*. Oxford university press, 2017.

[80] Emanuele Boattini, Marjolein Dijkstra, and Laura Filion. Unsupervised learning for local structure detection in colloidal systems. *The Journal of chemical physics*, 151(15):154901, 2019.

[81] Gideon Schwarz. Estimating the dimension of a model. *The annals of statistics*, pages 461–464, 1978.

[82] Jean-Patrick Baudry, Adrian E Raftery, Gilles Celeux, Kenneth Lo, and Raphael Gottardo. Combining mixture components for clustering. *Journal of computational and graphical statistics*, 19(2):332–353, 2010.

[83] Fabian Pedregosa, Gaël Varoquaux, Alexandre Gramfort, Vincent Michel, Bertrand Thirion, Olivier Grisel, Mathieu Blondel, Peter Prettenhofer, Ron Weiss, Vincent Dubourg, et al. Scikit-learn: Machine learning in python. *the Journal of machine Learning research*, 12:2825–2830, 2011.

[84] Melvin Avrami. Kinetics of phase change. ii transformation-time relations for random distribution of nuclei. *The Journal of chemical physics*, 8(2):212–224, 1940.

[85] Melvin Avrami. Kinetics of phase change. i general theory. *The Journal of chemical physics*, 7(12):1103–1112, 1939.

[86] D Crespo and T Pradell. Evaluation of time-dependent grain-size populations for nucleation and growth kinetics. *Physical Review B*, 54(5):3101, 1996.

[87] Xin Qi, Yong Chen, Yan Jin, and Yao-Hui Yang. Bond-orientational order in melting of colloidal crystals. *arXiv preprint cond-mat/0603229*, 2006.

[88] Nadezhda Gribova, Axel Arnold, Tanja Schilling, and Christian Holm. How close to two dimensions does a lennard-jones system need to be to produce a hexatic phase? *The Journal of chemical physics*, 135(5):054514, 2011.

[89] Hartmut Löwen. Melting, freezing and colloidal suspensions. *Physics Reports*, 237(5):249–324, 1994.

[90] Stan Salvador and Philip Chan. Determining the number of clusters/segments in hierarchical clustering/segmentation algorithms. In *16th IEEE international conference on tools with artificial intelligence*, pages 576–584. IEEE, 2004.

[91] Sajjad Ashraf, Hun-Kuk Park, Hansoo Park, and Soo-Hong Lee. Snapshot of phase transition in thermoresponsive hydrogel pnipam: Role in drug delivery and tissue engineering. *Macromolecular Research*, 24(4):297–304, 2016.

[92] Kunpeng Cui and Jian Ping Gong. Aggregated structures and their functionalities in hydrogels. *Aggregate*, 2(2):e33, 2021.

[93] D Karthickeyan, RG Joshi, and BVR Tata. Fcc-hcp coexistence in dense thermo-responsive microgel crystals. *The Journal of Chemical Physics*, 146(22):224503, 2017.

[94] Jannis Kolker, Johannes Harrer, Simone Ciarella, Marcel Rey, Maret Ickler, Liesbeth MC Janssen, Nicolas Vogel, and Hartmut Löwen. Interface-induced hysteretic volume phase transition of microgels: simulation and experiment. *Soft Matter*, 17(22):5581–5589, 2021.

[95] Yan Zhang, Wuli Yang, Changchun Wang, Wei Wu, and Shoukuan Fu. Thermosensitive nanocontainers prepared from poly (n-isopropylacrylamide-co-n-(hydroxylmethyl) acrylamide)-g-poly (lactide). *Journal of nanoscience and nanotechnology*, 6(9-10):2896–2901, 2006.

[96] Jung-Fu Lin, Olga Degtyareva, Charles T Prewitt, Przemyslaw Dera, Nagayoshi Sata, Eugene Gregoryanz, Ho-Kwang Mao, and Russell J Hemley. Crystal structure of a high-pressure/high-temperature phase of alumina by in situ x-ray diffraction. *Nature materials*, 3(6):389–393, 2004.

[97] Artem R Oganov, Michael J Gillan, and G David Price. Structural stability of silica at high pressures and temperatures. *Physical Review B*, 71(6):064104, 2005.

[98] Masanori Matsui and Orson L Anderson. The case for a body-centered cubic phase (α') for iron at inner core conditions. *Physics of the Earth and Planetary Interiors*, 103(1-2):55–62, 1997.

[99] Herman JC Berendsen, JPM van Postma, Wilfred F Van Gunsteren, ARHJ DiNola, and Jan R Haak. Molecular dynamics with coupling to an external bath. *The Journal of chemical physics*, 81(8):3684–3690, 1984.

[100] Bruno J Strasser and Thomas Schlich. A history of the medical mask and the rise of throwaway culture. *The Lancet*, 396(10243):19–20, 2020.

[101] Wei Lyu and George L Wehby. Community use of face masks and covid-19: Evidence from a natural experiment of state mandates in the us: Study examines impact on covid-19 growth rates associated with state government mandates requiring face mask use in public. *Health affairs*, 39(8):1419–1425, 2020.

[102] Mervin Zhao, Lei Liao, Wang Xiao, Xuanze Yu, Haotian Wang, Qiqi Wang, Ying Ling Lin, F Selcen Kilinc-Balci, Amy Price, Larry Chu, et al. Household materials selection for homemade cloth face coverings and their filtration efficiency enhancement with triboelectric charging. *Nano letters*, 20(7):5544–5552, 2020.

[103] Martin Z Bazant and John WM Bush. A guideline to limit indoor airborne transmission of covid-19. *Proceedings of the National Academy of Sciences*, 118(17), 2021.

[104] Shuo Feng, Chen Shen, Nan Xia, Wei Song, Mengzhen Fan, and Benjamin J Cowling. Rational use of face masks in the covid-19 pandemic. *The Lancet Respiratory Medicine*, 8(5):434–436, 2020.

[105] EC Riley, G Murphy, and RL Riley. Airborne spread of measles in a suburban elementary school. *American journal of epidemiology*, 107(5):421–432, 1978.

[106] William F Wells. On air-borne infection: study ii. droplets and droplet nuclei. *American journal of Epidemiology*, 20(3):611–618, 1934.

[107] Roland R Netz and William A Eaton. Physics of virus transmission by speaking droplets. *Proceedings of the National Academy of Sciences*, 117(41):25209–25211, 2020.

[108] Anže Božič and Matej Kanduč. Relative humidity in droplet and airborne transmission of disease. *Journal of Biological Physics*, 47(1):1–29, 2021.

[109] Wenjia Du, Francesco Iacoviello, Tacson Fernandez, Rui Loureiro, Daniel JL Brett, and Paul R Shearing. Microstructure analysis and image-based modelling of face masks for covid-19 virus protection. *Communications Materials*, 2(1):1–10, 2021.

[110] Wafa K Essa, Suhad A Yasin, Ibtisam A Saeed, and Gomaa AM Ali. Nanofiber-based face masks and respirators as covid-19 protection: A review. *Membranes*, 11(4):250, 2021.

[111] Wonjun Yim, Diyi Cheng, Shiv H Patel, Rui Kou, Ying Shirley Meng, and Jesse V Jokerst. Kn95 and n95 respirators retain filtration efficiency despite a loss of dipole charge during decontamination. *ACS applied materials & interfaces*, 12(49):54473–54480, 2020.

[112] Sejin Choi, Hyeonyeol Jeon, Min Jang, Hyeri Kim, Giyoung Shin, Jun Mo Koo, Minkyung Lee, Hye Kyeong Sung, Youngho Eom, Ho-Sung Yang, et al. Biodegradable, efficient, and breathable multi-use face mask filter. *Advanced Science*, 8(6):2003155, 2021.

[113] Siddhartha Verma, Manhar Dhanak, and John Frankenfield. Visualizing the effectiveness of face masks in obstructing respiratory jets. *Physics of Fluids*, 32(6):061708, 2020.

[114] Li Yi, Li Fengzhi, and Zhu Qingyong. Numerical simulation of virus diffusion in facemask during breathing cycles. *International journal of heat and mass transfer*, 48(19-20):4229–4242, 2005.

[115] Praveen Kumar, Ligesh Theeyancheri, Subhasish Chaki, and Rajarshi Chakrabarti. Transport of probe particles in a polymer network: effects of probe size, network rigidity and probe–polymer interaction. *Soft Matter*, 15(44):8992–9002, 2019.

[116] RK Singh, Jaladhar Mahato, Arindam Chowdhury, Anirban Sain, and Amitabha Nandi. Non-gaussian subdiffusion of single-molecule tracers in a hydrated polymer network. *The Journal of Chemical Physics*, 152(2):024903, 2020.

[117] Hyun Woo Cho, Haein Kim, Bong June Sung, and Jun Soo Kim. Tracer diffusion in tightly-meshed homogeneous polymer networks: A brownian dynamics simulation study. *Polymers*, 12(9):2067, 2020.

[118] Valerio Sorichetti, Virginie Hugouvieux, and Walter Kob. Dynamics of nanoparticles in polydisperse polymer networks: From free diffusion to hopping. *Macromolecules*, 54(18):8575–8589, 2021.

[119] SJ Anderson, Jonathan Garamella, S Adalbert, RJ McGorty, and RM Robertson-Anderson. Subtle changes in crosslinking drive diverse anomalous transport characteristics in actin–microtubule networks. *Soft Matter*, 17(16):4375–4385, 2021.

[120] Nairhita Samanta and Rajarshi Chakrabarti. Tracer diffusion in a sea of polymers with binding zones: mobile vs. frozen traps. *Soft matter*, 12(41):8554–8563, 2016.

[121] Steven R Lustig, John JH Biswakarma, Devyesh Rana, Susan H Tilford, Weike Hu, Ming Su, and Michael S Rosenblatt. Effectiveness of common fabrics to block aqueous aerosols of virus-like nanoparticles. *ACS nano*, 14(6):7651–7658, 2020.

[122] Parnia Forouzandeh, Kris O'Dowd, and Suresh C Pillai. Face masks and respirators in the fight against the covid-19 pandemic: An overview of the standards and testing methods. *Safety science*, 133:104995, 2021.

[123] T Schneider and E Stoll. Molecular-dynamics study of a three-dimensional one-component model for distortive phase transitions. *Physical Review B*, 17(3):1302, 1978.

[124] C. G. Opaskar and Samuel Krimm. Tetrahedral approximation in normal coordinate calculations of high polymers. *Spectrochimica Acta Part A: Molecular and Biomolecular Spectroscopy*, 21:1165–1166, 1965.

[125] A. P. Thompson, H. M. Aktulga, R. Berger, D. S. Bolintineanu, W. M. Brown, P. S. Crozier, P. J. in 't Veld, A. Kohlmeyer, S. G. Moore, T. D. Nguyen, R. Shan, M. J. Stevens, J. Tranchida, C. Trott, and S. J. Plimpton. LAMMPS - a flexible simulation tool for particle-based materials modeling at the atomic, meso, and continuum scales. *Comp. Phys. Comm.*, 271:108171, 2022.

[126] Kiyotaka Sakai. Dialysis membranes for blood purification. *Frontiers of medical and biological engineering: the international journal of the Japan Society of Medical Electronics and Biological Engineering*, 10(2):117–129, 2000.

[127] Nasibeh Hajilary, Mashallah Rezakazemi, and Saeed Shirazian. Biofuel types and membrane separation. *Environmental Chemistry Letters*, 17:1–18, 2019.

[128] C Benito-Alcázar, MC Vincent-Vela, JM Gozálvez-Zafrilla, and J Lora-García. Study of different pretreatments for reverse osmosis reclamation of a petrochemical secondary effluent. *Journal of hazardous materials*, 178(1-3):883–889, 2010.

[129] J Radjenović, M Petrović, F Ventura, and D Barceló. Rejection of pharmaceuticals in nanofiltration and reverse osmosis membrane drinking water treatment. *Water research*, 42(14):3601–3610, 2008.

[130] W.J. Lau, A.F. Ismail, N. Misdan, and M.A. Kassim. A recent progress in thin film composite membrane: A review. *Desalination*, 287:190–199, 2012. Special Issue in honour of Professor Takeshi Matsuura on his 75th Birthday.

[131] Ruth Habte Hailemariam, Yun Chul Woo, Mekdimu Mezemir Damtie, Bong Chul Kim, Kwang-Duck Park, and June-Seok Choi. Reverse osmosis membrane fabrication and modification technologies and future trends: A review. *Advances in colloid and interface science*, 276:102100, 2020.

[132] J Muscatello, EA Müller, AA Mostofi, and AP Sutton. Multiscale molecular simulations of the formation and structure of polyamide membranes created by interfacial polymerization. *Journal of Membrane Science*, 527:180–190, 2017.

[133] Santanu Karan, Zhiwei Jiang, and Andrew G Livingston. Sub–10 nm polyamide nanofilms with ultrafast solvent transport for molecular separation. *Science*, 348(6241):1347–1351, 2015.

[134] Haifeng Wang, Lei Li, Xiaosa Zhang, and Suobo Zhang. Polyamide thin-film composite membranes prepared from a novel triamine 3, 5-diamino-n-(4-aminophenyl)-benzamide monomer and m-phenylenediamine. *Journal of Membrane Science*, 353(1-2):78–84, 2010.

[135] Byeong-Heon Jeong, Eric MV Hoek, Yushan Yan, Arun Subramani, Xiaofei Huang, Gil Hurwitz, Asim K Ghosh, and Anna Jawor. Interfacial polymerization of thin film nanocomposites: a new concept for reverse osmosis membranes. *Journal of membrane science*, 294(1-2):1–7, 2007.

[136] Romil Mehta, Harshad Brahmbhatt, Gopal Bhojani, and Amit Bhattacharya. Polypyrrole as the interlayer for thin-film poly (piperazine-amide) composite membranes: separation behavior of salts and pesticides. *Journal of Applied Polymer Science*, 138(18):50356, 2021.

[137] John Chau, Prithish Basak, and Kamalesh K Sirkar. Reverse osmosis separation of particular organic solvent mixtures by a perfluorodioxole copolymer membrane. *Journal of Membrane Science*, 563:541–551, 2018.

[138] Tiefan Huang, Basem A Moosa, Phuong Hoang, Jiangtao Liu, Stefan Chisca, Gengwu Zhang, Mram AlYami, Niveen M Khashab, and Suzana P Nunes. Molecularly-porous ultrathin membranes for highly selective organic solvent nanofiltration. *Nature Communications*, 11(1):5882, 2020.

[139] Minxia Ding, Anthony Szymczyk, and Aziz Ghoufi. On the structure and rejection of ions by a polyamide membrane in pressure-driven molecular dynamics simulations. *Desalination*, 368:76–80, 2015.

[140] Weimin Gao, Fenghua She, Juan Zhang, Ludovic F Dumée, Li He, Peter D Hodgson, and Lingxue Kong. Understanding water and ion transport behaviour and permeability through poly (amide) thin film composite membrane. *Journal of Membrane Science*, 487:32–39, 2015.

[141] Adam Inurria, Pinar Cay-Durgun, Douglas Rice, Haojie Zhang, Dong-Kyun Seo, Mary Laura Lind, and François Perreault. Polyamide thin-film nanocomposite membranes with graphene oxide nanosheets: Balancing membrane performance and fouling propensity. *Desalination*, 451:139–147, 2019.